UNIVERSITEIT VAN PRETORIA
UNIVERSITY OF PRETORIA
YUNIBESITHI YA PRETORIA

COMPUTATIONAL FLUID DYNAMICS MODEL FOR CONTROLLING DUST AND METHANE IN UNDERGROUND COALMINES

Submitted in partial fulfilment of the requirements for the degree of

Master in Applied Science

M.Sc Appl. Sci. (Mechanics)

in the

Faculty of Engineering, Built Environment and Information Technology

University of Pretoria

Compiled by: **Dickson Daniel Ndenguma**

27229573

Study Leaders: **Dr. J. Dirker and Prof. NDL Burger**

Year: **September 2010**

ABSTRACT

Computational Fluid Dynamics Model for Controlling Dust and Methane in Underground Coalmine

Author	:	Dickson Daniel Ndenguma
Student Number	:	27229573
Study Leader	:	Dr. J. Dirker and Prof. NDL Burger
Degree	:	Masters of Applied Science (Mechanical)
Department	:	Mechanical and Aeronautical Engineering

ABSTRACT

Airborne dust and methane are common problems in the underground coalmines. They pose health and safety risk to mining personnel, and a safety risk to mining equipment as well. In order to prevent these risks air borne dust and methane concentrations must be reduced to within the acceptable levels. In South Africa, the dust and methane concentration in coalmines should not exceed 2.0 mg/m³ and 0.5% per volume, respectively.

Mine ventilation is one of the popular ways of controlling both dust and methane. Different ventilation systems have been designed since the history of underground coal mining. Unfortunately, none provides ultimate solution to the dust and methane problem, especially in the most critical areas of the underground coalmine, like blind-end of the heading and last through road.

By changing airflow patterns and air velocity, it is possible to obtain an optimum ventilation design that can keep dust and methane within the acceptable levels.

ABSTRACT

Since it is very difficult to conduct experiments in the underground coalmine due to harsh environmental conditions and tight production schedules, the designer made use of the Computational Fluid Dynamics (CFD) modelling technique. The models were then experimentally verified and validated using a scaled down model at University of Pretoria.

After verification further numerical analysis was done to in order to device a method for determining optimum fan positions for different heading dimensions.

This study proves that CFD can be used to model ventilation system of a scaled down coalmine model. Therefore chances that this might be true for the actual mine are very high but it needs to be investigated. If this is found to be true then CFD modelling will be a very useful tool in coalmine ventilation system research and development.

LIST OF ABBREVIATIONS, SYMBOLS AND TERMS

ABBREVIATIONS

AC	Alternating Current
ARD	Airborne Respirable Dust
CAD	Computer Aided Drawing
CFD	Computational Fluid Dynamics
CM	Coal Miner
CPU	Computer Processing Unit
CSIR	Council for Scientific and Industrial Research
CWP	Coal Workers' Pneumoconiosis
DAU	Data Acquisition Unit
DC	Direct Current
DME	Department of Minerals and Energy
FVM	Finite Volume Method
GM	Mine Geometry
KSSC	Kloppersbos Shear Spray Curtain
LED	Light Emitting Diode
LTR	Last Through Road
PDE	Partial Differential Equation
RSA	Republic of South Africa
USA	United States of America

SYMBOLS

English Symbols		Units
A_s	Shift production	tonne[1]
A_d	Airborne dust created per tonne of raw coal production	mg/ton
A_{ms}	Scaled model scrubber exit area	m^2
c	Wave speed	m/s
D	Diameter	m
D_{fcm}	Full scale CM cutting drum diameter	m
D_{mcm}	Scale model continuous miner cutting drum diameter	m
D_{fj}	Full scale jet fan diameter	m
D_{mj}	Scale model jet fan diameter	m
D_{fs}	Full scale scrubber diameter	m
D_{fs}	Scale model scrubber diameter	m
E_i	Internal energy	J
e	Wall roughness height	mm
F_n	Surface stress normal to the boundary	N/m^2
F_t	Surface stress tangential to the boundary	N/m^2
f	Friction factor	
g	Acceleration due to gravity	m/s^2
H_{fcm}	Full scale CM height	m
H_{fh}	Full scale heading height	m
H_{ft}	Full scale through-road height	m
H_{mcm}	Scaled model CM height	m
H_{mh}	Scaled model heading height	m
H_{mt}	Scaled model through-road height	m
h	Enthalpy	kJ/kg

[1] 1 tonne = 1000 kg

SYMBOLS

h_L	Head loss	m
K	Head loss coefficient	
k	Conduction of continuum	W/mK
L_{fcm}	Full scale CM length	m
L_{ft}	Full scale through-road length	m
L_{fh}	Full scale heading length	m
L_f	Fan position with respect to heading entrance	m
L_{mcm}	Scaled model CM length	m
L_{mh}	Scaled model heading length	m
L_{mt}	Scaled model through-road length	m
M	Mach number	
P	Pressure	Pa
Q_{air}	Volume of air	m^3
Q_{fs}	Full scale scrubber exit volumetric flow rate	m^3/s
Q_{fj}	Full scale scrubber exit volumetric flow rate	m^3/s
Q_{ft}	Full scale jet fan volumetric flow rate	m^3/s
Q_{ms}	Scaled model scrubber exit volumetric flow rate	m^3/s
Q_{mt}	Scaled model through-road volumetric flow rate	m^3/s
Q_{mj}	Scaled model jet fan volumetric flow rate	m^3/s
q_d	Average dust concentration per shift	mg/m^3
q	Heat flow	kJ/m
R	Hydraulic radius	m
Re	Reynolds number	
R_{fj}	Full scale jet fan penetration	m
R_{mj}	Scaled model jet fan penetration	m
S_{Mx} , $S_{My,}$ S_{Mz}	Body forces in directions x, y, z	N
t_d	Dust sampling time	min
T	Absolute temperature	K
t	Time	sec
$\boldsymbol{T_w}$	Wall temperature	K

SYMBOLS

u, v, w	Cartesian velocity components	m/s
$\boldsymbol{V}$	Velocity vector (column)	m/s
$\boldsymbol{V}_w$	Wall velocity vector	m
V_{fj}	Full scale jet fan velocity	m/s
V_{fs}	Full scale scrubber exit velocity	m/s
V_{ft}	Full scale through-road velocity	m/s
V_{ms}	Scaled model scrubber exit velocity	m/s
V_{mt}	Scaled model through-road velocity	m/s
V_{mj}	Scaled model jet fan velocity	m/s
W_{fcm}	Full scale CM width	m
W_{fh}	Full scale heading width	m
W_{ft}	Full scale through-road width	m
W_{mcm}	Scaled model CM width	m
W_{mh}	Scaled model heading width	m
W_{mt}	Scaled model through-road width	m
x, y, z	Cartesian space coordinates	m

Greek Symbols

ρ	Density	kg/m^3
μ	Viscosity due to linear deformation	Ns/m^2
λ	Viscosity due to volumetric deformation	Ns/m^2
Φ	Dissipation function or deformation heating	W/m
υ	Kinematic viscosity	m^2/s
γ	Specific weight	N/m^3
τ	Wall shear	N/m^2

ACKNOWLEDGEMENTS

Acknowledgements

I would like to thank God and the following people and organisations for their support and contributions to this dissertation:

Dr. Jaco Dirker and Prof. NDL Burger, for leadership and guidance
AEROTHEM, for proving introductory training in Star CCM+

The following persons are also thanked for providing moral support and encouragement:
Florence, my wife
Jones Kharika
Mathias Kyembe

TABLE OF CONTENTS

TABLE OF CONTENTS

TABLE OF CONTENTS

TABLE OF CONTENTS

TABLE OF CONTENTS

TABLE OF CONTENTS

LIST OF FIGURES

LIST OF FIGURES

CHAPTER 1: INTRODUCTION AND LITERATURE SURVEY

CHAPTER 2: PROBLEM STATEMENT AND METHODOLOGY

CHAPTER 3: CFD MODEL AND CFD RESULTS

LIST OF FIGURES

LIST OF FIGURES

LIST OF FIGURES

CHAPTER 6: FAN POSITION OPTIMIZATION

LIST OF TABLES

LIST OF TABLES

CHAPTER 1: INTRODUCTION AND LITERATURE STUDY

CHAPTER 2: PROBLEM STATEMENT AND METHODOLOGY

CHAPTER 3: CFD MODEL AND CFD RESULTS

CHAPTER 4: EXPERIMENTAL MODEL AND RESULTS

LIST OF TABLES

CHAPTER 6: FAN POSITION OPTIMIZATION

1. INTRODUCTON AND LITERATURE SURVEY

1.1 INTRODUCTION

Coal, a solid flammable rock, is a hydrocarbon compound formed from prehistoric vegetation which has been long buried in the ground, and has been altered by the combined effects of the pressure and heat. Internationally, coal is the most widely used primary fuel, accounting for about 36% of the total fuel consumption of the world's electricity production. About 77% of South Africa's primary energy needs are provided by coal. This situation is unlikely to change significantly in the near future due to a lack of economical and widely available alternative energy source [1].

Depending on its geological formation, coal can either be extracted from opencast or underground mining. The ratio between opencast and underground mining in South African coal industry in 2002 was 48 % and 52% respectively [1].

Like any other mining operations, the extraction of coal, especially underground coal mining, is associated with a number of hazards. The common problems encountered in underground coal mining are Airborne Respirable Dust (ARD) and mine gas[2].

As coal rocks are brittle, their mining in any form gives rise to a wide range of breakage products, of which a more or less constant proportion is fine material. Where the breakage of sandstone or shale, rather than coal takes place, a higher proportion of fine dust is produced. ARD concentration in the mine is high enough that if not well controlled it puts the health and safety of the workers and performance of mining equipment at risk. The dust hazard can be considered from three aspects: explosions and fire hazards, health risk and nuisance value.

[2] Mine gas is also referred to as methane. This is because 80% to 96% by volume of mine gas is methane.

In the underground coalmine, methane explosions can occur in any place as long as the conditions are favourable. However, most of them occur at the working faces where methane emission is the largest. These areas are the gob[3], working faces at the development entries, gob-side tail entry T-junction, near the cutting drum of the Continuous Miner (CM] or shearer, and in the roof fall cavities.

To prevent mine workers from dust and methane hazards, it must be ensured that the dust and methane concentration levels do not exceed the recommended standards. In South Africa, the dust concentration level in the underground coalmine should not exceed 2.0 mg/m³ at operator's position and methane level should not exceed the maximum concentration of 0.5% per volume [10].

Years of continuous research, development, investigation and experience have produced a number of techniques and a variety of equipment which can be applied to limit and control the production and concentration of dust and methane. Unfortunately, most underground dust control methods yield only 25 % to 50 % reductions in respirable dust [2]. Often, these reductions are not enough to achieve compliance with dust standards. At the same time more productive mining techniques that results in more dust have and are being innovated. As a result of this, there is a need for continuous improvement of the performance of dust and methane controlling machines and techniques to enable all miners to work in a health and safe environment.

Ventilation is a popular technique that is used to control dust and mine gas in underground coalmine. In this method air is utilized to dilute dust and mine gas to allowable concentration or blow the dust away from mine worker. But, since the heading is a blind-end penetration, air being blown into the heading is restricted and the air also re-circulates within the heading making the exercise very difficult.

[3] Gob is waste material produced in coal mining, consisting of clay, shale, etc

One of the problems currently being faced by coal mining operations is the control of dust and methane in the heading and Last Through Road [LTR]. It is therefore important to find an efficient ventilation technique that can be applied to control dust and methane in these areas in the coalmine, to the recommended standards. It is conceivable that by changing airflow pattern in the mine dust and methane dilution capacity will also change.

Unfortunately, carrying out a research activity like this in the actual mine is almost impossible. This is because production schedules are very tight, environmental conditions hush and experimental costs high. Therefore this study seeks to investigate comparatively inexpensive Computational Fluid Dynamics[4] (CFD) modelling technique which can reliably be utilized in solving ARD and mine gas concentration problems in underground coalmine.

In section 1.2, some background information is presented to acquaint the reader with underground coal mining activities and problems that arise from ARD and mine gas. Brief information on CFD and optimization is presented as well. Problem statement and method that was utilized in this study is presented chapter 2. Construction of CFD models is covered in chapter 3. Then practical experiments which were done using a scaled down coalmine model with the purpose of verifying the CFD model is presented in Chapter 4. Chapter 5 analyses and compares CFD and experimental results. Further numerical analysis with an objective devising a method for determining optimum position of jet fan is covered in chapter 6. The dissertation finishes with conclusions and description of future work and related topics that arose from this study.

[4] CFD is the analysis of systems involving fluid flow, heat transfer and associated phenomena such as chemical reactions by means of computer-based simulation [20].

1.2. LITERATURE STUDY

1.2.1. Mining Activities in Underground Coal Mines

1.2.1.1. Mining Techniques

In the early days coal was obtained by digging it from where it appeared on the surface. Later the first small mines were sunk known as bell pits. As mining techniques constantly improved, working into deeper seams became feasible. The two major types of mines are underground mines and surface or opencast mines. This dissertation is dealing with underground coalmines.

In underground coalmine different extraction methods are used depending upon the geological formations of the coal and other factors. The two major extraction methods are Bord and pillar (also referred to Room and Pillar) and Long wall. The two methods are sometimes combined to come up the third method known as Short wall.

1.2.1.1.1. Bord and Pillar Mining Technique

Bord and pillar mining is the most common type of underground coal mining method in the world, see Figure 1.1. [3]. Cutting operations are performed using a Continuous Miner (CM) that cuts out extended cuts into the mining face. To complete a cutting operation the CM makes four cuts, each 17.5 m long and 3.5 m wide into the coal seam. These cuts are known as box cuts. The final depth of the heading might be up to 35 m, the width up to 7 m and the height depends on the thickness of the coal seam.

As the rooms are cut, the CM simultaneously loads the coal onto a shuttle or ram car where it will eventually be loaded on a conveyor belt that will move it to the surface. Each room alternates with a pillar of greater width for support. Using this method

normally results in a reduction in recovery of as much as 60 percent because of coal being left in the ground as pillars. As mining continues, roof bolts are placed in the ceiling to avoid ceiling collapse. Under special circumstances, pillars may sometimes be removed or pulled towards the end of mining in a process called retreat mining.

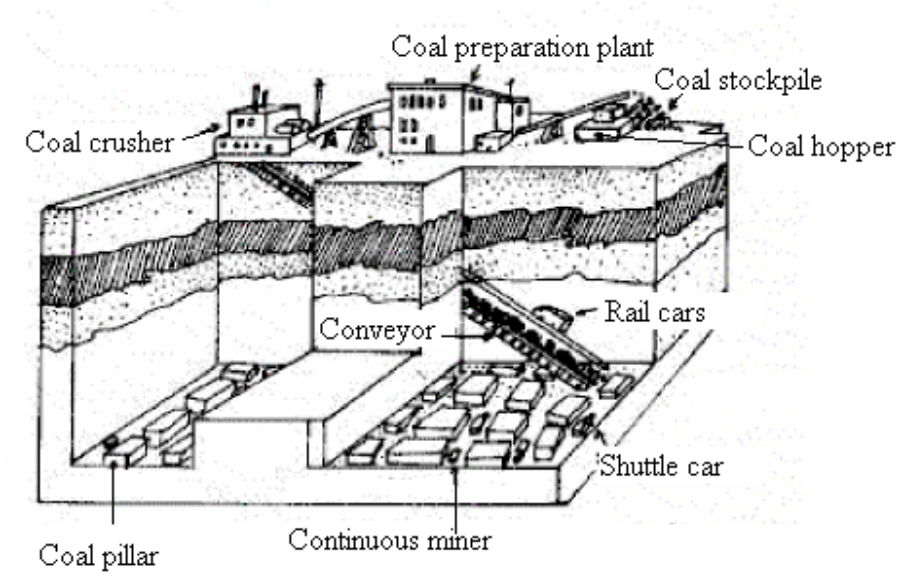

Figure 1.1: Perspective view of bord and pillar mining method [3]

Bord and pillar mining has been, and still is, most widely practiced method of underground coal mining in South Africa owing to its inherent safety, low capital investment, and low operating cost [4]. The Twisdraai coalmine, part of Sasol Mining's Secunda Collieries[5] complex is one example of a board and pillar operation. At these mines rooms, also referred to as headings during cutting process, are accomplished by four cuts, as already explained above.

[5] Coalmine with its buildings and equipment

In opening a mine on the bord and pillar system, gangways, entries, headings or galleries, as they are variously called, are first run forward on the face and end slips of the coal seam. The entries constitute the main avenues of the mine; they are usually driven much narrower than the rooms so as to make them safer, as well as to add strength to the pillars. In the headings breakthroughs, also referred to as Last Through Road (LTR), need to be made from one heading to another at stated intervals for the passage of the ventilating current of air and other purposes.

1.2.1.1.2. Long wall Mining Technique

With long wall mining methods the principle is to extract all of the coal over the width of the panel face in successive cuts, see figure 1.2. After the coal is removed, it drops onto a chain conveyor, which moves it to a second conveyor that will eventually take the coal to the surface. Temporary hydraulic-powered roof supports hold up the roof as the extraction process proceeds. This method of mining has proved to be more efficient than conventional room and pillar mining, with a recovery rate of nearly 75 %, but the equipment is more expensive than conventional bord and pillar equipment, and cannot be applied in all geological circumstances. As mining continue, only the roofs for main tunnels are bolted to avoid ceiling collapse. The rest of the roof is supported by large steel supports, attached to the mining machine. As the machine moves forward, the roof supports also advance. The roof behind the support is allowed to fall.

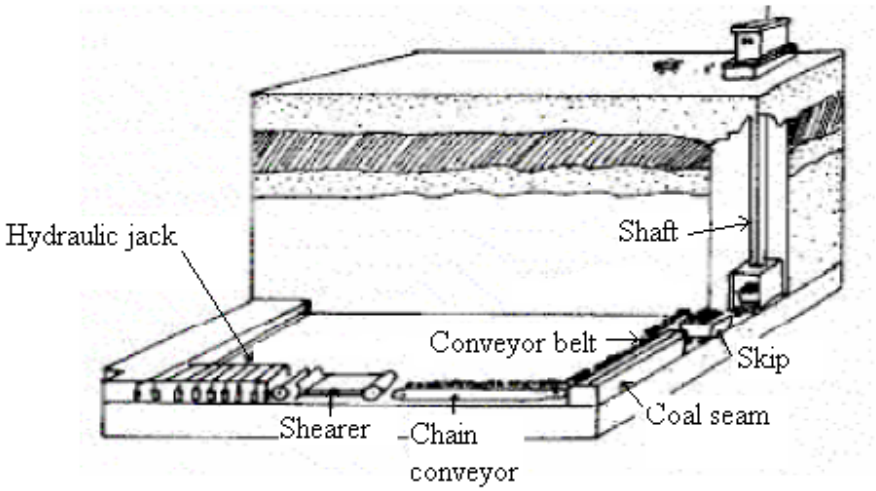

Figure 1.2: Perspective view of long wall mining method [3].

1.2.1.1.3. Short wall Mining Technique

The short wall method combines many of the features of bord and pillar and long wall. The area to be mined is developed by bord and pillar equipment, but the blocked-out pillars are larger. The pillars are extracted by taking wide slices off a relatively short wall, the roof being controlled by heavy-duty powered supports of the type commonly used on long walls.

The primary difference between long wall and short wall methods is that short walls are generally 46 to 61 metres wide, while the long walls are 106 to 182 metres wide [3]. Long wall mining can be practiced as an advancing or a retreating system (although only the latter currently is being used in South Africa) while short wall mining is usually only practiced on the retreat. In 2002, South Africa had three mines, namely, Malta No. 2, Amot No. 8 shaft and New Denmark, Okhozini Shaft, extracting coal by short wall method [1].

A major advantage of this method is that the same equipment, with the exception of the powered supports, can be used in both the development and pillar extraction phases of operation. And the capital cost of the supports is lower than for a long wall [6].

1.2.1.1.4. Rib Pillar Extraction Method

Rib pillar extraction refers to a series of methods that can be regarded as a combination of pillar extraction and short wall methods.

The term 'rib pillar' was coined in South Africa to describe a series of methods that are based on the extraction of a rib of coal between development roads and the goaf[6], with a solid block of coal providing the major means of support in the workings.

1.2.1.1.5. Sub-level Extraction Methods

Sub-level extraction in coal mining usually is applied only in coal seams where the nature of the seam excludes the practical application of other coal mining methods.

The method basically consists of driving a series of sub-levels commencing at the top of the ore body. A starting vertical slot is cut and then a series of ring patterns are drilled and blasted, the broken coal being drawn off after each blast. In South Africa there are very limited deposits of coal that would be suitable for this application.

1.2.2. Mining Equipment

Primary coal mining equipment is as follows:

[6] The empty area left by the extraction, which, however, is soon filled up by falls of stone from the strata overlying the bed. See figure 1.3.

- Continuous miners and Shearers: These are the major cutting machines. Continuous Miners are usually used in room and pillar-mining method while Shearers are popular in long wall.

- For transporting coal out of the mine, loaders, shuttle cars, continuous haulages and conveyors are usually employed.

- For health and safety purposes, roof supports, dust collectors, ventilation equipment (e.g. jet funs) are used among other equipment.

Components of the long wall mining system and the continuous miner are shown in figures 1.3 and 1.4 respectively.

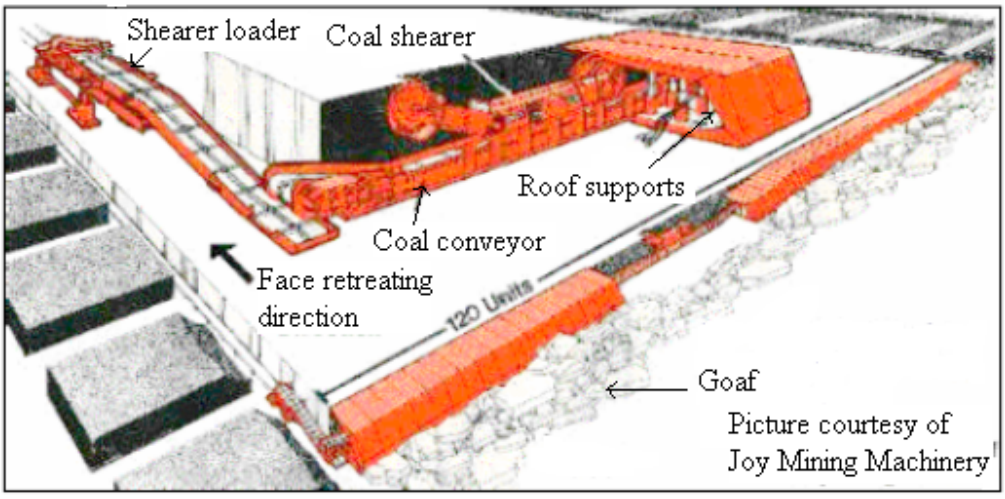

Figure 1.3: Perspective and closed-up views of a long wall mining system [7]

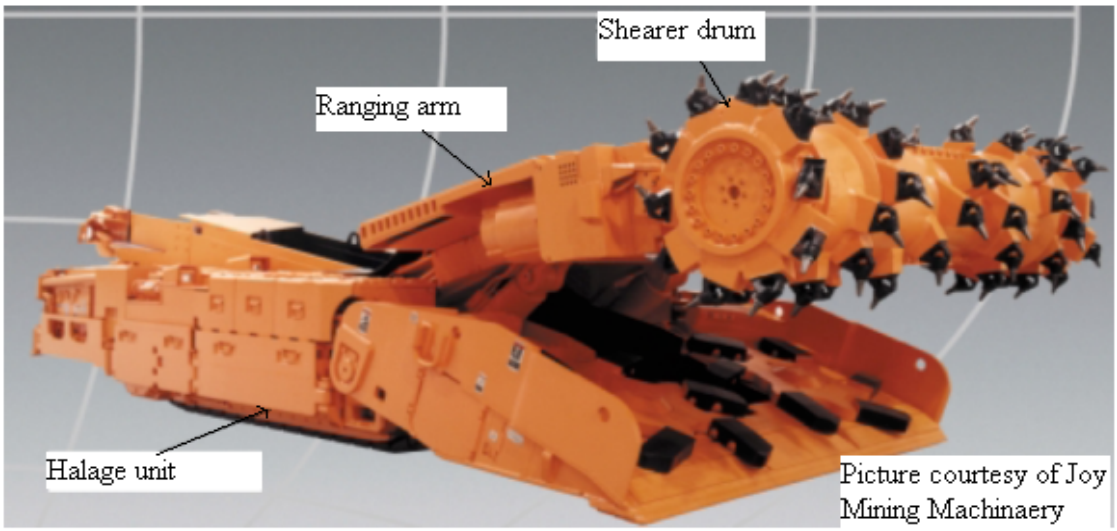

Figure 1.4: A Joy 14 CM Series Continuous Miner [7]

1.2.3. Health and Safety Hazards

Airborne Respirable Dust (ARD) and methane are the two common problems encountered in underground coalmine. In the quantitative risk assessment for thick-seam / long wall operation [1], using field data, dust was identified as both an explosion and a health risk in the rankings of 2 and 1 respectively, see Appendix A.

1.2.3.1. Coal Dust

1.2.3.1.1. Description of Coal Dust

The fine coal and rock particles produced in underground mining are called dust. The sizes of the dust particles are denoted by their average diameter in micrometre, abbreviated µm (1 µm = 10^{-6} mm). The dust that is suspended in and moves with the air ventilation flow is the airborne dust and that which settles down on the floor is the settled

dust. Dust concentration is the amount of airborne dust contained in one unit of air volume. It is generally represented by the total weight in milligrams per cubic metre (mg/m³) or sometimes by number of dust particles in one cubic centimetres of air volume. In this document the former is used.

The amount of airborne dust made per tonne of raw coal produced, A_d, can be determined by:

$$A_d = \frac{q_d Q_{air} T}{A_s} \qquad (1.1)$$

Where q_d is the average dust concentration per shift in mg/m³, Q_{air} is the air volumetric flow rate in m³/min at the location where the dust concentration is measured; T is the dust sampling time in minutes, and A_s is the shift production in tonnes.

The amount of airborne dust and its duration in the airflow depend not only on the sizes, shapes, and weight of the dust particles, but also on the air velocity and humidity. As these factors change, the airborne dust may be converted to the settled dust or vice versa [1].

1.2.3.1.2. Sources of Coal Dust

Mechanized coal and stone operations, more concentrated workings, wide spread use of powered supports and thus more caving of wastes with a more rapid advance of coal face, have all contributed to the increased production of dust in recent years [2].

Most of the dust produced is formed and dispersed at the coalfaces, and at various places in the intake airways, which thus contaminate the air supplying the coalfaces.

There are two primary causes of dust production in mines:

- Mechanical breakage and disintegration of the coal and adjacent strata during mining operations, and in some cases dispersion during mining operations of dust already present in the slips and bedding planes.

  Since coal rocks are brittle, their mining in any form gives rise to a wide range of breakage products, of which a more or less constant proportion is dust.

  The presence of pre-formed dust in bedding and cleavage planes is dependent upon the coal structure and geological conditions. This inherent dust is released and dispersed whenever the strata are broken during mining operations.

- Degradation and agitation of material during transportation.

  The coals are further broken down and more dust is produced during transportation by conveyors and loaders, especially at the transfer points.

In addition to the basic sources of dust formation and dispersion there is also the problem of disturbing and re-dispersing dust that has settled out of the ventilation current. Dust can be re-dispersed by high air velocities or by the movement of people and machinery.

According to underground measurement, the airborne dust concentration in coalmines can reach 286.7 mg/m³ and 120 mg/m³ when excavating hard and soft coal respectively [2]. If the roof and the floor rocks are included in the cutting, the airborne dust increases significantly.

1.2.3.1.3. Coal Dust as a Health Hazard

If miners are exposed to ARD for a long time, the inhaled coal dust could cause health hazards ranging from minor bronchial disorders to pneumoconiosis or silicosis. The latter is the most widely recognized occupational disease in coal mining and is commonly referred to as Coal Workers' Pneumoconiosis (CWP) or black lung. The concentration of the CWP can be attributed to the following factors:

- **Dust Size**: The airborne dust contains various sizes of dust particles. Once the airborne dust is inhaled by the human being, due to their own weight and air impact, the larger particles will settle on the membranes of the bronchial tubes before they reach the lung. On the other hand, the fine particles, that is, those with diameter less than 5 μm, will be able to reach the lungs. These fine particles account for a large proportion of the airborne dust, sometimes up to 80% [1]. The fine particles that can penetrate into the nonciliated space in the lung and lead to pneumoconiosis are the respirable dust.

- **Free Silica**: The amount of free silica in the airborne dust is directly related to the rate of development and severity of the pneumoconiosis. But only a small amount of free silica is associated with the airborne dust in the coalmines.

- **Dust Concentration**: The amount of respirable dust that enters the lung is proportional to the dust concentration and the duration of contact with the airborne dust. Therefore if effective methods are employed for controlling the dust generation and/or dust flows, the dust concentration can be greatly reduced. Under this condition, the amount of respirable dust inhaled will be too small to cause pneumoconiosis even after long-term exposure.

1.2.3.1.4. Degradation of Working Environment by Coal Dust

Airborne dust particles of all sizes may cause irritation of the eyes, ears, nose and throat, and also result in skin irritation where the temperature and humidity are high. Small electrical relays, switches, hydraulic circuitry, machine and motor bearings can all suffer from abrasive dust and cause delays, with a possible loss of production. If the air at the face area is filled with airborne dust, it is very difficult to make the visual inspection required constantly for operating the machines and roof conditions. This may lead to accidents.

1.2.3.1.5. Coal Dust as Cause of Dust Explosion

When the concentration of the airborne dust with particle sizes ranging from 25 - 100 µm reaches certain limits, dust explosion will occur provided the following conditions prevail:

- The coal dust is more liable to explode as the amount of volatile matter in the coal increases. But this cannot be used as the only criterion because the composition of coal is rather complicated.

- All airborne dust particles smaller than 100 µm contribute to dust explosion. But the most dangerous range is from 25 to 75 µm.

- There must be a sufficient dust concentration to initiate dust explosion. The lower limit ranges from 30 to 40 g/m³ in clean air (i.e. no methane).

- The presence of methane will lower the limit of dust concentration for initiating dust explosion.

- Dust explosion also requires a minimum temperature for ignition, which is generally from 700 to 800 ºC, sometimes even up to 1100 ºC. During dust explosion, the air temperature will reach well above 2000 ºC. This is accompanied by extremely high air pressure. As a result, the shock wave will scoop up the settled dust into the airflow, prolonging the explosion.

Therefore coal dust constitutes a large threat to the health and safety of coal miners. It must be efficiently and effectively controlled.

1.2.3.2. Methane

1.2.3.2.1. Description of Methane

In general, mine gas refers to all the hazardous gases in mines. The most frequently encountered hazardous gases in underground coalmines are methane (CH_4), carbon monoxide (CO), sulphur dioxide (SO_2), hydrogen sulphide (H_2S), nitrogen dioxide (NO_2) and hydrogen (H_2).

Methane is the major component of the hazardous gases in the underground coalmines occupying approximately 80 – 96 percent by volume. Methane is a colourless, odourless, flammable gas. Its diffusivity[7] is about 1.6 times that of air. Since it has a low specific gravity[8] (0.554), methane is easily accumulated near the roof of the roadway and working faces in the mine.

[7] **Diffusivity** is classically defined as the mass of solute transferred per unit area per unit time under unit concentration gradient.

[8] **Specific density** is the ratio of the density of a given solid or fluid substance to the density of water at a specific temperature and pressure. It is unit less.

The amount of methane emission in an underground coalmine can be expressed either by the absolute amount or the relative amount of emission. The absolute amount of emission (Q_{gas}) is the absolute amounts of emission per unit time in the whole mine. Its volumetric unit will be m³/day or m³/min. However, the relative amount of emission (q_{gas}) is the average amount of emission per tonne of coal produced within a certain period of time.

1.2.3.2.2. Sources of Methane

During the coalification process, the coal forming materials, which consist mainly of plants, undergo a series of physical and chemical reactions and produce a large volume of methane. After that, the coal is subjected to metamorphism and undergoes changes in chemical composition and structure under high pressures and temperatures. Metamorphism process also produces methane. In general the amount of methane produced is proportional to the ranking of metamorphism, see table 1.1.

Table 1.1: Methane Produced by Various Ranks of Coal (Source: Curl, 1978)

Rank	Lignite	Low Volatility Bituminous	High Volatility Bituminous	Semi Anthracite	Anthracite
Methane (m³/tonne)	68	230	270 -290	330	400

Most of the methane produced during coalification and metamorphism escapes to the atmosphere through fissures in the strata. A small amount stays in the fissures and still

another small amount remains in the coal. This is the methane that is commonly referred to mine gas.

1.2.3.2.3. Methane as a Hazard to Miners

Although methane is harmless to breath in small quantities, it is suffocating if its concentration is very high. The most dangerous problem with methane is the potential of methane explosion. There are three requirements for methane explosion: minimum concentration of methane, minimum concentration of oxygen and a suitable heat source.

Under a certain temperature, methane will be ignited when its concentration is between 5 and 15 percent. When methane concentrations are 5%, it forms a bluish stable combustion layer around the flame without initiating explosion. When the methane content is larger than 15%, there is insufficient amount of oxygen to promote explosion [3].

The study conducted by John Frint in 1990, reviewed that between 1891 and 1990, a total of 155 explosions occurred in South African collieries that resulted to 799 fatalities [9]. Details are shown in Appendix B.

Based on the factors contributing to methane explosion, most of the preventive methods of methane explosions are based on reduction of methane accumulation and elimination of high temperature heat sources. Flint identified the heat sources for mine gas explosion and suggested their prevention methods. This study dwells on the control of methane and dust concentration by ventilation method.

1.2.4. Legal Requirements and Standards

One of the most important features in the control of environmental hazard is the establishment of standards by which the quality of relevant aspect of the environment may be judged objectively.

In the coal mining industry worldwide there are also different legal requirements and standards for ARD and methane concentration for different countries. The United States Federal Coal Mine Health and Safety Act of 1969, limits personal exposure to respirable dust to 2.0 mg/m³ and the concentration of methane 1%. A directive of the South Africa Department of Minerals and Energy (DME, 1997) required the dust concentration level to be reduced below 5 mg/m³ at the operator's position [10]. This figure is now being reduced further to 2 mg/m³. And methane concentration in South African coalmines should be kept below 0.5%.

1.2.5. Airborne Dust and Methane Control in Coalmines

Years of continuous research, development, investigation and experience have produced a number of techniques and a variety of equipment which can be applied to limit and control concentration of ARD and methane. Unfortunately, a single solution that can reduce the concentrations to the required standards is yet to be found. Most of the present methods yield only 25 to 50 percent reductions in respirable dust. Thus, several methods are used simultaneously, usually without knowing for sure how well any individual method is working [11].

Coal Dust Control – Dust control in the coalmines can be divided into three major categories: ventilation, water, and dust collection. Since this research is mainly concerned with ventilation method, more details are given on this area while general information is covered on the rest.

Methane Gas Control - There are three requirements for methane explosion: minimum concentration of methane, minimum concentration of oxygen and a suitable heat source, as mentioned before.

Based on the factors contributing to methane explosion, most of the preventive methods of methane explosions are based on reduction of methane accumulation and elimination of high temperature heat sources. This study dwells on control of methane concentration by ventilation method.

1.2.5.1. Ventilation Systems for Development Headings

Methane Control – The primary function of ventilation is to dilute and remove mine gas. The amount of air required for methane dilution is greater than that for dust reduction. For example, in the USA the fresh air required at the long wall face is from 510 to 1417 m^3/min. In methane rich seams, it is not unusual to have the fresh air intake at the rate of 1840 m^3/min [3]. Ventilation also reduces the temperature in the mine since high-temperature contributes to methane explosion.

Dust Control - Ventilation air reduces dust through both dilution and in some cases, displacement. The dilution mechanism operates when additional air serves to reduce the dust concentration by diluting the dust cloud surrounding the workers. The displacement mechanism operates when workers are upwind of the dust source and the air velocity is high enough to reliably keep the dust downwind.

The minimum quantities of air are prescribed by the Mines and Works Regulations, which require that, throughout the 24 hours, the face should be provided with 0.001m^3/sec of air per 25 multiplied by the mass of coal mined in tonnes per shift, and further that the velocity of air over the working height shall be not less than 0.25 m/sec [4]. The velocity of the air current at which dust pick-up may start to be troublesome is

2.5 – 3.0 m/s[9]. Therefore it should be ensured that the air speed must not reach dust picking levels. This conflicts with the necessity of removing methane [4].

1.2.5.1.1. Jet Fans

At the beginning of underground coal mining ventilation was accomplished through natural drafts [2]. In modern days fans and ventilation shaft are used for ventilation purposes.

Jet fans are predominantly used for longitudinal ventilation and are positioned at heading entrance near to the wall opposite the CM as shown in figure 1.5. The standard position for the jet fan is 1.2 m from the heading entrance, 1 m from the side wall and 0.7 m from the floor. Modern jet fan have variable pitch and speed control as well as reversible flow direction.

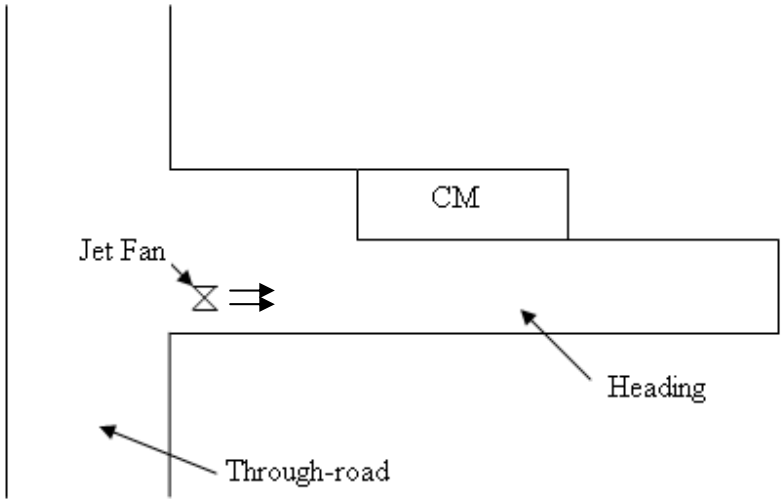

Figure 1.5: Plan view showing the position of the fan in the coalmine

[9] This figure however depends on the inherent moisture in the coal, particle size and method of working.

Due to the heading being blind air from the fan end up circulating and re-circulating resulting into inefficient control of ARD and mine gas. To overcome the re-circulation problem some auxiliary equipment like ducts are sometimes used.

1.2.5.1.2. Fan and Duct System

Ventilation by means of duct can be exhaust, forcing or overlap; these are described in details in the following sections:

Exhaust System

Exhaust ventilation system consists of main exhaust duct, to which a duct fan is attached on its suction side in the heading as shown in figure 1.6. With exhaust system relatively clean air passes the miners and the extracted dust is fed via the fan into the return air stream. There are, however, two disadvantages. Firstly, if firedamp is a problem, pockets of mine gas could accumulate at the face of the heading, together with possible roof layering because of the low velocity and limited scouring action of the airflow.

Secondly, the dust exhausted from the face of the heading may contaminate the ventilation used to supply other working places. The second problem may be overcome by using dust collector to take out a large part of the airborne dust before the air is used again [2]. However, if gas emission is a problem, then an overlap system should be considered.

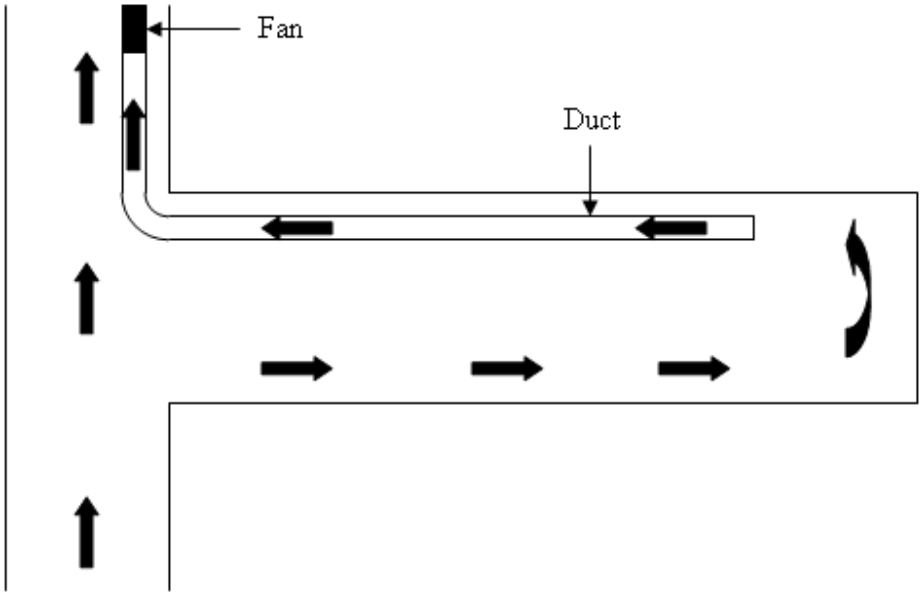

Figure 1.6: Exhaust duct ventilation system [11]

An exhaust ventilation system can be equipped with extra ventilation devices, such as: air curtain on a CM, jet fan in working face zone and air cooler at a certain distance from the face zone [11].

Forcing System

A forcing ventilation system consists of the main duct line, to which a duct fan is attached on its forcing side in the heading with through air shown in figure 1.7. Forcing ventilation is characterized by blowing a greater quantity of airflow rate to the heading face than exhaust ventilation. This makes it the best system for dealing with firedamp [11]. The forcing system, however, has the disadvantage of exposing the miners to airborne dust of maximum concentration on its return journey along the roadway [2]

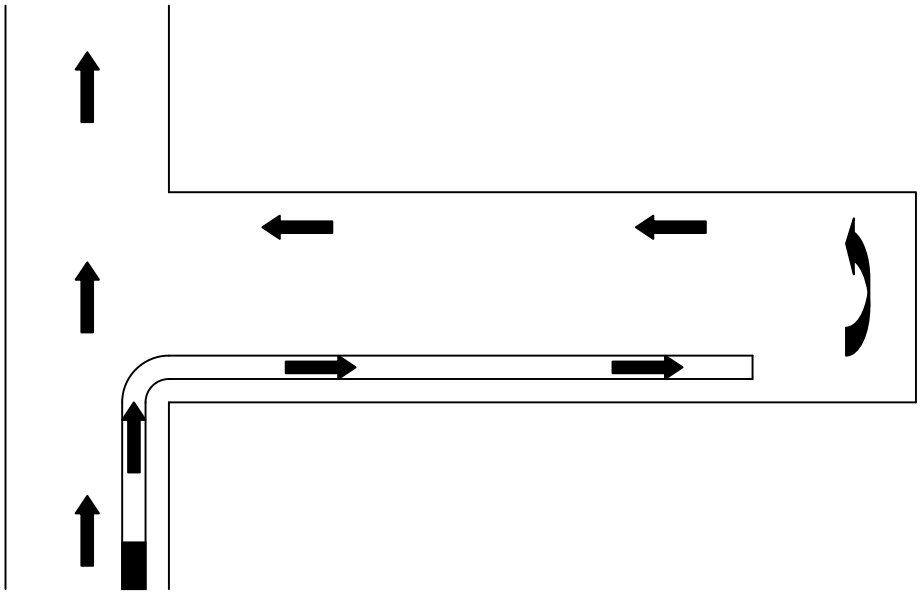

Figure 1.7: Forcing duct ventilation system [11]

Forcing ventilation system can be equipped with extra ventilation devices, such as: air cooler with an auxiliary fan located in the main forcing duct and/or a cooler in an auxiliary duct located in the working face zone [11].

Forcing System with Overlap

The forcing system with overlap, shown in figure 1.8, is the one recommended where possible [2]. The forcing section is the main part of the ventilation system and the short exhaust section is the secondary part for dust control, usually incorporating some form of dust collector. The forcing section gives a good scouring action at the face of the heading. It is normally necessary to use a diffuser at the delivery end of the forcing ducting to reduce the delivery velocity and dust pick-up. When it is necessary to cool air, a cooler is placed in the forcing duct [11].

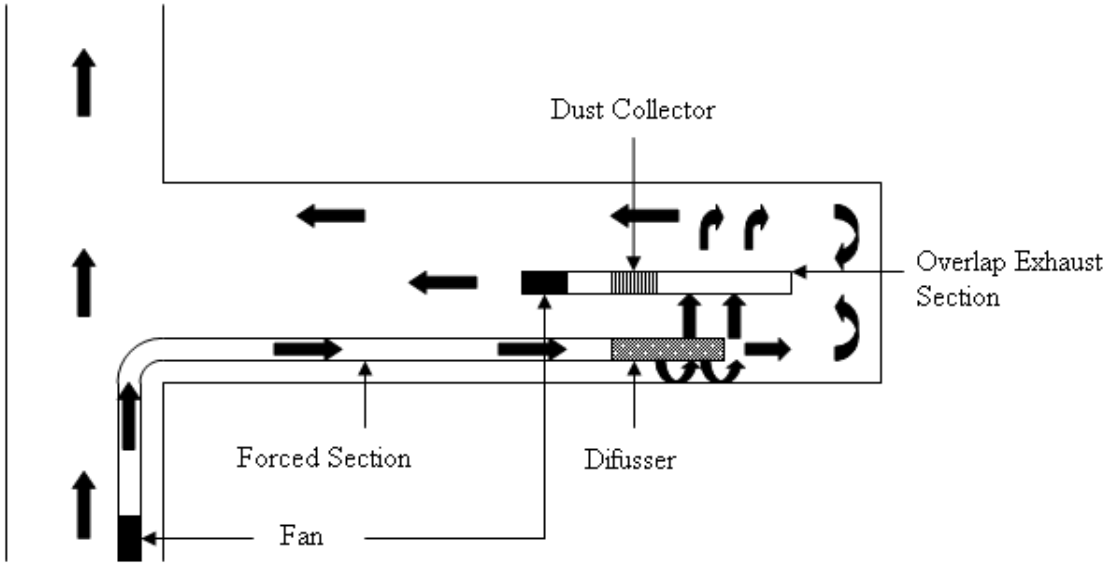

Figure 1.8: Forcing ventilation system with overlap [11]

Exhaust System with Overlap

As with forcing system with overlap, the exhaust system with overlap, shown in figure 1.9 combines the advantages of having a good scouring action from the forcing section, with the removal of the high dust concentration to bypass the workers. This system has the following solutions [11]:

- Short forcing duct with a vortex duct and duct hopper in the face zone in case of methane hazard.

- Short forcing duct with a vortex duct, a duct hopper in the face zone and a jet fan in the heading in case of extremely high methane hazard.

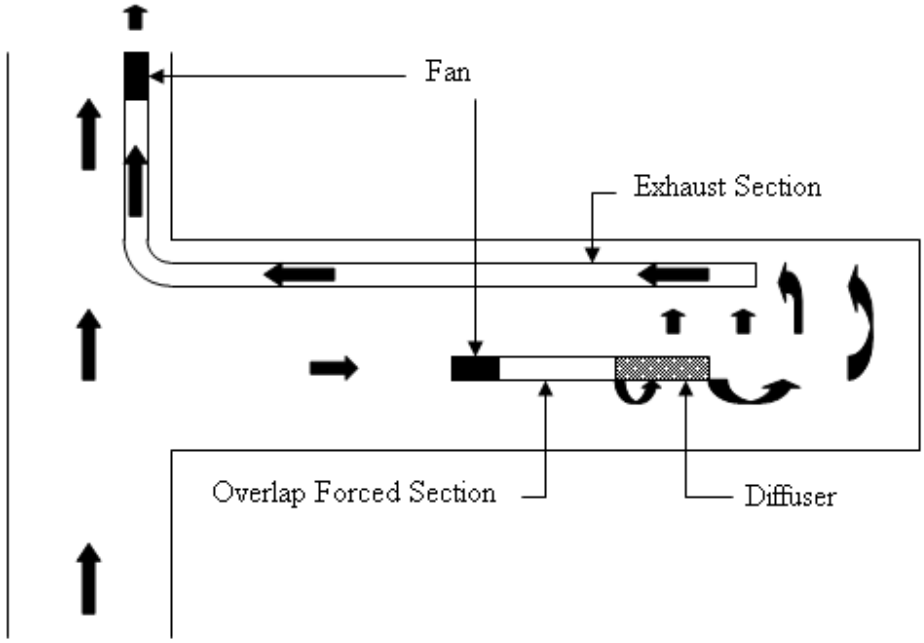

Figure 1.9: Exhaust System With Overlap [11]

A part from individual problems of fan and duct system mentioned under specific systems the general disadvantage of this system is that the equipment has to be adjusted as the heading depth progresses. Considering the harsh working environment in the mine, workers find it difficult to move the equipment around as a result this system is not applied in most of the mines.

1.2.5.2. Other Methods of Control

Ventilation is just one common method of controlling ARD and mine gas but there are also other methods that are used in addition to ventilation. This section describes some of the other popular methods.

1.2.5.2.1. Dust Control Methods

1.2.5.2.1.1. Use of Water

Once dust is airborne it is very difficult to control therefore it is necessary to suppress it at the source. Normally, water plays a bigger part in dust suppression in coalmine using methods like water spray and water infusion. The details of these methods can be found in reference [2].

Water is also used even to control airborne dust like in the wet scrubber and water curtains.

1.2.5.2.1.2. Dust Collection

Dust collectors are used to remove dust from air stream. Scrubber is the most popular dust extractor in the underground coalmines. Recently wet scrubber has proved to be more efficient as far as dust extraction is concerned.

1.2.5.2.1.3. Surfactants

Surfactants are chemicals that are added to spray water in order to increase its effectiveness in terms of dust suppression. Surfactants help to bond the dust particles together so that they are not easily become airborne in case of high air velocities or mine explosion.

1.2.5.2.1.4. Cutting techniques

Good cutting techniques by using appropriate cutting machine for a specific coalmine help to reduce the amount of dust production. For more information see references [1][2][3] and [6].

1.2.5.2.2. Methane Control

Usually, methane accumulates to high concentration in the gob. In the USA the gobs are ventilated to prevent methane accumulation and to reduce temperature. In most other countries the gobs are tightly sealed such that it completely cuts off any fresh air flowing into the gob or prevents high-concentration methane flowing out of the gob.

If the coal seam has high methane content methane drainage is considered. Methane drainage involves drilling boreholes into the solid coal, the roof and sometimes the floor. The withdrawn methane is used as fuel or as a raw material for chemical by-products.

The other method of preventing the accumulation of methane in the mine is water infusion. This involves drilling in-seam horizontal holes into the solid coal ahead of mining. High-pressure water is injected into the boreholes and moves away in a cylindrical waterfront. As the water moves away from the borehole, the methane is also driven away.

1.2.6. Previous work on underground coal mine ventilation

Since health and safety risks caused by ARD and methane where identified in coal mining numerous research work have been conducted in order to mitigate or eliminate their effects. In addition to the work described in the preceding sections this section gives

a summary of other works in the area of mining ventilation that is more relevant to this particular research.

1.2.6.1. VUMA-Network Simulation Software

VUMA-Network is a ventilation network simulator that was jointly developed by the Mining Technology Division (Miningtek) of the Council for Scientific Research (CSIR) and Bluhm Burton Engineering Pty. Ltd. in South Africa [13]. VUMA-Network is an interactive program that allows the simultaneous modeling of airflow as well as contaminant and thermodynamic behavior in mine ventilation networks. The VUMA-Network can, however, be used to simulate airflow only.

Miningtek performed a simulation of the ventilation network of a South African coalmine that lead to the following conclusion of VUMA-Network simulation software:

- VUMA-Network is capable of simulating a coalmine ventilation system to a high degree of accuracy.

- The benefit of using a simulation tool such as VUMA-Network is that the results can be viewed graphically.

- The effect of various changes to the existing ventilation network can be easily assessed.

- Real benefits can be derived in areas of airflow distribution and fan power requirements by using VUMA-Network.

1.2.6.2. Kloppersbos Shear Spray Curtain (KSSC) Dust Control System

The extensive full-scaled simulation studies in the ventilation tunnel at the CSIR resulted in a new Kloppersbos Spray System and the development of new dust-control systems. They are the half-curtain, the retrofitted hood system, double scrubber system and the integrated system [14].

According to Bell, in more than 80% of the new dust-control systems were being operated in South Africa mines in 2002. The half-curtain dust-dust control system was the most successful of them all. Test carried out on the half-curtain system in the Kloppersbos ventilation simulation tunnel showed that effectively dilutes the methane released at the face at a rate of 600 L/min (Van Zyl *et al*., 1999).

A typical half-curtain dust-control system is fitted with:

- Hollow-cone spray nozzles with inlet and outlet diameters of 1.6 and 2.0 mm respectively.
- A directional spray system.
- Air movers fitted over the flight conveyor.
- An extended scrubber intake, with an inlet cone fitted.
- A physical air curtain.

1.2.7. Literature on CFD

As already defined in footnote 4, CFD stands for Computational Fluid Dynamics and it deals with the entire study field of fluid mechanics using computational method.

In this work, the author would like to investigate if CFD can be used to study air flow in a scaled-down underground coalmine. It is for this reason that the basic differential equations on which all CFD packages are built introduced.

1.2.7.1. Governing Equations and Boundary Conditions

1.2.7.1.1. Basic Equations

The fundamental equations for compressible viscous flow of a fluid are based on the three laws of conservation for a physical system [15]:

I. Conservation of mass (continuity)
II. Conservation of momentum (Newton's second law)
III. Conservation of energy (first law of thermodynamics)

The three unknowns that can be obtained simultaneously from these three basic equations are the velocity **V**, the thermodynamic pressure p, and the absolute temperature T. Thermodynamic pressure and absolute temperature considered as independent thermodynamic variables. However, the final forms of the conservation equations also contain four other thermodynamic variables: the density ρ, the enthalpy h (or the internal energy e_i), and the two-transport properties μ (viscosity) and k (conduction).

In order to specify a particular problem completely, the conditions (of various types) for **V,** p and T must be known at every point of the boundary of the flow regime. The

preceding considerations however apply only to fluid of uniform, homogeneous composition.

Please note that all the three basic laws are formulated for particles (systems) of fixed identity. Thus, in the Eulerian system appropriate to fluid flow all the three laws utilize the particle derivative

$$\frac{D}{Dt} = \frac{\delta}{\delta t} + (V \bullet \nabla) \qquad (1.2)$$

The following partial differential equations were derived for general control volumes, expressed in Cartesian coordinates (fn):

Conservation of mass: the equation of continuity

$$\frac{D\rho}{Dt} + \rho . \nabla \bullet V = 0 \qquad (1.3)$$

with

$$\nabla \bullet V = \frac{\delta u}{\delta x} + \frac{\delta v}{\delta y} + \frac{\delta w}{\delta z}$$

Where: $\boldsymbol{V}$ = velocity vector (column) in m/s

ρ = density in kg/m^3

x, y, z = space coordinates in 3D in metres

u, v, w = velocity components in m/s

t = time in seconds

Equation (1.3) is the steady, three-dimensional mass conservation or continuity equation at a point in a compressible fluid. The first term on the left hand side is the rate of change in time of the density. The second term describes the net flow of mass out of the element across its boundaries and is called the convective term.

I. Conservation of momentum: the Navier – Strokes (fn) equations

The Navier – Strokes equations express proportionality between applied force and the resulting acceleration of a particle of mass. This is the reason it is also commonly known as Newton's second law.

In scalar form, the Navier – Strokes equations are presented as follows:

$$\rho\frac{Du}{Dt} = S_{Mx} - \frac{\delta p}{\delta x} + \frac{\delta}{\delta x}\{2\mu\frac{\delta u}{\delta x} + \lambda\,\nabla\bullet V\} + \frac{\delta}{\delta y}[\mu\{\frac{\delta u}{\delta y} + \frac{\delta v}{\delta x}\}] + \frac{\delta}{\delta z}[\mu\{\frac{\delta w}{\delta x} + \frac{\delta u}{\delta z}\}] \tag{1.4}$$

$$\rho\frac{Dv}{Dt} = S_{My} - \frac{\delta p}{\delta y} + \frac{\delta}{\delta x}[\mu\{\frac{\delta v}{\delta x} + \frac{\delta u}{\delta y}\}] + \frac{\delta}{\delta y}\{2\mu\frac{\delta v}{\delta y} + \lambda\,\nabla\bullet V\} + \frac{\delta}{\delta z}[\mu\{\frac{\delta v}{\delta z} + \frac{\delta w}{\delta y}\}] \tag{1.5}$$

$$\rho\frac{Dw}{Dt} = S_{Mz} - \frac{\delta p}{\delta z} + \frac{\delta}{\delta x}[\mu\{\frac{\delta w}{\delta x} + \frac{\delta u}{\delta z}\}] + \frac{\delta}{\delta y}[\mu\{\frac{\delta v}{\delta z} + \frac{\delta w}{\delta y}\}] + \frac{\delta}{\delta z}\{2\mu\frac{\delta v}{\delta z} + \lambda\,\nabla\bullet V\} \tag{1.6}$$

Where in addition to the variables in defined in equation 1.3,

	μ	=	Viscosity due to linear deformation in kg/m.s
	λ	=	Viscosity due to volumetric deformation in kg/m.s
And	S_M	=	Body force in Newtons in directions x, y and z of equations 1.4, 1.5 and 1.6 respectively.

II. Conservation of energy: (first law of thermodynamics)

With the assumption that Fourier's law governs the heat transfer to the element volume[10], the energy takes the final form of:

$$\rho \frac{Dh}{Dt} = \frac{Dp}{Dt} + div\,(k\nabla T) + \Phi \qquad (1.7)$$

Where: Φ = dissipation function or deformation heating[11]
k = conduction of continuum in W/mK
h = enthalpy in kJ/kg
P = pressure in Pascal

The basic equations given in this section are used to derive CFD codes.

1.2.7.1.2. Boundary Conditions

Any CFD model is as good as the assumptions it is based on. One can have a sufficiently converged solution, but if the boundary conditions do not resemble the reality, the solution is useless. Thus, it is very important to apply the correct boundary conditions.
In this research were the fluid in question is incompressible and viscous (air), the boundary conditions are given in table 1.2.

[10] Fourier's law: $q = -k\nabla T$ where: q = the vector heat flow per unit area in W/m^2; k = conduction of the continuum in W/mK; T = absolute temperature in K/m.

[11] The dissipation function Φ involves the viscous stresses. It is always positive definite [15].

Table 1.2: Boundary conditions for compressible viscous flow

Initial conditions for unsteady flows	Everywhere in the solution region	ρ, $\boldsymbol{V}$ and T must be given at time $t = 0$
Boundary conditions for unsteady and steady flows	On solid surfaces	$\boldsymbol{V} = \boldsymbol{V}_w$ (no-slip condition) $T = T_w$ (fixed temperature)
	On fluid boundaries	Inlet: ρ, $\boldsymbol{V}$ and T must be known as a function of position
		Outlet: $-p+\mu\frac{\delta u}{\delta n} = F_n$ And $\mu\frac{\delta u}{\delta n} = F_t$ (stress continuity)

1.2.7.2. Solving Methods

Solving complex fluid flow problems using the differential equations requires a numerical approach. A numerical solution of a differential equation consists of a set of numbers from which the distribution of the dependent variables can be constructed. This is different from the analytical solution that describes the continuous values throughout the domain thus an infinite amount of values of the dependent variables.

In numerical method the governing Partial Differential Equations (PDE) are replaced with simple algebraic equations, which can be solved with relative ease. This is achieved by replacing the continuous information contained in the exact solution of the differential equation with discrete values (of dependent variables) at a finite number of given points in the domain. This is referred to as discretisation.

To convert the governing Partial Differential Equations (PDE) to a system of algebraic equations (or ordinary differential equations), a number of choices are available. The

most common are the finite difference, finite element and spectral methods. In this dissertation the Finite Volume Method (FVM) formulation, which falls under finite difference method is used. This is because the resulting statements of the control volume integration express the exact conservation of relevant properties of each finite size cell and is central to the most well established CFD codes like CFX/ANSYS, FLUENT, EFD Lab, PHOENICS and STAR-CD. Since FVM is used in this research as a solving method, it is the only one that has been described in this dissertation. For the sake of the readers who are interested in the other methods, refer to references [15-19].

In outline the numerical algorithm consists of the following steps:

- Integration of the governing equations of fluids flow over all the finite control volumes of the domain.

- Discretisation – conversion of the resulting integral equations into a system of algebraic equations.

- Solution of the algebraic equations by iterative method

1.2.7.3. Pre-processing: Geometry Development and Mesh Generation

Any CFD flow problem starts with the preparation of geometry using CAD software, as well as dividing the geometry into cells, called the mesh or grid before any modelling is done.

Most commercial CFD packages use their own pre-processor to generate both the geometry and mesh.

Different mesh strategies exist: structured, unstructured, hybrids, composite and overlapping meshes. The choices of numerical methods (discretisation equations) and models to be used, and meshing strategies, are strongly interdependent. The success of simulation depends on appropriate choices for most CFD problems.

1.2.7.4. Finite Volume Method

The Finite Volume Method (FVM is one of the most versatile discretisation techniques used in CFD. Based on the control volume formulation of analytical fluid dynamics, the first step in the FVM is to divide the domain into a number of control volumes[12] where the variable of interest is located at the centroid of the control volume. The next step is to integrate the differential form of the governing equations over each control volume. Interpolation profiles are then assumed in order to describe the variation of the concerned variable between cell centroids. The resulting equation is called the discretised or discretisation equation. The discretised equation expresses the conservation principle for the variable inside the control volume and its result satisfies the conservation quantities such as mass, momentum, energy, and species. [19]

FVM is ideal method for computing discontinuous solutions arising in compressible flows and solving partial differential equations containing discontinuous coefficients.

1.2.7.5. Convergence Theorem

The quality of simulation results depends upon convergence and grid independence. A solution of the algebraic equations that approximate a given PDE is said to be convergent if the approximate solution approaches the exact solution of the PDE for each value of the independent variable, as the grid spacing tends to zero.

[12] Also referred to as cells or elements

In Star CCM+ convergence is judged by residual monitor plots. The residual in each cell represents the degree to which the discretised equation is not completely satisfied. The residual plot is a monitor plot that is automatically created from the active residual monitors on semi-log axes when iterating starts [20]. A sample residual plot is shown in figure 1.10.

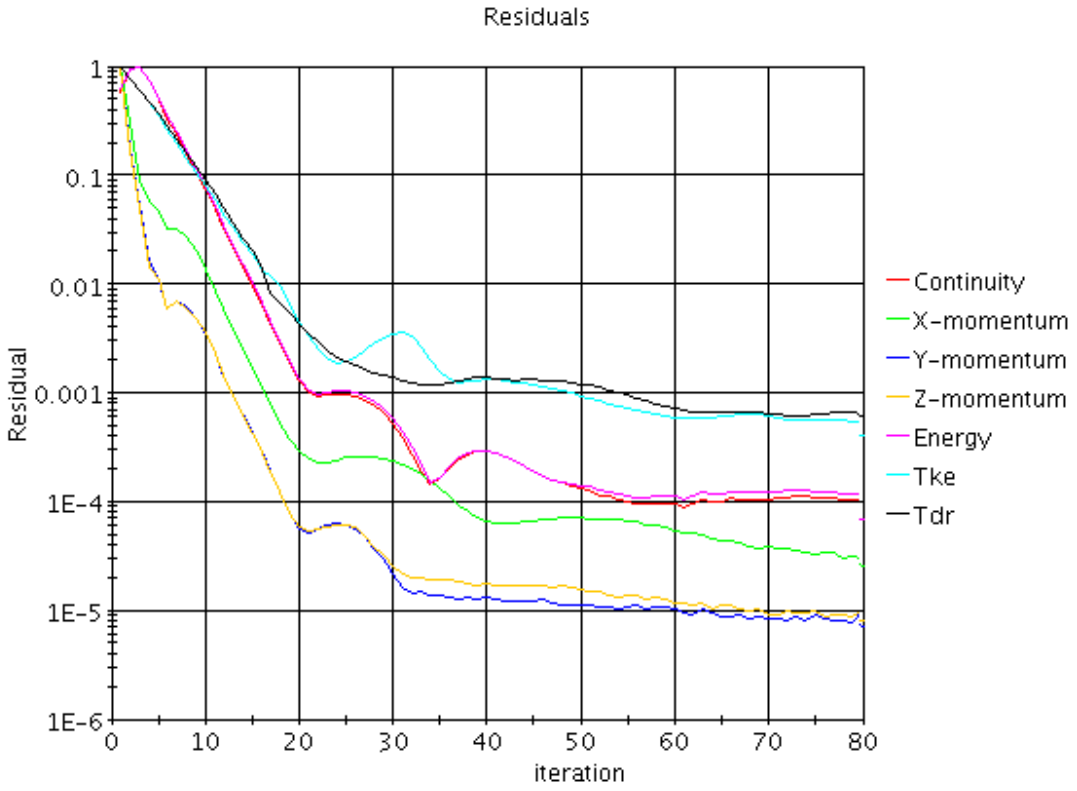

Figure 1.10: A sample converging residual plot [20]

Residual quantity will tend toward a very small number when the solution is converged and will increase in number when it is diverged.

1.2.8. Design Optimization

This section briefly describes design optimization of CFD model.

1.2.8.1. Base Case Evaluation and Model Perfection

A first step in optimization process is to identify a physical process to be optimized. This physical process is called the base case in the optimization process. Then the base case is evaluated in the CFD code and compared to with the actual physical process results. All the relevant meshing strategies, assumptions made and models chosen in the CFD code are experimented with in order to perfect the CFD model of the base case.

Evaluating the base case usually gives the user insight into the problem and can lead the user to identify suitable parameters or variables that have a marked influence.

1.2.8.2. Identifying Objectives and Parameters Constraint Functions

Optimization seeks to change design variables of an identified base case in such a way that the objective function is achieved. In choosing the objective function it must be ensured that its parameters or variables can be minimized for the optimum solution. Constraint functions that restrict the achievement of the set objective are also identified.

1.2.8.3. Parameterization of CFD Model

The more variables to be optimized, the more perturbations[13] are essential for the optimizer to predict the next optimum design iteration. Parameterization is can be done by most of the CFD commercial software.

[13] Small changes in terms of optimization process.

1.2.8.4. Design Optimization

The optimization process begins by iteration of the base case and its perturbations and moves on until the established objective function is approximated. In other words, the solution to the preceding iteration is used to do to succeeding iteration. This process is carried on until the objective function converges to a constrained minimum.

1.2.8.5. Experimental Validation

It is impossible to assess the validity of models of physics and chemistry embedded in a program as complex as a CFD code or the accuracy of its final results by any means other than comparison with experimental test work [21].

In case the validation using the actual system or process results into high financial, environmental or any other undesirable implications, other experimental validations can be considered. In this dissertation, the CFD model was validated with the experimental results done using scaled down physical model of an underground coalmine in the aerodynamics lab at the University of Pretoria.

1.2.9. Conclusion of Literature Review

The literature study has reviewed the following concerning ARD and methane problem in the underground coalmines:

- There is no single efficient method of controlling ARD and/or methane concentration levels.

- Although ventilation methods seems to be a better method of controlling both methane and dust, the existing techniques do not allow air reach some of the most critical areas of the mine.

- Most of the dust control techniques were developed in the USA for low-seam long wall mines (seam heights up to 2.5m). The applications of these techniques are limited to RSA high-seam conditions in which the operating seam height reaches 4.1m.

CHAPTER 2: PROBLEM STATEMENT AND METHODOLOGY

2.1. Introduction

This chapter explains the problem under investigation in details and explains the method that was used in the study in order to arrive at solutions.

2.2 Problem Statement

As it has been mentioned in the previous chapter, coal dust and methane gas are a hazard to coalmine workers and mining equipment.

To ensure safety of coalminers the South African government through the Department of Energy stipulated that dust concentration level in the underground coalmine should not exceed 2.0 mg/m³ at operator's position and methane level should not exceed the maximum concentration of 0.5% per volume [10]. A number of initiatives have been developed to mitigate these hazards but none seems to work effectively. Therefore, work has to continue to ensure that the standards are met or even exceeded for the benefit of the miners. Methods that are employed to control the hazards have been described in the literature study of which ventilation is popular.

Unfortunately, carrying out investigations in the underground coalmine proves to be difficult due to harsh conditions prevailing in the mine. The environment is too dusty, dump and dark to conduct experiments that can be meaningful. This problem brought out a need to develop methods of carrying out the investigations in an environment where the said conditions are excluded. A full scale model of underground coalmine was made and is located at Kloppersbos to eliminate the harsh conditions without compromising on quality of the results. Even after the full scale model was made it is too costly, in terms of money and time, to carry out investigation with it. Therefore there is a need to develop

a means of carrying meaningful investigations at low cost and less time. One way of achieving this is by using computer modeling and simulation.

This work was done in order to find out if CFD numerical method could be used to carry out ventilation related investigations for the underground coalmine.

2.3. Methodology

Numerical solutions can only be relied upon with confidence if they can be validated with experiments. Therefore, in this investigation experiments were conducted to validate the CFD results. Validation was achieved by comparing the numerical and the experimental results. Similarity of the results validates the numerical method. Two types of experiments and their related CFD simulation were done. They are steady and unsteady or transient states. The CFD models are discussed in chapter 3 and experimental model in chapter 4. Comparison between CFD and experimental results are captured in chapter 5.

In order to reduce the cost and time for the exercise a scaled down physical model was used instead of the full scale model. The scaling down of the full scale model is described first before experiment methods. It should be understood that the scale model was not used to represent a full scale mine but rather to validate a CFD model. This can later be extended to find out if the concept is applicable to a full scale mine later.

It should be noted in advance that scrubber was included in this study but it was difficult to visualize clearly the flow of air in the steady state experiments therefore it effects are not shown in steady state results. But the results in unsteady state include the effect of scrubber.

2.3.1. Scale Model

The scaled model that was originally designed and built by A.A. Daling [25] was used. The model was scaled down to 15% and is located in Aerodynamics Laboratory at the University of Pretoria. This section describes the concept, the scaling down and modification work done on the model in order to achieve the objectives.

2.3.1.1. Design Concept

The model shown in figure 2.1 comprises: a through-road, a heading, CM, jet fan and scrubber.

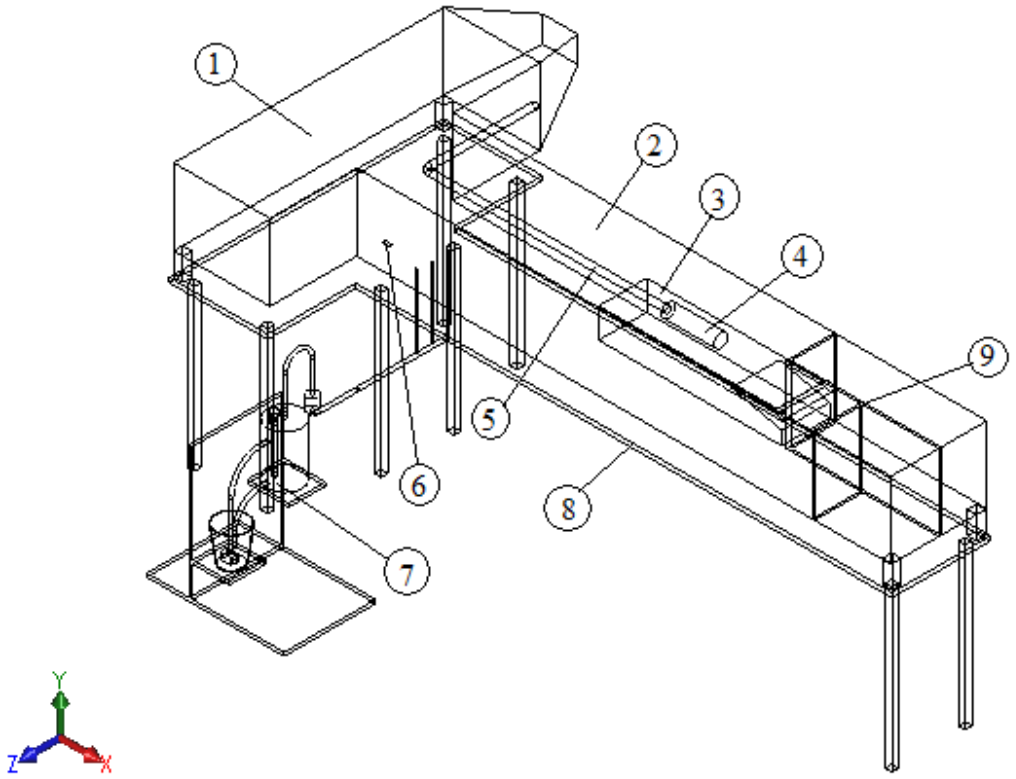

No	Description	No	Description
1	Through-road	6	Jet fan
2	Heading	7	Smoke System
3	Continuous Miner	8	Table
4	Scrubber	9	Partitioning mechanism
5	Flexible duct		

Figure 2.1: Coalmine Scale Model

The model was scaled down to 15% from the dimensions and quantities of actual mine as described in the next section.

The tapered end of the through-road on the model (please note that the actual through-road has not tapered end) is fitted with a fan that facilities air velocity in the through-

road. The tapered end was done for the purposes of creating a well developed flow in the through-road considering the size and shape of the fan used as compared to the size and rectangular shape of the through-road cross section.

It was not possible to find a jet fan scaled down to 15% with the same penetration as the actual fan; therefore the jet fan is represented in the model by a nozzle blowing air from a compressed air system [25]. The exit diameter of the nozzle that gives a similar penetration of the jet fan is 10 mm as calculated in 2.4.2.4.[25]

The left half of the coal seam, as seen from heading entrance, was made in such a way that it can be adjusted forward or backward. See a picture of the scaled model in figure 2.2. An addition mechanism to block the right half was also provided for in the design. These two mechanisms facilitated modification of model geometry to different shapes as the case in the actual mine when mining process is in progress.

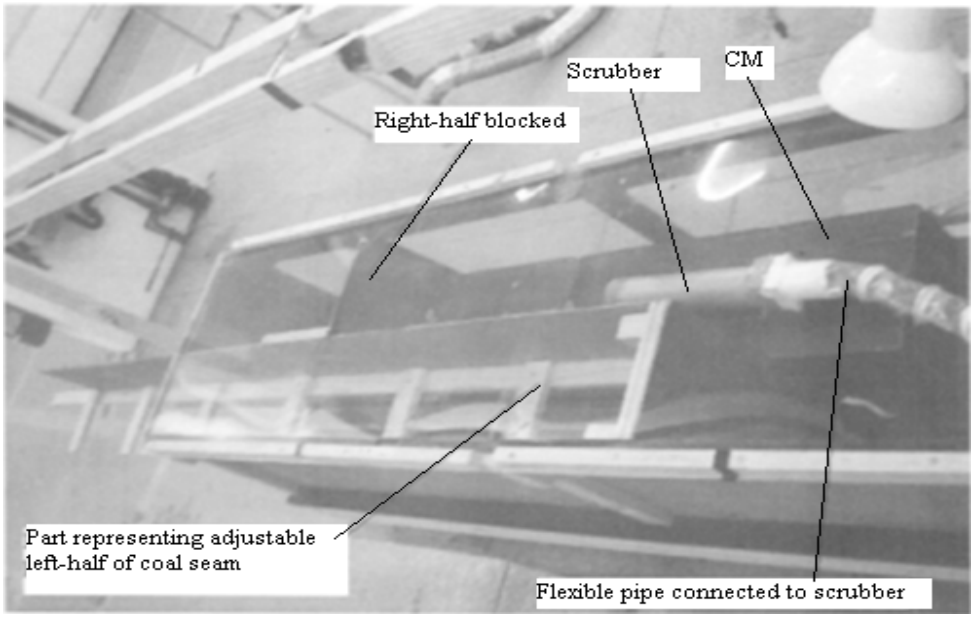

Figure 2.2: A picture of scaled-down coalmine model showing adjustable part of the heading representing coal seam.

The top and right side of the heading wall, as seen from heading entrance, are made of transparent plastic sheet. This is so to facilitate convenient observation of air flow when conducting the experiments. In addition, the top part can easily be removed in order to access the inside of the heading for the purposes of changing the geometry of heading, fixing sensors, setting the smoke tubes, etc.

2.3.1.2. Scaling

According to T. Prinsloo [25] who did an investigation for optimisation of air flow patterns in coalmines using the same scale model, the conversion of data from full scale model to 15%-scale model using physical phenomenon result into impractically high quantities. For example, using Reynolds number the exit air speed for scrubber was found to be 152 m/s. Therefore, air flows were scaled using percentage volume flow method. The percentage volume flow rate is the amount of air that is replaced by new air in relation to the entire volume of air in the volume of interest. And dimensions for the mine and CM were scaled down by geometrical method.

Please note that the intension here is not to represent a full scale mine by sing a scale model, but rather to validate a CFD model which can later be used to represent a full scale mine.

The following sections describe how the scaled down sizes and quantities, shown in table 2.1, were found as inspired by a full scale mine:

Table 2.1: The actual and scaled down dimensions and quantities of coalmine and equipment

Description		Actual Mine		Scale Model		Units
		Symbol	Value	Symbol	Value	
Heading	Length	L_{fh}	35	L_{mh}	2.333	m
	Width[14]	W_{fh}	6.3	W_{mh}	0.420	m
	Height	H_{fh}	5	H_{mh}	0.333	m
Through-road	Length[15]	L_{ft}	18	L_{mt}	1.200	m
	Width	W_{ft}	6.5	W_{mt}	0.420	m
	Height	H_{ft}	5	H_{mt}	0.333	m
	Air velocity	V_{ft}	2	V_{mt}	0.0665	m/s
CM	Length	L_{fcm}	12	L_{mcm}	0.800	m
	Width	W_{fcm}	3.6	W_{mcm}	0.240	m
	Height	H_{fcm}	4.5	H_{mcm}	0.300	m
	Cutting drum diameter	D_{fcm}	2.1	D_{mcm}	0.140	m
Scrubber	Exit diameter	D_{fs}	0.6	D_{ms}	0.040	m
	Exit velocity	V_{fs}	35	V_{ms}	2.333	m/s
	Volumetric flow rate	Q_{fs}	9.9	Q_{ms}	0.003	m^3/s
Jet fan	Exit diameter	D_{fj}	0.266	D_{mj}	0.010	m
	Outlet velocity	V_{fj}	46	V_{mj}	9.34	m/s
	Volumetric flow rate	Q_{fj}	2.5	Q_{mj}	0.00074	m^3/s
	Reach[16]	R_{fj}	26	R_{mj}	1.733	m
Jet fan position	Into the heading		1.2		0.08	m
	From side wall		1.0		0.067	m
	Above ground		0.7		0.047	m

2.3.1.2.1. Test Section and CM

The dimensions of the mine geometry and CM were scaled by a scale factor of 1 : 15. This means that there is a linear relationship between the actual mine and the scale model.

[14] Please take note that the actual width of most mines in South Africa is 7 m but 6.3 m in this research because the model by A.A. Daling was scaled from this dimension.

[15] The length of the scaled model represents a segment of 18 m.

[16] A reach is a jet penetration depth.

For example, the length of the heading is calculated as follows:

$$L_{fh} = 15 \times L_{mh}$$
$$35 = 15 \times L_{mh}$$
$$L_{mh} = 2.33 \text{ m}$$

2.3.1.2.2. Scrubber

The scrubber was scaled by percentage of volumetric flow method. To determine the flow of the scrubber in the scale model the percentage volumetric flow rate of the scale model is assumed to be the same as that of the full model. Scrubber fan diameter is scaled geometrically by a factor of 1:15. The scaling is as follows:

Full model volumetric flow rate,

$$Q_{fs} = 35 \times \frac{\pi}{4} \times 0.6^2$$
$$= 9.9 \text{ m}^3/\text{s}$$

Full model percentage volumetric flow rate,

$$P\% = \frac{Q_{fs}}{(L \times W \times H)_{fh}}$$
$$= \frac{9.9}{35 \times 6.3 \times 5}$$
$$= 0.009$$

The percentage of the scale model is thus 0.9%.

The volumetric flow rate of 15%-scale model is,

$$P\% = \frac{Q_{ms}}{(L \times W \times H)_{mh}}$$

$$Q_{ms} = 0.009 \times 2.333 \times 0.42 \times 0.333$$

$$Q_{ms} = 0.0029 \text{ m}^3/\text{s}$$

Scaling down the exit diameter for scrubber the result is 0.04m, therefore the exit velocity,

$$V_{ms} = \frac{Q_{ms}}{A_{ms}}$$

$$= \frac{0.0029 \times 4}{\pi \times 0.04^2}$$

$$= 2.3 \text{ m/s}$$

2.3.1.2.3. Through-road Air Velocity

Through-road is ventilated by the main ventilation system and flow is usually 2 m/s. There is generally no dust and mine gas concentration problems in the through-road since air flows are sufficient enough to dilute mine gas and dust. Though there is no current concern with through-road ventilation, it is brought into picture here because the air flowing in the through-road influences heading flow. Flow in the through-road is scaled by percentage of volumetric flow method as follows:

Volumetric flow rate in the actual mine,

$$Q_{ft} = 2 \times 6.3 \times 5$$

$$= 63 \text{ m}^3/\text{s}$$

Full model percentage volumetric flow rate,

$$P\% = \frac{Q_{ft}}{(L \times W \times H)_{ft}}$$

$$= \frac{63}{(18 \times 6.3 \times 5)}$$

$$= 0.111$$

The percentage of the scale model is thus 11.11%.

The through-road volumetric flow rate for the 15%-scale model is,

$$P\% = \frac{Q_{mt}}{(L \times W \times H)_{mt}}$$

$$Q_{mt} = 0.019 \text{ m}^3/\text{s}$$

Therefore, the scale model air velocity in the through-road is,

$$V_{mt} = 0.0665 \text{ m/s}$$

2.3.1.2.4. Jet Fan

For the jet fan scaling, it is important to take into consideration the fan penetration in order to arrive at accurate values. In the actual mine which is used as reference for the scale model, the jet fan with an exit velocity of 45 m/s only penetrates approximately 26 m into the blind heading [25].

As it has already been explained in 2.4.1, the jet fan in the scaled model was replaced by a nozzle with exit diameter of 10 mm[17], blowing out air from air compression system. The jet fan properties for the scale model were calculated and are shown in table 2.1. The standard and scaled down positions of the fan are also indicated in the same table. The width of test section is half the total distance because it is assumed that the air will need equal cross section areas into and out of the heading.

Full model volumetric flow rate for the jet fan,

$$Q_{fj} = 45 \times \frac{\pi}{4} \times 0.266^2$$
$$= 2.5 \text{ m}^3/\text{s}$$

Full model percentage volumetric flow rate,

$$P\% = \frac{2.5}{(35 \times 3.15 \times 5)}$$
$$= 0.0041$$

The percentage of the scale model is thus 0.41%.

The volumetric flow rate of 15%-scale model is,

$$Q_{mj} = 0.0041 \times 2.333 \times .21 \times .333$$
$$= 0.0007 \text{ m}^3/\text{s}$$

Therefore, exit air velocity for the 10 mm nozzle is,

[17] It should be noticed that this figure is not found by geometrical scaling but it was found by comparing jet penetrations of different exit diameters[25].

V_{mj} = 9.0 m/s

2.3.1.3. Flow Visualization

As air is transparent and cannot be seen with human eyes, a smoke producing device and a system to conduct the smoke into the test section[18] of the model was designed. This system facilitates the visualisation of air flow. Figure 2.3, shows a schematic representation of the smoke producing device. It comprises a container with a heating element inside it, a glycol/water mixture[19] reservoir with a submersible pump in side it, a network of tubes and a fan that blows smoke into the test section.

[18] The mined spaced in the heading including through-road is the test section.

[19] Glycol/water mixture has commercial names called fog fluid, fog juice or smoke water. It commonly used by Disk Jockeys to create a foggy environment at discos or parties. One can easily get this fluid in music equipment shops in RSA.

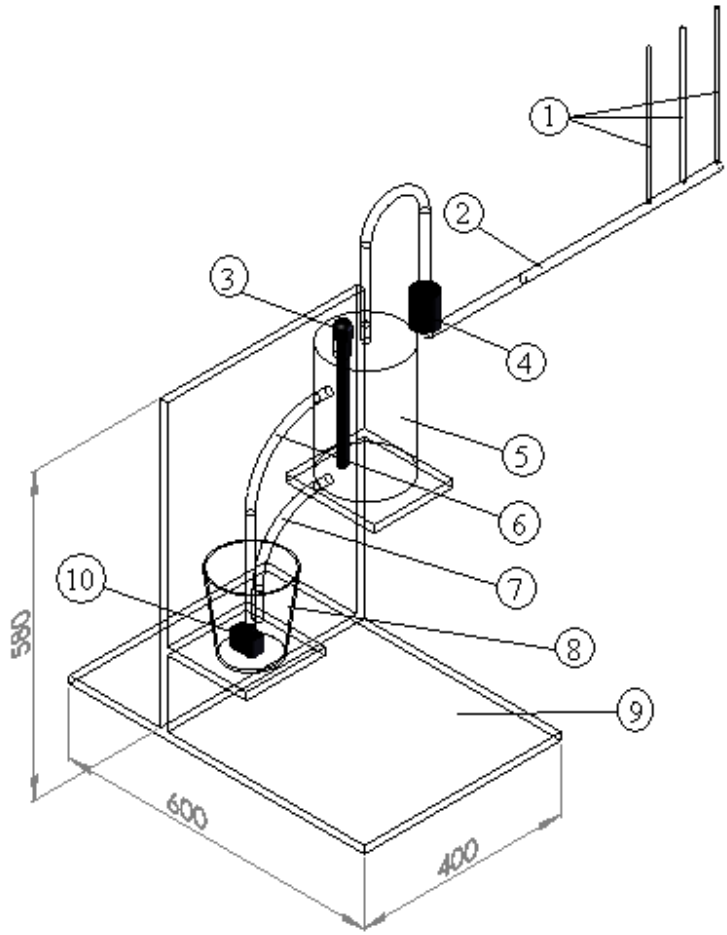

No	Description	No	Description
1	Tubes delivering smoke into heading	6	Glycol/water mixture return tube
2	Main smoke tube	7	Glycol/water mixture return tube
3	Heating Element	8	Glycol/water mixture reservoir
4	Smoke extractor	9	Stand
5	Smoke container	10	Pump

Figure 2.3: Smoke System using a pump to spray fluid onto the heating element

The smoke system works as follows: glycol/water mixture is pumped from the tank into the container where it is sprayed onto the hot heating element. The burning of the fluid produces smoke. The smoke is blown into the test section by the fan and the liquid glycol/water mixture returns to the circulation process. The smoke enters the test section through the tubes inserted in the holes on the heading floor of the model as indicated in figure 2.4.

Initially, the heating element in use was a modified domestic aquarium heater with a rating of 75W. In the course of performing experiments, the pump broke down due to high temperature of the fluid. As a result the heater burnt out. The heater was then replaced by a coiled heating element with a rating of 1000W because a replacement that could fit the pot design was not readily found.

All the walls inside the scale model, excluding the transparent observation panels, were painted black (using non-gloss paint) to enhance visibility of smoke when capturing video images.

2.3.1.4. Rehabilitation Work on the Model

Despite the scale model being available for the required experiments, it was found that it was not in working condition. The following, had to be done to ensure that the model was back in good working condition:

- Non metallic parts of the smoke producing container were burnt and damaged in the previous tests therefore the whole container was replaced by all metal (galvanised iron sheet) container. And some ports for tube attachment were included in the design. Other changes that were made in the course of experiments are explained in chapter 4.

- Initially, the smoke extractor used for forcing smoke into the test section was at the top of the smoke producing container. Due to high temperature the plastic parts got damaged. To solve this problem, the smoke extractor was relocated along the smoke delivery tube, as shown in figure 2.3.

- The joints were sealed with silicon sealant to make the test section air tight.

- The blades of the fan for smoke extractor were replaced by a smaller one to ensure that the smoke enters the test section at a very low velocity. This was an improvement on the model because smoke entering test section at high velocity compromises the flow pattern created by the jet fan.

- The tapered end of the through-road was found open, as a result there was almost no air flowing in the through-road when the fan was switched on. The tapered end was covered by plastic sheet to ensure air flow.

- Since the air compression system can be used by several persons at the same time, the flow fluctuated. A pressure regulator[20] was fixed to ensure constant supply pressure. Although, the regulator was not small enough to show the readings accurately, it was able to regulate a constant pressure. The flow velocity was set by using anemometer.

- A light source was fixed to assist in capturing clear video pictures.

[20] It was the smallest regulator that was found at that time.

2.3.2. Steady State Condition

The steady state simulations were done in order to investigate the air flow patterns in the underground coalmine.

To facilitate steady state experiment holes with diameter of 6 mm were drilled through floor of the heading as shown in figure 2.4. Taking the length, height and width of the scale model as x, y and z direction, the spacing of holes on the model in x-direction was 322 mm and that in z-direction 67 mm, representing 4.83 m and 1 m in full scale scenario respectively. Since some points above the CM were also examined for air flow, the holes were drilled on the CM as well. Initially, there were a total of 42 holes made on the floor starting from column C to I. But after the first type of the experiment was done and analysed it was observed that more points were required around the heading entrance hence two more columns (columns A and B) were added.

For the purposes of analysis of experimental data, later on in the chapter, each hole was given a reference number. For example, the hole at top left corner is A6.

Please take note that there is no hole at location A1. This is so because the pipe carrying from the compressor to the nozzle passed over this position and it was not possible to have a smoke out at the location. However, this does not affect the investigation much.

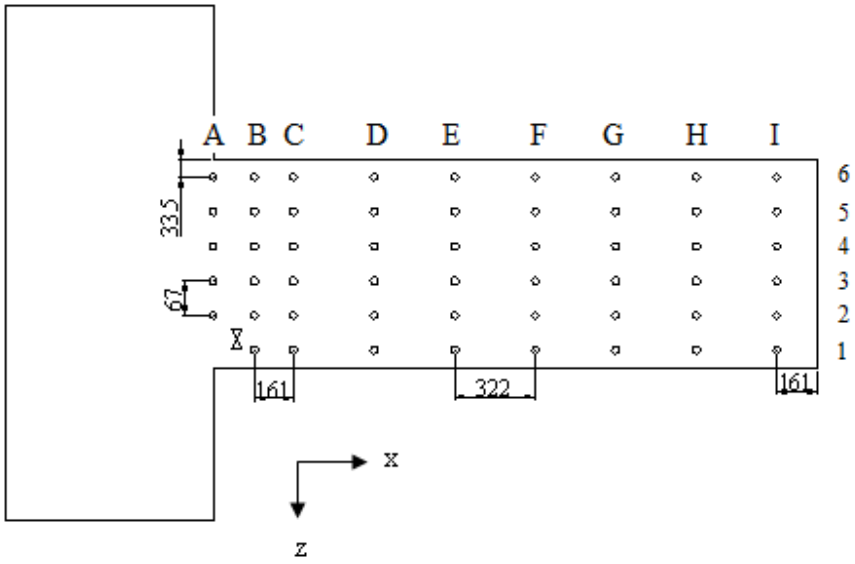

Figure 2.4: Holes on the floor of the heading

2.3.2.1. Mining Geometries

Three different points of mining progression in the heading were selected. See the plan views of mine geometries in figure 2.5. A single geometry could be enough but three were deliberately done in order to increase the confidence in the results of the research. The first one (A), at a point when the first and second box cuts[21] are completed, in other words half the heading has been mined. Secondly (B), at a point where the CM is doing the third box cut with coal seam 10 m long (equivalent to 666 mm in the scale model) remaining. And finally (C), at a point where CM is doing the last box cut with coal seam 7 m long (equivalent to 467 mm in the scaled model) remaining. These three points, figure 2.5, are referred to as MG-1, MG-2 and MG-3, respectively. MG stands for Mine Geometry.

[21] Box cuts are described under bord and pillar mining techniques.

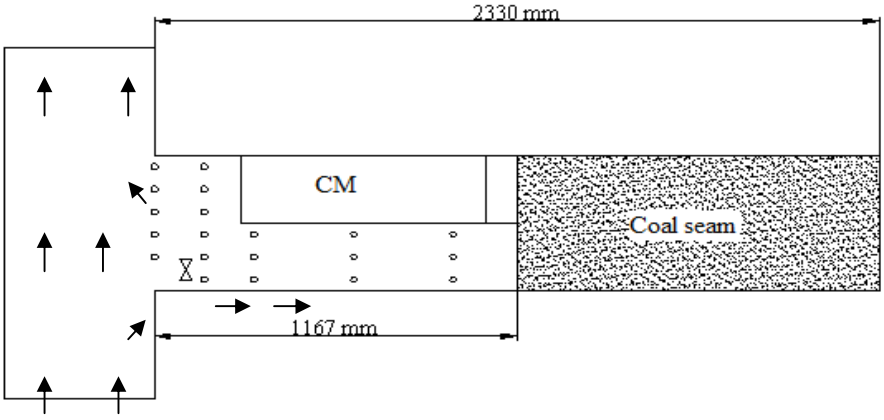

(A) MG-1

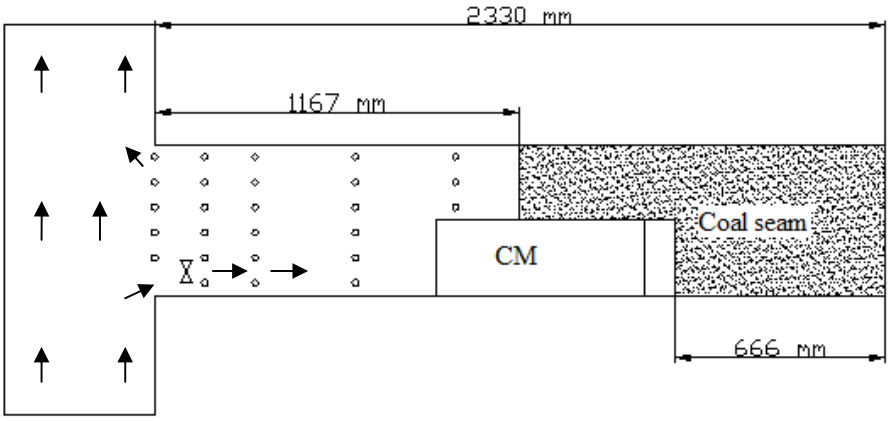

(B) MG-2

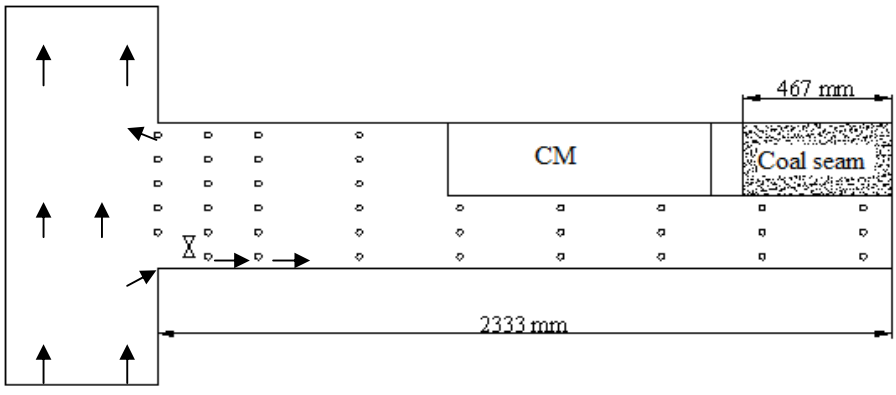

(C) MG-3

Figure 2.5: Mine Geometries Shown in plan view Used in the Steady State Scaled Experiments (from the top MG-1, MG-2 and MG-3).

In all the three scale mine geometries the jet fan position is the same, i.e. 80 mm into the heading, 67 mm from the sidewall and 47 mm above the floor. This scaled position represents the actual position used in most mines in RSA.

More details on conduction of steady state experiment are in chapter 4.

2.3.3. Unsteady State

The objective of this experiment was to find out the time taken to extract the air out of the test section. To achieve this objective smoke was also utilize as in steady state experiments. Unlike the steady state experiment where smoke was used to assist in visualizing the air movement, in this instance smoke was used to represent air in the actual mine that is polluted with dust and mine gas. Smoke was selected to represent pollutants because its presents could be detected by sensors. Fresh air was then let into the test section to clear out the polluted air. Time taken for the smoke to completely be removed at different locations was recorded. The locations of sensors are described in the next section but details of the sensors and conduction of unsteady state experiment are described in chapter 4.

2.3.3.1. Sensor Locations

Sensors were inserted in the scaled-down mine model at several location of interest as shown in figure 2.5. CAD geometry representing the set up in figure 2.5 was also prepared for the purposes of simulation and comparison with experimental results.

The numerical positions for the sensors are given in table 2.1. The origin of these positions is at right[22] bottom corner of the heading entrance of mine geometry as indicated in figures 2.6. These dimensions are read to the centre of the sensors.

[22] Right hand side of a person standing at heading entrance and facing the blind end of heading.

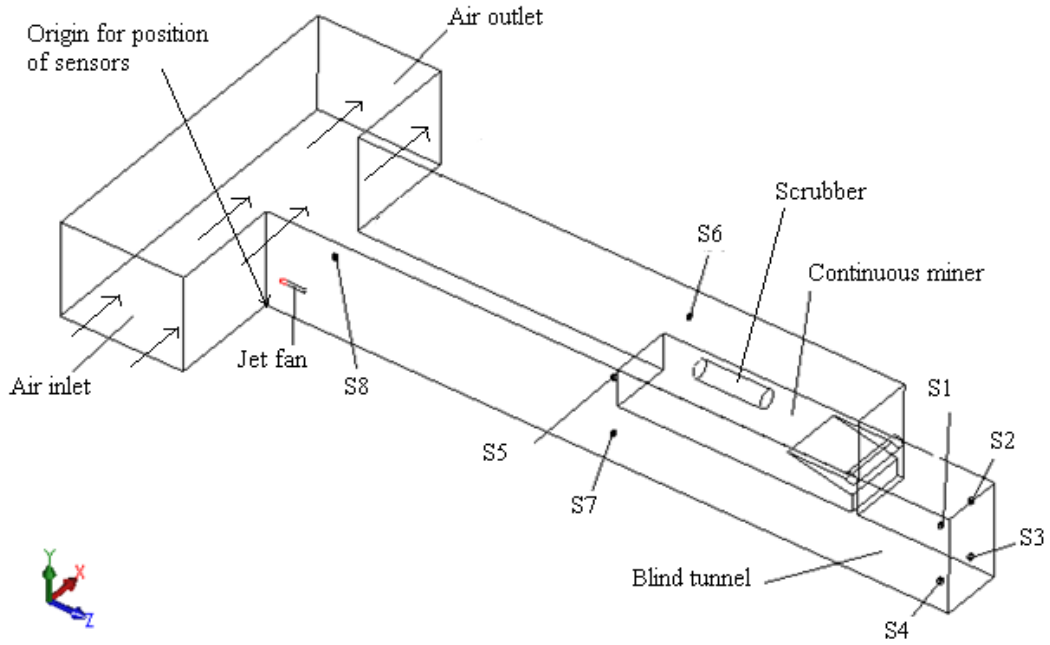

Figure 2.6: MG 3 in Isometric View Showing Smoke Sensors

Table 2.2: Numerical Location of Sensors in the Test Section

Sensor	Position in millimetres		
	X	Y	Z
S1	2280	282	36
S2	2280	282	174
S3	2280	70	174
S4	2280	70	36
S5	1167	282	36
S6	1167	282	384
S7	1167	70	36
S8	150	210	166

Sensors S1, S2, S3 and S4 were located at the blind end since this is the most problematic area as far as mine ventilation is concerned. Sensors S5, S6 and S7 were located midway the heading while S8 was located at the heading entrance. This was deliberately done to ensure that almost all the heading space was covered.

CHAPTER 3: CFD MODEL AND CFD RESULTS

3.1 Introduction

As it has already been mentioned in previous chapter, CFD modelling was used in this investigation. The importance of correct CFD model is immeasurable, as an incorrect model or non repeatable solution will render the optimization process useless.

In this study the CFD software, Star CCM+ version 3.02.006 was used. Due to the fact that the software was used for the first time by the researcher and to ensure the correctness of the model; a few simple internal fluid flow problems were done using both analytical and computer simulation methods and then the results were compared. This was done for the purposes of building confidence in the use of the Star CCM+ software before tackling the actual research problem.

The first section of this chapter gives basic concepts of internal fluid flow. Then the theoretical and simulated pressure change solutions of fluid flow in selected closed conduit[23] were compared as follows: flows in constant diameter pipe and rectangular duct, duct with 90 ^{0} mitre bend (without vanes), pipe and duct with long sweep elbow and pipe with an orifice. The analytical solutions were solved using Microsoft excel. The last section in this chapter presents CFD models of scaled down model of the underground coalmine.

3.2. CFD Modeling of Selected Internal Fluid Flows

In order to understand how the solutions to fluid flows in the closed conduits were arrived at, some of the basic concepts of fluid flow are discussed first.

[23] Both pipes and ducts are referred to as conduits.

3.2.1 Basic Concepts of Fluid Flow in Conduits

3.2.1.1. Laminar or Turbulent Flow

The flow of a fluid in a conduit may be laminar flow or it may be turbulent flow. In a laminar flow the fluid flows with no significant mixing of neighbouring fluid particles. If a dye were injected into the flow, it would not mix with the neighbouring fluid except by molecular activity; it would retain its identity for a relatively long period of time. Viscous shear stress always influences a laminar flow.

In a turbulent flow fluid motions vary irregularly so that quantities such as velocity and pressure show a random variation with time and space coordinates. The physical quantities are often described by statistical averages. A dye injected into a turbulent flow would mix immediately by the action of the random moving fluid particles; it would quickly lose its identity in this diffusion process [21-22].

The flow regime depends on three physical parameters describing the flow conditions. The first is the length scale of the flow field, such as the diameter of the pipe. If this length is sufficiently large, a flow disturbance may increase and the flow may be turbulent. The second parameter is a velocity scale; for a large enough velocity the flow may be turbulent. The third parameter is the kinematic viscosity; for a low enough viscosity the flow may be turbulent.

The three parameters can be combined into a single parameter that can serve as a tool to predict the flow regime. This quantity is called Reynolds number[24], a dimensionless parameter, defined as

[24] It is named after Osborne Reynolds (1842 – 1912) who did a lot of work in this area.

$$\text{Re} = \frac{\rho V D}{\mu} \tag{3.1}$$

Where D and V are a characteristic length and average velocity, respectively; for example in a pipe flow D could be diameter of the pipe and V the average velocity of the fluid. ρ is density and μ is viscosity[25] due to linear deformation. Since the viscosity is often divided by the density in the derivation of equations, it has become useful and customary to define kinematic viscosity represented by symbol υ.

$$\upsilon = \frac{\mu}{\rho} \tag{3.2}$$

So that Reynolds number can be expressed in terms of kinetic viscosity as

$$\text{Re} = \frac{VD}{\nu} \tag{3.3}$$

The flow can also be intermittently laminar and turbulent. This phenomenon occurs during the transition from laminar to turbulent when the Reynolds number is close to critical Reynolds number, Re_{crit}. For conduit flow the value of Reynolds number must be less than approximately 2100 for laminar flow and greater than approximately 4000 for turbulent flow [22].

Both laminar and turbulent flows can either be steady[26] or unsteady[27].

[25] Viscosity can be thought of as the internal stickiness of a fluid [21].

[26] Steady flow: flow in which physical quantities do not change with time.

[27] Unsteady flow: time dependent flow where physical quantities change with time.

3.2.1.2. Pressure

Fully developed steady flow in a constant diameter pipe may be driven by gravity and/or pressure forces. For horizontal pipe flow, gravity has no effect except for a hydrostatic pressure variation across the pipe that is usually negligible. It is the pressure difference, $\Delta p = p_1 - p_2$, between one section of the horizontal pipe and another which forces the fluid through the pipe. Viscous effects provide the restraining force that exactly balances the pressure force, thereby allowing the fluid to flow through the pipe with no acceleration.

The need for pressure drop can be explained using two different points of views. In terms of a force balance, the pressure force is needed to overcome the viscous forces generated. In terms of an energy balance, the work done by the pressure force is needed to overcome the viscous dissipation of energy throughout the fluid [21-23].

3.2.1.3. Incompressible and Compressible Flows

Fluid flow is also classified into incompressible and compressible flows. An incompressible flow exists if the density of each fluid particle remains relatively constant as it moves through the flow field, that is,

$$\frac{D\rho}{Dt} = 0 \qquad (3.4)$$

Among other fluids, low-speed gas flows, such as the atmospheric flow are also considered to be incompressible flows. The Mach number[28], M is useful in deciding

[28] The Mach number, named after Ernest Mach (1838 – 1916), is defined as $M = \frac{V}{c}$ where V is the gas speed and the wave speed $c = \sqrt{kRT}$ [21].

whether a particular gas flow can be studied as an incompressible or compressible flow. If M < 0.3, density variations are at most 3% and the flow is assumed to be incompressible; for standard air this corresponds to a velocity below about 100 m/s. If M > 0.3, the density variations influence the flow and compressibility effects should be accounted for [21].

3.2.1.4. Loses in Developed Conduit Flow

Head loss is probably the most calculated quantity in conduit flow. If the head loss, expressed in metres, is known in a developed flow, the pressure change can be calculated. The head loss that results from the wall shear in a developed flow is related to the friction factor by the Darcy-Weisbach equation, namely,

$$h_L = f\frac{L}{D}\frac{V^2}{2g} \quad (3.5)$$

Where, f = friction factor[29]

L = length of conduit in metres

D = diameter of pipe in metres

V = average velocity of fluid m/s

g = acceleration due to gravity m/s^2

If the friction factor is known, the head loss and the pressure change can be found. In equation 3.5, it can be observed that the head loss is directly proportional to the average velocity of the fluid.

[29] Friction factor is a dimensionless wall shear defined by $f = \frac{8\tau}{\rho V\text{^}2}$

The friction factor f depends on the various quantities that affect the flow, written as

$$f = f(\rho, \mu, V, D, e) \quad (3.6)$$

Where in addition to the variables defined in equation 3.1,

e = average wall roughness height in mm

A dimensional analysis of equation 3.6 gives the following dimensionless quantities

$$f = f\left(\frac{\rho VD}{\mu}, \frac{e}{D}\right) \quad (3.7)$$

Where, $\frac{e}{D}$ is the relative roughness.

and $\frac{\rho VD}{\mu}$ is Reynolds number.

For, non circular cross sections, good approximations can be made for the head loss by using the hydraulic radius R, defined by:

$$R = \frac{A}{P} \quad (3.8)$$

Where A is the cross sectional area [m^2] and P is the wetted perimeter [m], that perimeter where the fluid is in contact with the wall of the conduit. Therefore, the Reynolds number, the relative roughness and the head loss for non circular conduits are as follows:

$$Re = \frac{4\rho VR}{\mu} \quad \text{or} \quad \frac{4VR}{\nu} \quad (3.9)$$

$$\text{Relative roughness} = \frac{e}{4R} \tag{3.10}$$

$$h_L = f\frac{L}{4R}\frac{V^2}{2g} \tag{3.11}$$

Experimental data that relate the friction factor to the Reynolds number have been obtained for fully developed pipe flow over a wide range of wall roughness. The results of these data are presented in Appendix C, which is commonly referred to as the Moody diagram[30]

3.2.1.5. Minor Loses in Conduit Flow

Apart from head losses due to a developed flow in a conduit there are also additional losses that are referred to as minor losses, even though such losses can exceed the frictional losses. These losses are due to fittings and other conduit geometries which include: valves, elbows, enlargements, contractions, orifice, inlets, outlets, bends etc. Each of these devices causes a change in the magnitude and/or the direction of the velocity vectors and hence results in head loss. In general, if the flow is gradually accelerated by a device, the losses are very small; relatively large losses are associated with sudden enlargement or contractions because of the separated[31] regions that result.

A minor loss is expressed in terms of a loss coefficient K, defined by

$$h_L = K\frac{V^2}{2g} \tag{3.12}$$

[30] Named after Lewis F. Moody (1880 – 1953) [21]

[31] A separated flow occurs when the primary flow separates from the wall.

Values of *K* have been determined experimentally for the various fittings and geometry changes of interest in piping systems. One exception is the conical enlargement and contraction from diameter D_1 to diameter D_2, for which the value of *K* can be calculated. Since an orifice is a combination of contraction and enlargement it can also found by their summation. The formulae for the three exceptions are as follows:

For conical enlargement

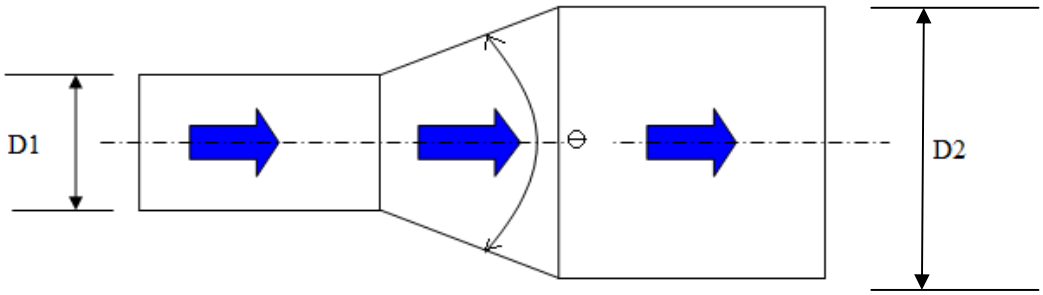

Figure 3.1: Conical Enlargement [22]

$$\text{If } \theta \leq 45^0, \qquad K_e = \frac{2.6\sin\theta/2\left[1-\left(D1/D2\right)^2\right]^2}{\left(D1/D2\right)^4} \tag{3.13}$$

$$\text{If } 45^0 < \theta \leq 180^0 \qquad K_e = \frac{\left[1-\left(D1/D2\right)^2\right]^2\sqrt{\sin\theta/2}}{\left(D1/D4\right)^4} \tag{3.14}$$

Therefore, for sudden enlargement $\theta = 180^0$

And $$K_e = \frac{\left[1-\left(D1/D2\right)^2\right]^2}{\left(D1/D2\right)^4} \quad (3.15)$$

For conical contraction

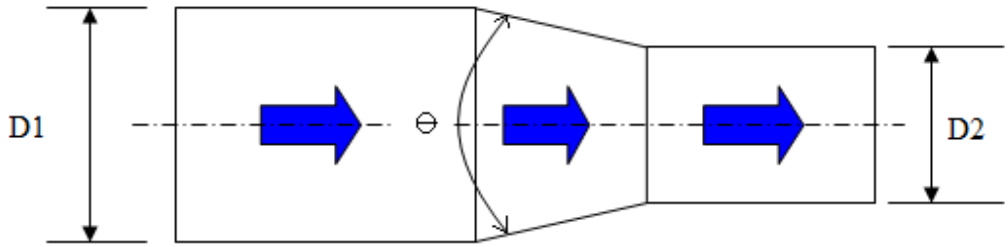

Figure 3.2: Conical Contraction [22]

If $\theta \leq 45^0$, $$K_c = \frac{0.8\sin\theta/2\left[1-\left(D2/D1\right)^2\right]}{\left(D2/D1\right)^4} \quad (3.16)$$

If $45^0 < \theta \leq 180^0$ $$K_c = \frac{0.5\left[1-\left(D2/D1\right)^2\right]\sqrt{\sin\theta/2}}{\left(D2/D1\right)^4} \quad (3.17)$$

Therefore, for sudden contraction $\theta = 180^0$

And $$K_c = \frac{0.5\left[1-\left(D2/D1\right)^2\right]}{\left(D2/D1\right)^4} \quad (3.18)$$

For an orifice

Orifice is the combination of sudden contraction and enlargement, therefore its loss coefficient K_c, is the sum of the two losses.

$$K_o = K_c + K_e$$

$$= \frac{0.5\left(1-\frac{D1}{D2}\right)^2 + \left(1-\left(\frac{D1^2}{D2}\right)\right)^2}{\left(D_1/D_2\right)^4} \qquad (3.19)$$

A bend has a relatively large loss coefficient. This results primarily from the secondary flow caused by the fluid flowing from high-pressure region to the low-pressure region. In addition, a separate region occurs at the sharp corner. Energy is required to maintain a secondary flow and the flow in the separate region. This wasted energy is measured in terms of the loss coefficient.

The loss coefficients for various geometries are presented in Table 3.1

Table 3.1: Nominal Loss Coefficients *K* (Turbulent Flow)[32] [21]

Type of fitting	*Screwed*			*Flanged*		
Diameter	2.5 cm	5 in	10 cm	5 cm	10 cm	20 cm
Globe valve (fully open)	8.2	6.9	5.7	8.5	6.0	5.8
(half open)	20	17	14	21	15	14
(one-quarter open)	57	48	40	60	42	41
Angle valve (fully open)	4.7	2.0	1.0	2.4	2.0	2.0
Swing check valve (fully open)	2.9	2.1	2.0	2.0	2.0	2.0
Gate valve (fully open)	0.24	0.16	0.11	0.35	0.16	0.07
Return bend	1.5	0.95	0.64	0.35	0.30	0.25
Tee (branch)	1.8	1.4	1.1	0.80	0.64	0.58
Tee (line)	0.9	0.9	0.64	0.39	0.30	0.26
Standard elbow	1.5	0.95	0.23	0.30	0.19	0.15
Long sweep elbow	0.72	0.41	0.23	0.30	0.19	0.15
45^0 elbow	0.32	0.30	0.29			
Square-edged entrance	0.5					
Re-entrant entrance	0.8					
Well-rounded entrance	0.03					
Pipe exit	1.0					
Sudden contraction[33]	Area ratio					
	2:1		0.25			
	5:1		0.41			
	10:1		0.46			
Orifice	Area ratio A/A_o					
	1.5:1		0.85			
	2:1		3.4			
	4:1		29.0			
	≥6:1		$2.78(A/A_o-0.6)^2$			
Sudden enlargement[34]	$(1 - A_1/A_2)^2$					
90^0 mitre bend (without vanes)	1.1					
(with vanes)	0.2					
General contraction						
(30^0 included angle)	0.02					
(70^0 included angle)	0.07					

[32] Values for other geometries can be found in *Technical Paper 410*, Crane Company, 1957.

[33] This is based on exit velocity V_2.

[34] This is based on entrance velocity V_1.

3.2.2 Pressure Loss Calculation and Simulation

Pressure change can be found either by theoretical calculation, conducting experiment or computer simulations. Experimental method produces the most reliable results but at the same time it is costly, in terms of finance and time, to conduct them. For this reason, the author decided to compare the computer simulated pressure change in conduits of different geometries to the theoretical results.

Before presenting the pressure changes for selected geometries description of steps that were followed when calculating and simulating pressure change in a conduit are presented.

3.2.2.1. Steps in Theoretical Calculation

- Calculate the Reynolds number. Re is found using equation (3.1) if the conduit is a pipe or equation (3.8) if a conduit is a duct. To use any of the two equations one needs to know the cross section dimensions of the conduit, the velocity of the fluid flowing in the conduit. The density, viscosity or kinematic viscosity can be extracted from the table of fluid properties if the temperature of the fluid is known. The properties of water and air required in this research are attached in Appendix D.

- Determine if the flow is laminar or turbulent.

- Afer Re of the flow and relative roughness of the conduit surface are calculated.

- Calculate the fluid head resistance to overcome the flow through the conduit. Equations 3.5 or 3.11 are used if the conduit is a pipe or a duct respectively.

- Determine loss coefficient K, for the fitting(s) within the conduit. The nominal loss coefficients for common commercial fittings are shown in table 3.1 and formula for pipe enlargement; contraction and orifice are given in equations 3.13 to 3.19.

- Calculate the total head resistance or loss that is present in the conduit.

- Calculate the pressure loss in the conduit. This is found by applying the following formulae:

$$\Delta P = \rho g h = \gamma h \qquad (3.20)$$

Where ΔP = pressure loss or change [Pa]

$\gamma = \rho g$ = specific weight [N/m^3]

h = height [m]

3.2.2.2. Steps in Computer Simulation Using Star CCM+

Before one starts simulation process in Star CCM+, the geometry in/on which the flow will be simulated must be done first. This can be achieved using drawing and design software like Solid Works, Auto CAD, etc. The geometries are then saved in file types that star CCM+ can import from. These files are [20]:

- `.dbs` - pro-STAR surface database mesh file.
- `.inp` - pro-STAR cell/vertex shell input file.
- `.nas` - NASTRAN shell file.
- `.pat` - PATRAN shell file.
- `.stl` - Stereo lithography file.
- `.igs/.iges` - Initial Graphics Exchange Specification file.
- `.stp/.step` - Standardized Exchange of Product file.

- `.x_t/.x_b` - Para solid Transmit file

In this investigation geometries were created in Solid Works then saved in a Stereo lithography file.

After the necessary geometry is created the simulation process in Star CCM+ proceeds as follows [20]:

- Import geometry from the relevant file.
- Set boundaries and regions[35].
- Mesh the geometry[36]. This only applies in situation where the geometry was not meshed prior to importation. Mesh model has to be chosen before the generation is initiated. In this research, geometries were imported coarsely meshed and had to be surface re-meshed before volume meshing was generated.
- Define the physical models in the continua.
- Define the region conditions, values and boundary conditions.
- Set up reports/monitors.
- Run the simulation. Convergence can be monitored while the simulation is running and if necessary solver parameters can adjusted.
- Post-process the results. This includes making plot and their analysis among other things.

3.2.3. Flows in Selected Conduits

This section presents the comparative results for pressure changes in different conduits found through analytical and simulation methods. All the conduits under consideration

[35] A region is a volume domain (or surface in a two-dimensional case) in space and has to be completely surrounded by boundaries.

[36] Meshed geometries prepared in pro-star, gridgen, fluent, gambit, star-CD, ICEM are compatible with Star CCM+ [20].

are assumed to be made of smooth surfaces[37] and are lying in a horizontal position. Both the analytical and numerical pressure changes are plotted on the same graph for ease of comparison. An analytical calculation for a pipe with an orifice only is shown in Appendix E as an example.

3.2.3.1. Constant Diameter Pipe

Water flow in a constant diameter straight pipe with the following details was simulated and then pressure drop was analytically done:

Internal diameter	0.03 m
Length	0.50 m
Water velocity	2.83 m^3/s

The pressure change for both simulation and analytical calculation are shown in the graph in figure 3.3.

[37] The friction factors are taken from the line indicated as smooth pipe in Moody Diagram on appendix C.

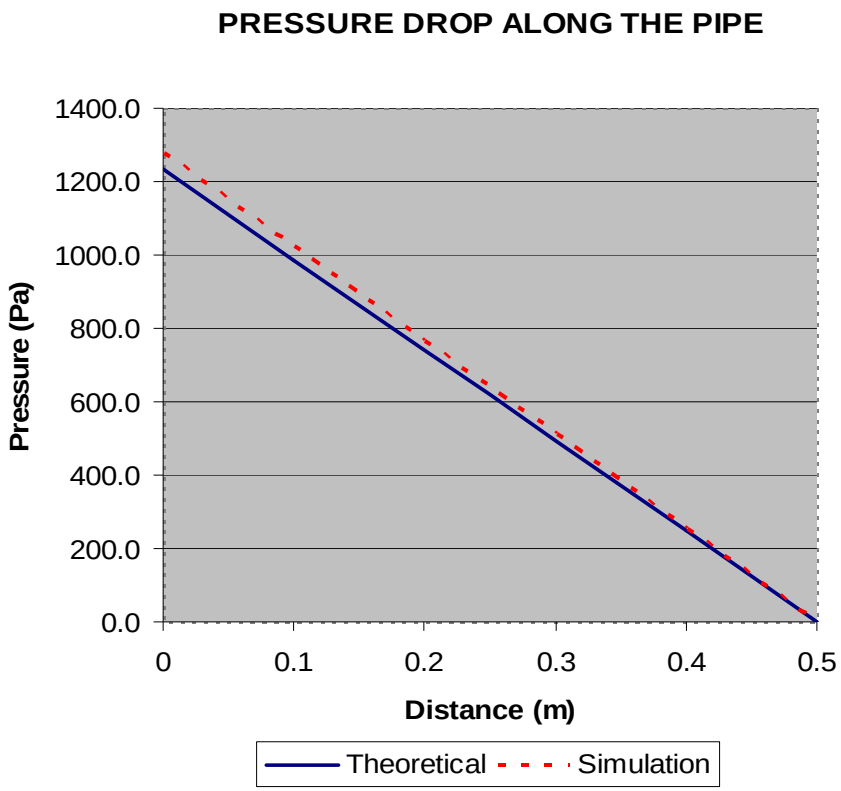

Figure 3.3: Pressure Change in a Constant Diameter Pipe by Simulation and Analytical Calculation

The two plots for theoretical and simulated pressure drop are almost the same. The small difference, approximately 50 Pa which, translates to 4% difference, may be due inaccurate reading from Moody diagram.

3.2.3.2. Rectangular Duct

Water flow in a square straight duct with the following details was simulated and then pressure change was analytically done:

Internal cross section 0.05 m square

Length	1.00 m
Inlet velocity	1.00 m/s

The pressure change for both simulation and analytical calculation are shown in the graph in figure 3.4.

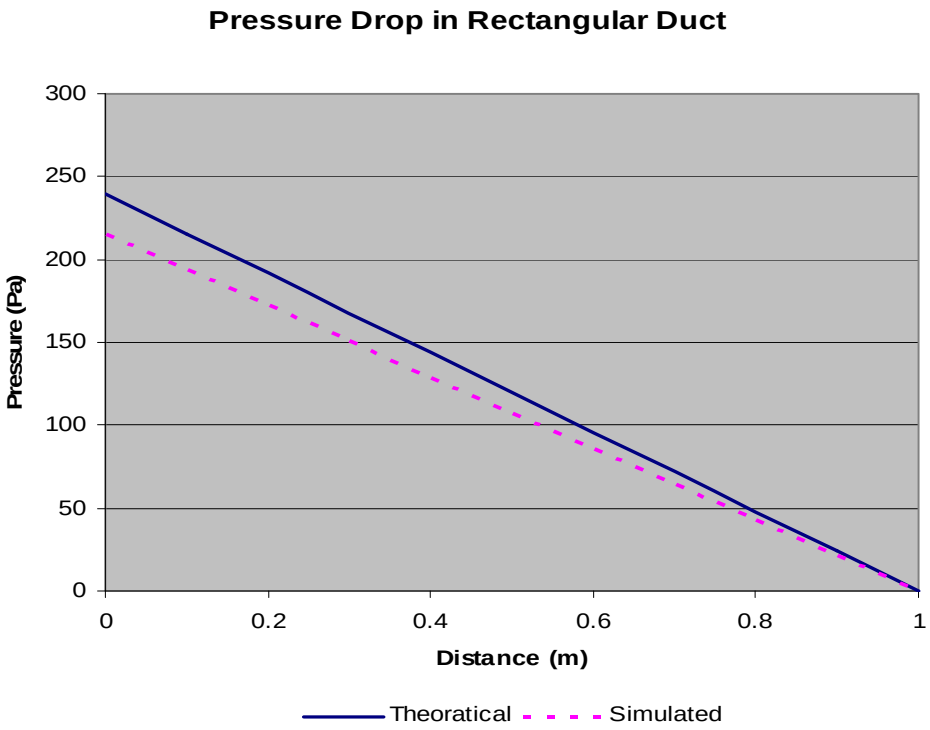

Figure 3.4: Pressure Change in Square Duct by Simulation and Analytical Calculation

Just like in the constant diameter pipe simulation two plots for theoretical and simulated pressure drop in the straight duct are also almost the same with a difference of about 10%. The difference may arise from inaccurate reading from Moody diagram.

3.2.3.3. Duct with 90° Miter Bend (without vanes)

Water flow in a rectangular duct with 90° mitre bend, figure 3.5, having the following details was simulated and then pressure change was analytically done:

Internal cross section	0.10 m wide by 0.05 m high
Length	2.00 m
Inlet velocity	1.00 m/s
Loss coefficient *K* (table 3.1)	1.1

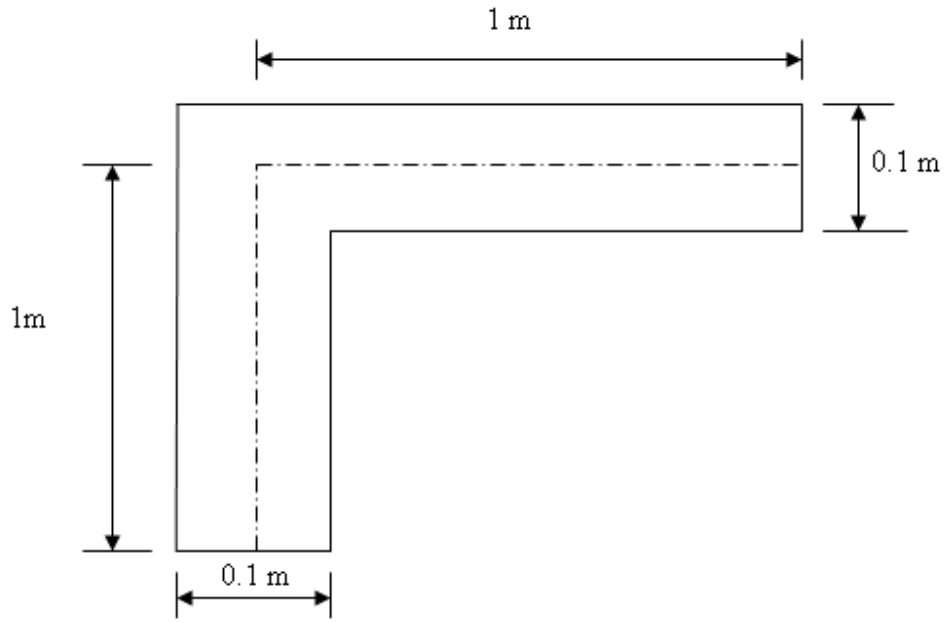

Figure 3.5: Rectangular duct with 90° bend without vanes

The pressure change for both simulation and analytical calculation are shown in the graph in figure 3.6.

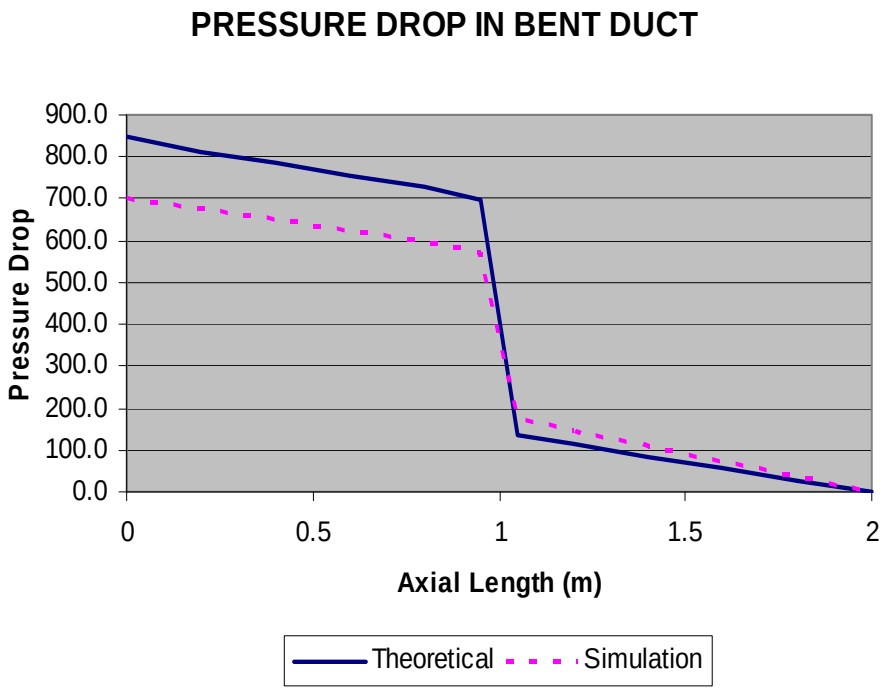

Figure 3.6: Pressure Change in a rectangular duct with 90 ^{0} mitre bend by Simulation and Analytical Calculation

The pressure drops from the two results have a difference of approximately 150 Pa but the profiles of the two plots are similar. The main reason for the difference in plot profiles could be the position where the minor head loss occurs. Theory assumes that it occurs right at the bend while in real practice it occurs after the bend.

3.2.3.4. Pipe with Long Sweep Elbow

Water flow in a pipe with long sweep elbow, figure 3.7, having the following details was simulated and then pressure change was analytically done:

Internal diameter 0.10 m

Length	1.50 m
Inlet velocity	2.00 m/s

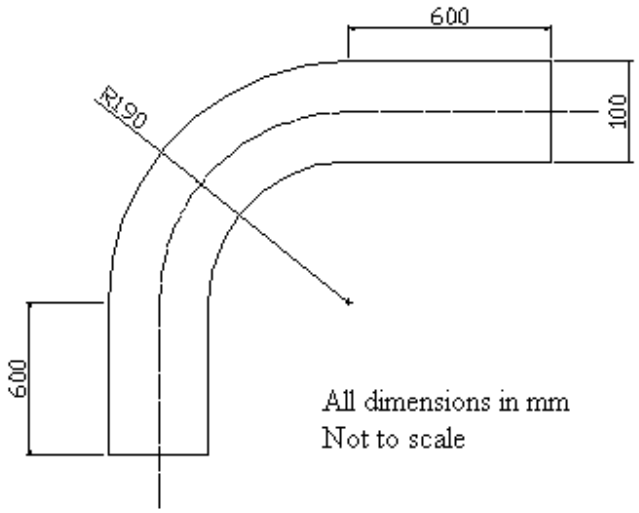

Figure 3.7: Long sweep elbow with straight pipe on both ends

The pressure change for both simulation and analytical calculation are shown in the graph in figure 3.8.

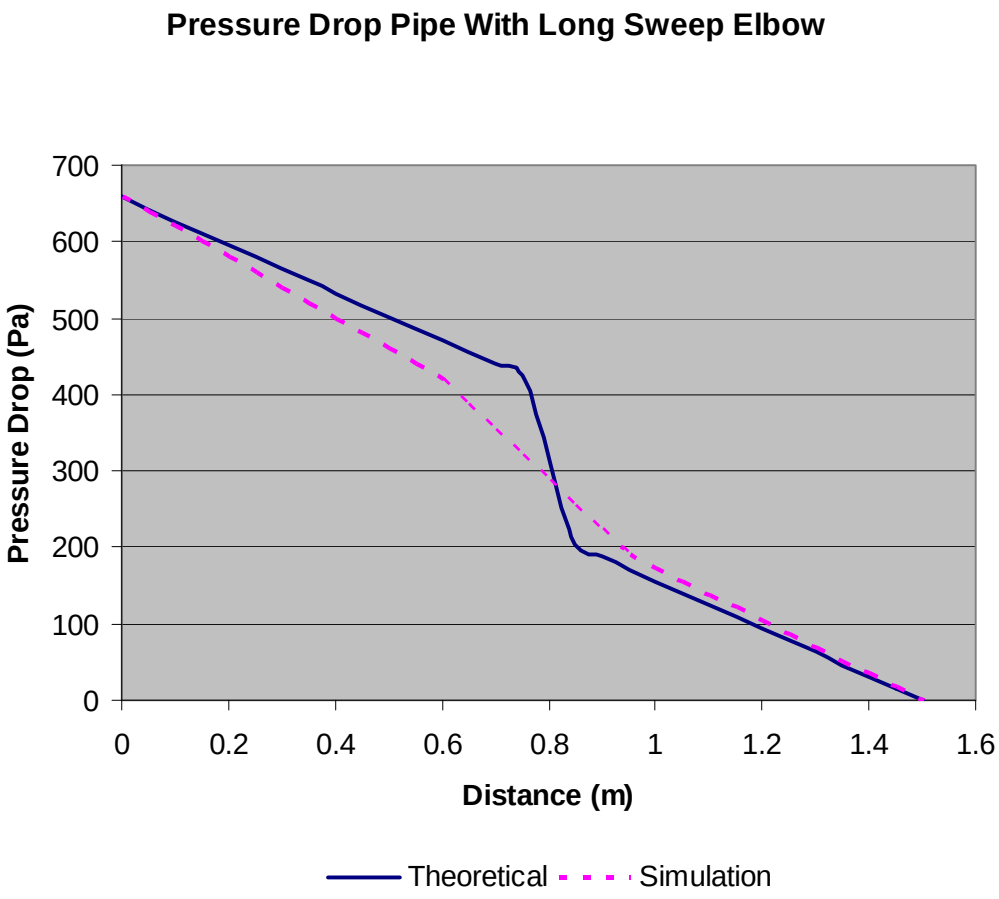

Figure 3.8: Pressure Change in a pipe with long sweep elbow by Simulation and Analytical Calculation

The pressure change found by the two methods is almost the same. The only difference is the gradient which might have been caused by point where the minor loss is assumed to occur in the theoretical calculation.

3.2.3.5. Orifice

Water flow in a pipe with an orifice, figure 3.9, having the following details was simulated and then pressure change was analytically done:

Internal diameter	0.100 m
Orifice diameter	0.071 m
Length	2.000 m
Inlet velocity	1.000 m/s

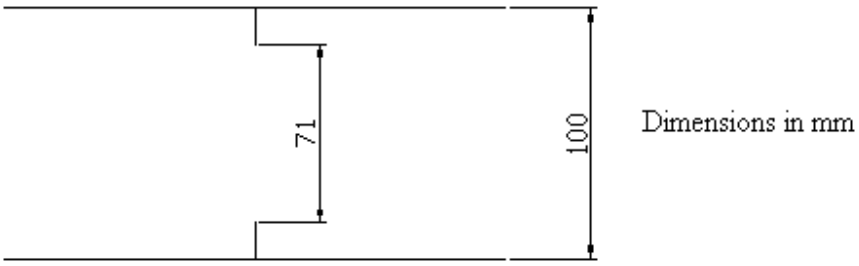

Figure 3.9: Orifice

The pressure change for both simulation and analytical calculation are shown in the graph in figure 3.9.

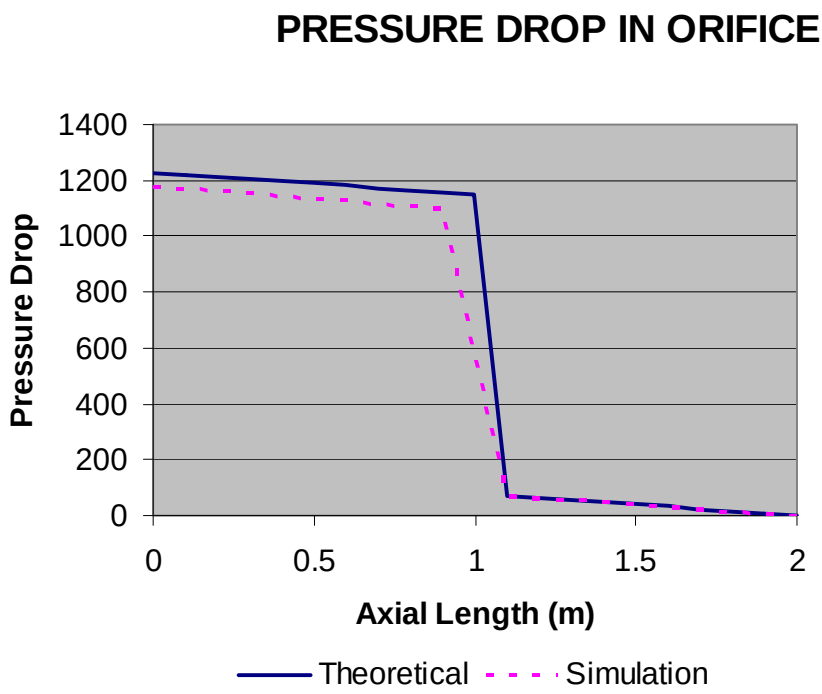

Figure 3.10: Pressure Change in a pipe with orifice by Simulation and Analytical Calculation

It can be observed that pressure change is similar with a slight difference in the point where the drop due to orifice starts to occur. This is because the theory assumes that the drop starts exactly at the orifice itself. The difference in pressure drop is only 3% of theoretical one.

3.3. CFD Modeling of Scaled Model Underground Coalmine

In order to achieve the objective of this investigation, two types of numerical solutions were done using a scaled down underground coalmine. The first one was a steady state condition and the other unsteady state condition. This section discusses the two types of numerical solutions, starting from development of geometries in CAD, through to the

results. As explained earlier, the results were later on validated with experiments whose details are covered in chapter 4.

3.3.1. Step Followed to Get Steady State Numerical Solutions

This section describes in details steps that were taken in order to arrive at the steady state numerical solutions.

3.3.2. Development of Geometry

Scaled-down geometries MG 1, MG 2 and MG 3 that are described in the methodology in chapter 2 were used to get steady state numerical solutions. Since the steps taken to simulate these geometries were the same, the word geometry is used in this section to make the presentation easy.

The geometry and other parameters that were used for simulation were 15% smaller than the size and parameters prevailing in the actual mine. This was done because the experiments to validate the simulations were done on a 15%-scale model of the underground coalmine. The scaling down of mine dimensions and parameters like air velocities are explained in chapter 2.

Solid Works CAD software was used to develop the geometry. The geometry comprising the heading, through-road, jet fan, scrubber and CM was developed in one block. The shape of the CM was just cut in the block in order to minimize the size of the actual volume to be meshed which translates into less number of cells therefore reduced meshing and iteration time. The fan was inserted into the block through assembling. See figure 3.11. The geometry was then stored in Stereo lithography format ready to be imported by star CCM+.

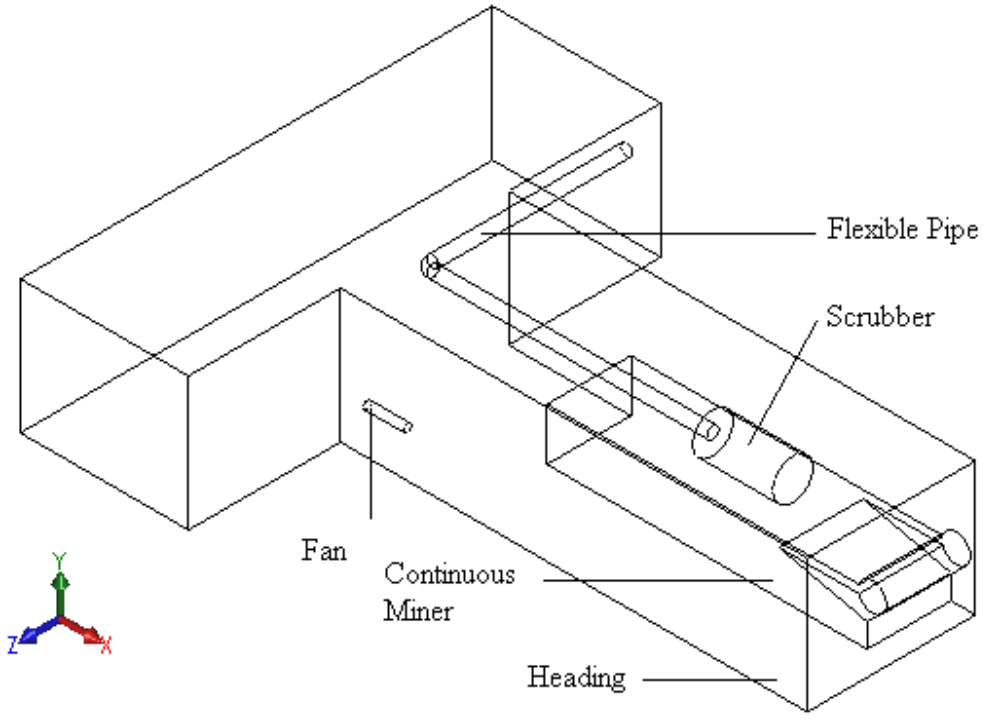

Figure 3.11: Isometric View of MG 1 Done in Solid Works

3.3.3. Importing and Pre-processing the Geometry

The geometry was imported to star CCM+ from solid works as one region and one boundary. Therefore it was necessary to split the geometry so that Star CCM+ should be able to recognize the fan, the tunnel, CM and scrubber. The boundaries were split, renamed and relevant boundary types were specified accordingly. The units of importation were millimetres the same as the one used when the geometry was developed in solid works. The geometry was imported with surface mesh too coarse to give accurate simulation results. Therefore the next step was to re-mesh the surface geometry before volume meshing was done.

As it has already been explained earlier, the volume mesh in a simulation is the mathematical description of the space (or geometry) of the problem being solved. The

volume mesh in Star CCM + can contain either trimmed, polyhedral or tetrahedral type cells for each mesh region, determined via the selection of mesh models. Additionally, prism layers[38] can be automatically included next to wall boundaries and interfaces.

3.3.4. Volume Meshing

A grid is generated in a domain where the fluid flow equations are solved through computational techniques. To obtain good results the appropriate grid must be applied. This section briefly, gives a brief description of the three different types of volume mesh models, explains mesh or grid independence, describes how a decision to use a specific model was made and gives the reference values that were used in the mesh model.

3.3.4.1. Types of Volume Mesh Models in Star CCM+

Tetrahedral Meshing Model

Tetrahedral meshes provide an efficient and simple solution for complex mesh generation problems. Out of the three, it is the fastest and uses the least amount of memory for a given number of cells.

Polyhedral Meshing Model

Polyhedral meshes provide a balanced solution for complex mesh generation problems. They are relatively easy and efficient to build, requiring no more surface preparation than the equivalent tetrahedral mesh. They also contain approximately five times fewer cells than a tetrahedral mesh for a given starting surface.

[38] A prism layer mesh is composed of orthogonal prismatic cells that usually reside next to wall boundaries in the volume mesh. They are required to accurately simulate the turbulence and heat transfer.

Trimmer Meshing Model

The trimmer mesh provides a robust and efficient method of producing a high quality mesh for both simple and complex mesh generation problems. The model is not directly dependent on the surface quality of the starting surface and as such is more likely to produce a good quality mesh for most situations.

In terms of general accuracy for a given number of cells, the trimmer and polyhedral cell type meshes always produce the most accurate solution when compared to tetrahedral mesh [Star CCM+ Notes].

3.3.4.2. Mesh Independence

When solving CFD problems it is important to ensure that the solutions are not affected by the size of the mesh or grid. The ability to retain consistency across varying cell sizes is called mesh independence. Mesh independence can be achieved by taking three runs of the same problem but on very different mesh size. If the solutions from the three runs show little variation then the mesh is deemed to be independent.

In this investigation cell size of 0.1 m was utilized because mesh independence was observed around this size. The details on how the mesh was sized are given in the next section.

3.3.4.3. Reference Value

Before Star CCM+ was commanded to mesh the geometry reference values had to be specified. Reference values determine the size, number and quality of cells among other things. Reference values that were used to mesh the models are shown in table 3.2.

Table 3.2: Reference values that were employed to mesh the model

Parameter	Value
Base value	0.1m
Number of prism layers	1.0
Prism layer thickness (Relative size)	5.0
Surface curvature	36
Surface growth rate	1.3
Surface proximity (# points in gap)	2.0
Surface size o Relative minimum size o Relative target size	 0.1 100
Tet/poly density o Density o Growth Factor	 1.0 1.0
Tet/poly source blending	1.0

The import mesh had 520 faces and the numbers of cells for each mesh model are given in table 3.3.

Table 3.3: Number of Cells for MG 3 for the Three Mesh Models

Mesh Model	Number of Cells
Tetrahedral	53327
Polyhedral	17944
Trimmer	9106

3.3.5. Modeling of physics continuum

A model in STAR-CCM+ defines how a physical phenomenon in a continuum is represented. Essentially, models define the primary variables of the simulation (such as pressure, temperature and velocity) and what mathematical formulation will be used to generate the solution. An appropriate combination of models is necessary for the complete definition of a continuum.

The various models in STAR-CCM+ have varying levels of complexity and functionality, but their major task is to work with the solvers to obtain a solution and to help present the information to the user. Among the tasks of a typical model is to make relevant field functions available to the simulation and to place initial conditions and reference values in the continuum of which it is a part. [Star CCM+ notes]

The model that was used to define the physical phenomenon of steady state solutions is as shown in table 3.4:

Table 3.4: Physics Model of Continuum for Steady State Condition

Space	Three Dimensional
Motion	Stationary
Material	Gas
Flow	Segregated
State of Equation	Constant density
Time	Steady
Viscosity Regime	Turbulent
Reynolds-Averaged Turbulence	K-Epsilon
Optional Physics Model	Segregated Fluid Temperature

3.3.6. Boundary Conditions

After meshing and modelling the physics continuum air velocity values and directions were specified. The air velocity of the jet fan was set at 10 m/s [39] , scrubber air outlet velocity at 2.3 m/s and through road inlet at 0.0665 m/s as scaled down earlier.

3.3.7. Setting up Reports/monitors

Monitors enable summary information from the simulation to be sampled and saved during the solution. This information can then be displayed in an XY plot while the solution is progressing or post-processed after iteration or unsteady time-stepping is complete. They are useful for watching the behaviour of numerical or engineering quantities as the solution evolves, and can be used to define stopping criteria that can stop the solution iteration.

A report presents a computed summary of the current simulation or CPU data. The report summaries are useful for post-processing, and enable engineering quantities to be computed.

After setting monitors and reports then the stopping criteria and solvers are set before initiating iteration process.

3.4. Unsteady State Condition

Unsteady state simulations were done in order to investigate the rate of extracting an initial volume of air in the underground coalmine model. This was later used to determine the optimum position of jet fan for different mine heading lengths in chapter 6.

[39] The velocity value of 10 m/s was used instead of 9.42 m/s because it was difficult to accurately set this velocity.

In the simulation, it was assumed that the test section was initially filled with smoke simply because smoke was used in the verification experiment in chapter 4. Then the jet fan was switched on to bring in flesh air, thereby removing the smoke. The smoke represents the volume of air in the actual mine that is polluted with dust and mine gas as it has already explained in the methodology in chapter 2.

The Multi-Component Gas model was used for this analysis and results were presented in form of XY- plot of Mass Fraction of Air against Time.

3.4.1. Step Followed to Obtain Unsteady State Numerical Solutions

Most of the steps that were done to get unsteady state solution were the same as those for steady state. Only those steps that were different are explained in this section.

3.4.1.1. Development of a Model in CAD

Solid Works CAD software was used to develop the geometry. Geometry MG 3, figure 2.5, was utilized for unsteady state simulation.

3.4.1.2. Modeling of Physics Continuum

For unsteady state a non-reacting multi-component gas and implicit unsteady were selected for material and time models respectively. The initial condition of mass fraction was set as (0.0, 1.0).[40]

The model that was used to define the physical phenomenon of unsteady state solutions is shown in table 3.6.

[40] This implies that there was no fresh air in test section but it was completely filled with smoke.

Table 3.5: Physics Model of Continuum for Unsteady State Condition

Space	Three Dimensional
Motion	Stationary
Material	Multi-component gas
Flow	Segregated
State of Equation	Constant density
Time	Unsteady
Viscosity Regime	Turbulent
Reynolds-Averaged Turbulence	K-Epsilon
Optional Physics Model	Segregated Fluid Temperature

3.4.1.3. Defining Region Conditions, Values and Boundary Conditions

The boundary values were specified as shown in table 3.6.

Table 3.6: Boundary Values

Physical Values	**Jet Fan**	**Through-road Air Inlet**	**Through-road Air Outlet**
Mass Fraction	[1.0, 0.0][41]	[1.0, 0.0]	[0.0, 1.0]
Static Temperature	293 K	293 K	293 K
Static Pressure	N/A	N/A	0 Pas
Velocity Magnitude	10 m/s	0.0665 m/s	N/A

[41] This implies that the jet fan is blowing 100 percent fresh air. This is also the same with the air flowing into the through-road.

3.4.1.4. Solver and Stopping Criteria

An implicit unsteady solver of 1.6 seconds and a maximum inner iteration of 1 were found to produce results similar to the experimental results.

3.4.1.5. Setting up Reports/Monitors

Mass fraction of air was monitored on averaged area of sensor boundaries and the results were plotted against time.

3.5. Results

3.5.1. Steady State Results

Results for MG 3 are presented in details in this section and those for MG 1 and MG 2 are in Appendix F. Star CCM+ is capable of presenting results in many different forms including vectors. Streamline diagrams are given here as they give a better representation of the flow field than would have been the case with vector plots. Figure 3.12 shows the results in orthographic and isometric projections.

Front Elevation

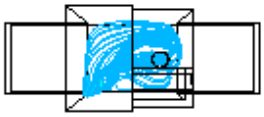

End Elevation

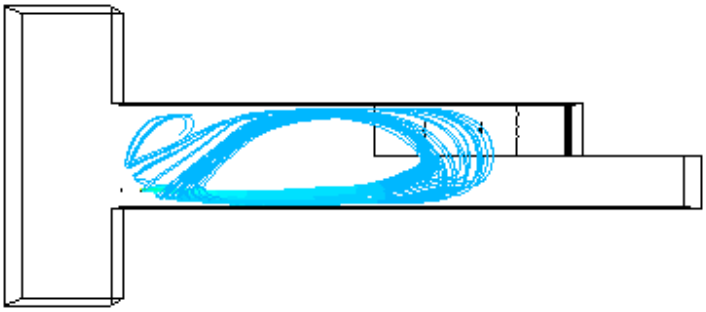

Plan

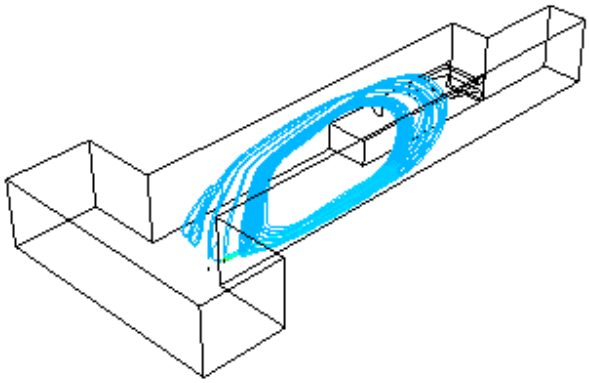

Isometric View

Figure 3.12: Flow Pattern of Air in Mine Geometry 3 Presented in Orthographic and Isometric Views

3.5.2. Unsteady State Results

The CFD model results for the rate of extracting smoke out of the test section for the mine geometries MG-3, using tetrahedral and polyhedral volume mesh models are shown in graph format in figures 3.13 and 3.14. The reason for using tetrahedral and polyhedral volume meshes was to assist in choosing the best volume mesh to be utilized for the rest of numerical analysis. A decision as to which type of mesh to be used for the rest of numerical analysis was made after comparing the results for both types with experimental results.

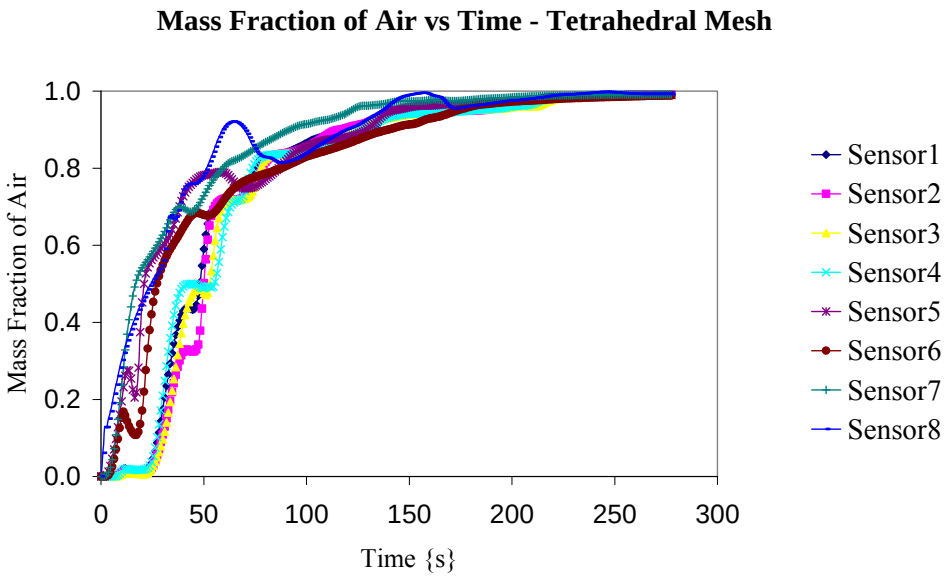

Figure 3.13: Graph of Mass Fraction of Air against Time for MG-3, Tetrahedral Mesh Model.

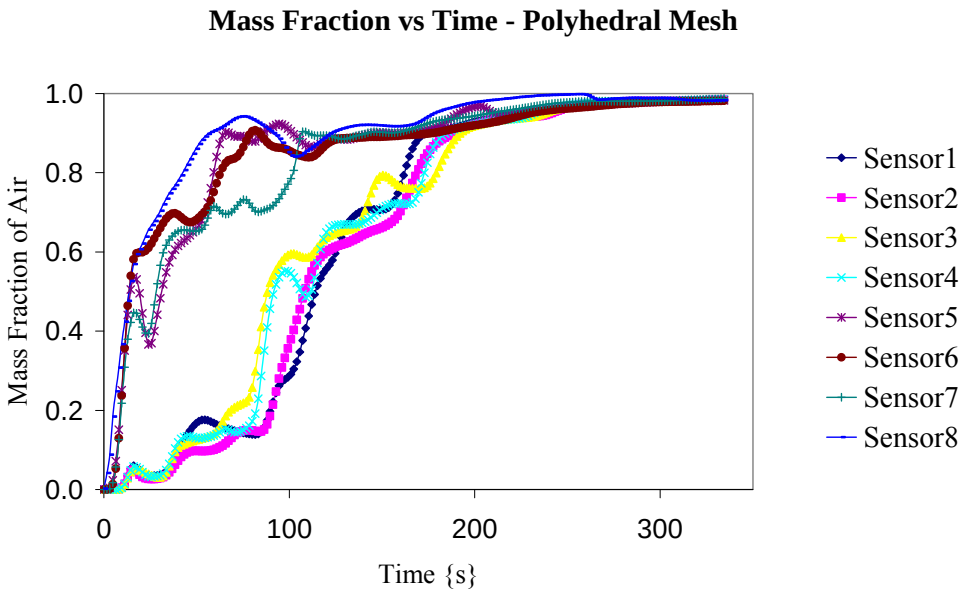

Figure 3.14: Graph of Mass Fraction of Air against Time for MG-3, Polyhedral Mesh Model.

For both mesh models, it can be observed that a graph for sensor 8 takes off first, followed by sensors 5, 6 and 7 and lastly, sensors 1, 2, 3 and 4. This means that extraction of initial volume of air began at sensor location 8, followed by locations 5, 6 and 7 and lastly, 1, 2, 3 and 4. This was so because location 8 was closer to the fan than the rest while sensor 5, 6 and 7 were closer than 1, 2, 3 and 4. Therefore, fresh air from the fan reached sensor 8 first before the rest, etc.

Graphs for sensors 5, 6, 7 and 8 rose sharply soon after taking of then after approximately 50 s their gradients reduces drastically. The slower rate of extraction beyond the 50 s mark could be due to the effects of recirculation and diffusion rate. For sensors 1 to 4 in a polyhedral mesh model the rise before the 50 s mark is not as sharp as the rest. This could be because they are located at the blind end of the heading where the air jet could not penetrate with much strength.

The major difference between tetrahedral and polyhedral mesh models is in the way the graphs for sensors located at blind end of the heading (i.e., sensors 1, 2, 3 and 4) rose. The gradient for polyhedral mesh model was slower than that for tetrahedral. The difference comes about because of the difference in the design of the two volume meshes.

Polyhedral mesh model was chosen because it discriminated the behaviour of the graphs of sensors far much better than tetrahedral mesh model, especially between the one located at blind end and the rest. Secondly, when the graphs for the two mesh models were compared to the similar graphs for experimental results, the trend of the graphs for polyhedral mesh model were found to be closer than those for tetrahedral mesh model.

4. EXPERIMENTAL MODEL AND RESULTS

4.1 Introduction

The correctness of CFD model depends upon correct meshing and physical inputs. Otherwise, one might end up with a simulation that runs and converge very well but gives wrong results. For this reason, it was decided that experimental verification should be conducted in order to ensure the correctness of the CFD model that were constructed in chapter 3, before further numerical solutions were done.

Two types of experiments were conducted. The first was the steady state (time independent) and the other unsteady state (time dependent).

The methodology that was used to carry out investigation for this study was covered in chapter 2. This chapter describes how experiments were conducted on the 15%-scale model and reveals the results. The experimental results are compared with numerical solutions later in chapter 5.

4.2. Experiment Methodology

4.2.1. Steady State Experiment

The first type of experiment was the steady state. The objective of this experiment was to find out the pattern of air flow in the test section. As it has already been mentioned in chapter 2, smoke was utilized to visualize air flow. The flow patterns at each smoke outlet hole were recorded by a visual camera. This was done in order to facilitate repeated observation of flow direction.

The scaled model was configured according to mine geometry MG 1, MG 2 and MG 3, in figure 2.5. For the sake of validation steady state experiments were done using all the three geometries as it had been done in the CFD modelling in chapter 3.

4.2.1.1. Image Capturing

In steady state experiments, the flow patterns of the air in the test section were recorded so that it could be analysed in detail at a later stage. A digital camera with a resolution of was used to record video clips. For each position in the test section two video clips were taken, one from the transparent heading side of the model and the other from the top. Positions for recording the video clips were fixed to ensure that images captured could be accurately checked for repeatability. To achieve this the camera was mounted on a tripod stand and positions for tripod stand were carefully setup according to predefined markings on the floor of the lab as shown in figure 4.1. These are the positions that were used to capture images from the side. Similarly, positions on the camera mounting rail above heading of the model were also marked.

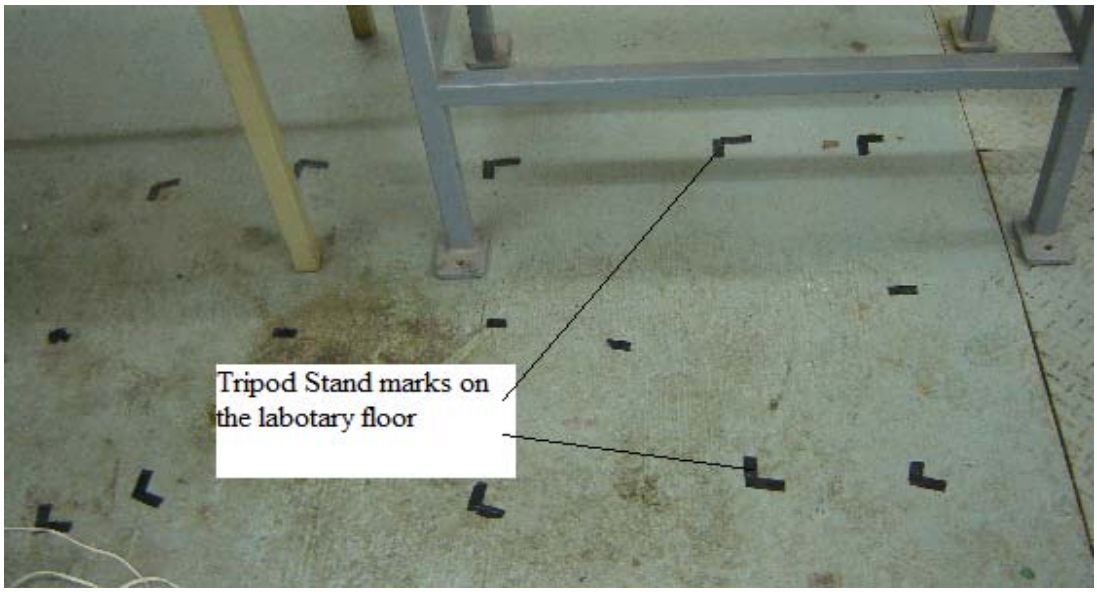

Figure 4.1: Marked positions for tripod stand for the camera

When images were being captured all the lights in the laboratory were switched off and a flow observation light on the scale model was switched on in order to maximise visualisation of smoke.

The following is the procedure that was utilized in process of conducting the experiment:

- The valve on the compressed air system was opened to give air velocity at the nozzle exit of 10 m/s.
- The smoke tubes (labelled 1 in figure 2.3) were inserted into three consecutive holes along the width of the heading and set at same level or height at a single time. The heights that were used are 47 mm, 165 mm and 250 mm, measured from floor level of the heading. These heights are referred to as level 1, 2 and 3 respectively, in the dissertation. This was done to ensure that flow directions at as many positions as possible in the test section are captured. The rest of the holes on the floor were sealed off by insulation tape to avoid air leakages.

- A digital camera was set to capture data in form of video clips. Image capturing process is explained in details in section 4.2.1.1.

- The smoke system, the through-road fan, observation light and scrubber were all switched on while laboratory lights were switched off.

- As soon as enough smoke started coming out of the tubes in the test section the camera was switched on to start capturing images. Two video clips were taken for each position in the test section, one from the side and the other from the top. Most of video images looked similar therefore a log was kept in order to avoid confusing them during analysis.

- After capturing data at one position the three tubes were set again at a different level or next set of holes. And, the third to fifth steps were followed again until all the designated points in the test section were done. It should be noted that some points especially those at level 1 were obstructed by the CM. At those particular holes only points at levels 2 and 3 were captured.

4.2.2. Unsteady State Experiment

The second type of experiment was the unsteady state also referred to as transient state. The objective of this experiment was to find out the time taken to extract the air out of the test section. In this section, air presence measuring system, experiment set up and procedure followed in carrying out the experiment are described.

4.2.2.1. Measuring System

To determine the time taken by air to be extracted out of the test section a measuring system was devised.

In order to understand the experiment set up better the general framework of the measuring system is described first. The general framework consists of three stages as shown in figure 4.2 and are described below [27].

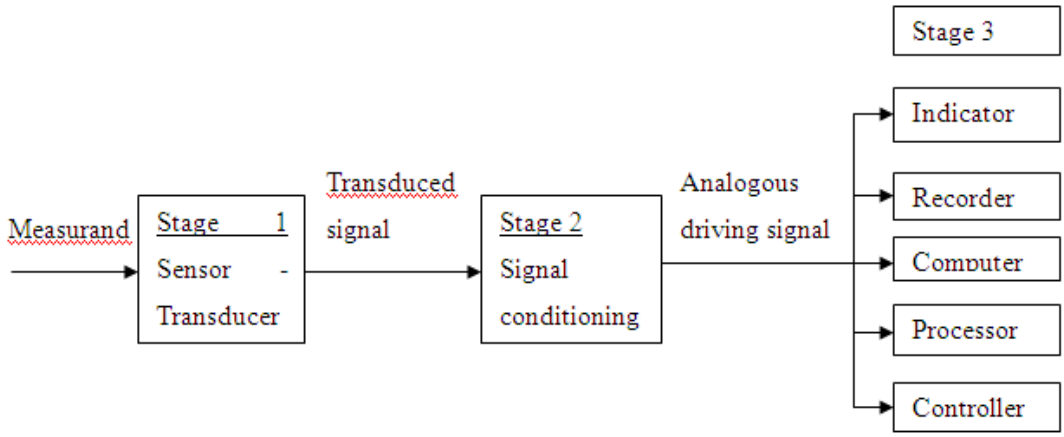

Figure 4.2: Block diagram of the generalized measuring system

First, or Sensor-transducer, stage

Sensors and transducers convert a physical quantity into an electrical quantity. Therefore, primary function of the first stage is to detect or to sense the measurand[42].

Second, or Signal-Conditioning, Stage

The purpose of the second stage is to modify the transduced information so that it is acceptable to the third, or terminating stage. The most common function of this stage is to increase either amplitude or power of the signal, or both, to the level required to drive the final terminating device. In addition, it may perform other operations, such as selective filtering to remove noise, integration, differentiation, or telemetering, as may be required.

[42] Measurand is the physical parameter being observed and quantified or an input quantity to the measuring process [27].

Third or Terminating Readout, Stage

The third stage provides the information sought in a form comprehensible to humans or to a controller. Graphs of resistance against time are utilized for this purpose in this experiment. These graphs were produced on the computer using Microsoft Excel.

Figure 4.3, shows the block diagram for the measuring system that was designed for this experiment and the details of each stage are described below.

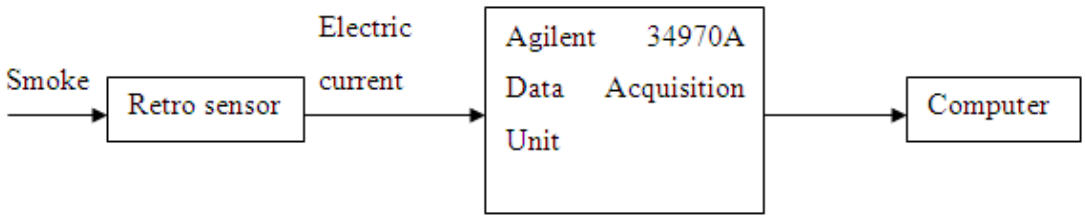

Figure 4.3: Block diagram of the specific measuring system for unsteady state experiment

4.2.2.1.1. Sensor-transducer

Light-detecting transducer called Retro sensor was used to detect the measurand, which in this case was smoke. The retro sensor detects the presence of an object by generating light and then looking for its reflectance from the object to be sensed. Since air which is the sensed object does not reflect light smoke had to be injected into it to serve this purpose. A retro sensor comprising a phototransistor[43], Light Emitting Diode (LED) lamp and a cardboard structure was made and is shown in figure 4.4.

[43] Phototransistor is basically a photodiode followed by one or two stages of amplification incorporated in the same package to enhance the output. Photodiode are semiconductors that produce current flow when they absorb light.

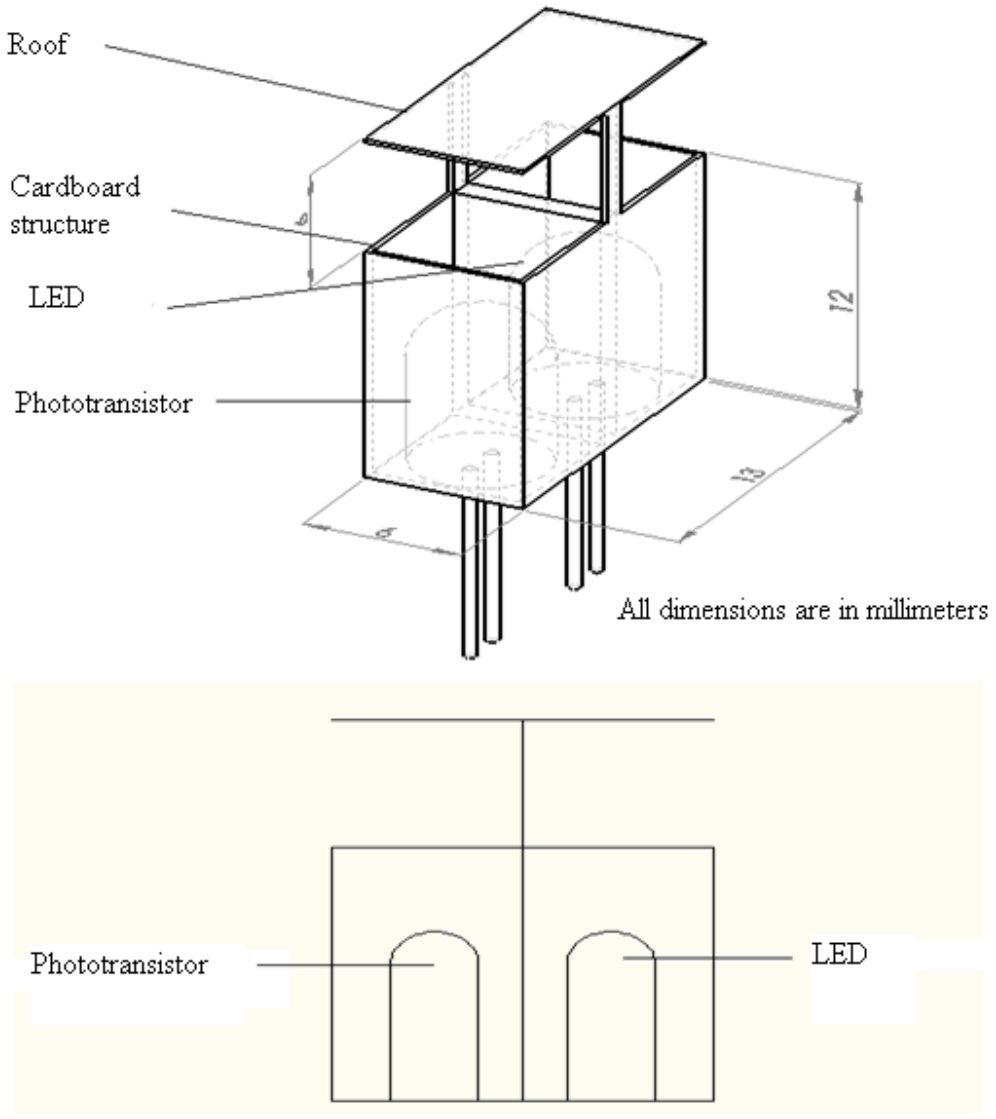

Figure 4.4: Isometric View and a Section of Retro Sensor.

The sensor was made as small as possible to minimize the interruption of air flow in the test section. The surface area for the roof supports was also as small as possible to minimize the flow interruption above the LED lamp and phototransistor. The under surface of the roof was painted black (using non gloss paint) to reduce its reflectance capability.

The sensor gives electrical resistance measurement in ohms.

4.2.2.1.2. Signal Conditioning

Agilent 34970A Data Acquisition Unit (DAU) was used in the experiment for signal conditioning. The signal sent by the retro sensor in form of electrical current (I) was converted to electrical resistance (R).

Data that was captured was stored in the DAU memory to be uploaded into the computer for analysis.

4.2.2.1.3. Terminating Readout

A computer was used to readout and analysis the data from DAU. The computer needs to have relevant software to be able to upload and analyse data from DAU. In this case, Agilent BenchLink Data Logger[44] and Microsoft excel were used for uploading and analysis respectively.

4.2.2.2. Experiment Set-up

Unlike in the steady state experiment where several mine volume were used, in the unsteady state experiment only one volume was utilized.

4.2.2.2.1. Positioning Retro Sensors

The exact locations for the sensors have already been explained in chapter 2 and illustrated in figure 2.5.

[44] Agilent BenchLink Data Logger is a windows-based application designed to make it easy to use Agilent 34970A with a computer for gathering and analyzing measurements.

4.2.2.2.2. Smoker

The smoke producing device that was used in the steady state experiment was found to be lacking for this experiment. The reason being that the smoke flow rate into test section was very low and since the test section was not fully airtight it was very difficult and time consuming to fill the volume with enough smoke to get reasonable data.

Another type of smoke producing device was constructed and represented in figure 4.5. It was able to reduce the time needed to fill the volume dramatically.

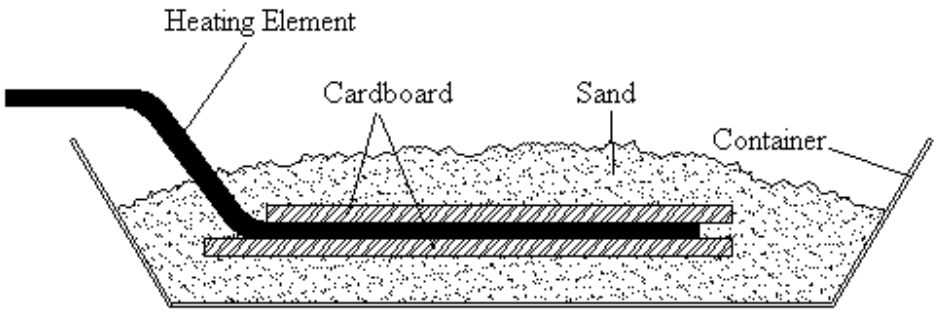

Figure 4.5: Smoker used for transient state experiment

This smoke producing device comprises a coil heating element fixed in a metal tray. The smoke source which in this case was two pieces of commercial hardboard placed underneath and on top of the heating element. Then both the element and the hardboard were buried in sand to avoid a flame. The device was placed almost at the middle of the test section. A cable was attached to the tray for pulling the device out of the test section.

4.2.2.3. Test for Repeatability of Readings

Before using the sensors for the experiment it was necessary to examine if they were able to give repeatable results. This was done by simply switching the light in the laboratory on and off while the DAU was recording the results in ohms. The results for this exercise shown in the graph, figure 4.6 reveals that the sensors gave repeatable results and could be used with confidence. The peaks are for light on and valleys for light off.

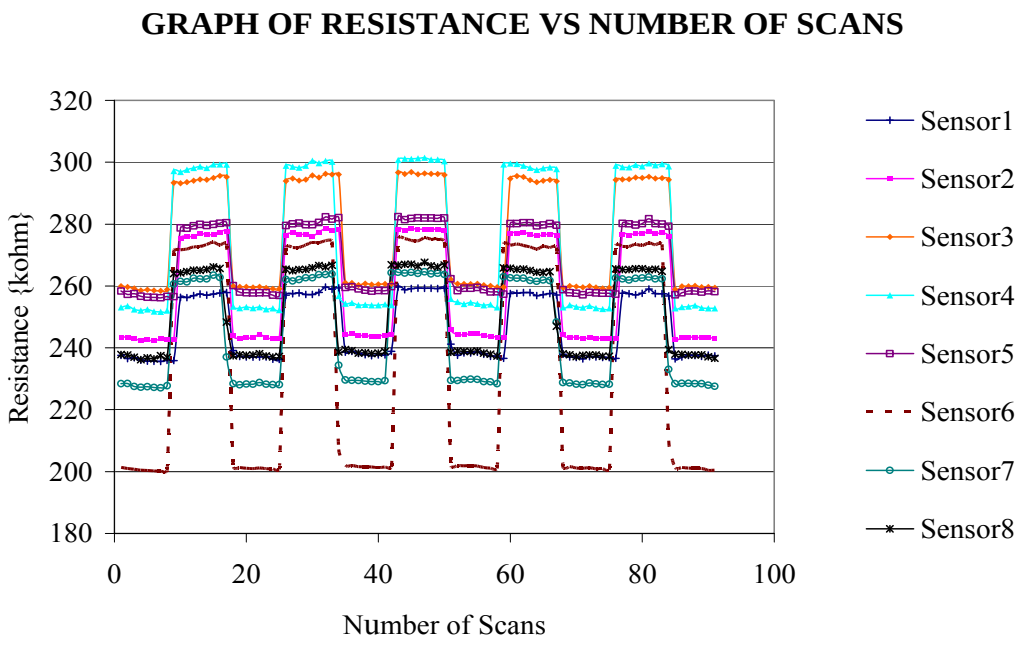

Figure 4.6: A Graph of Resistance against Time with Laboratory Lights on and off

4.2.2.4. Calibration of Retro sensors

In non-specialized use, calibration is often regarded as including the process of adjusting the output or indication on a measurement instrument to agree with value of the applied standard, within a specified accuracy [28].

The sensors had to be calibrated before using them for the experiment so that the necessary adjustments could be made later on the experiment results. The calibration was done as follows:

A regulator transformer was used to vary light intensity of LED lamps of Retro sensors. By adjusting the voltage reading of the regulator transformer the current in the circuit changed consequently, varying light intensity of LED lamps. Since the transformer was an Alternate Current (AC) transformer and the LED lamps were Direct Current (DC) amps, a 3 V adaptor had to be connected to the output of the transformer as shown in the schematic diagram in figure 4.7.

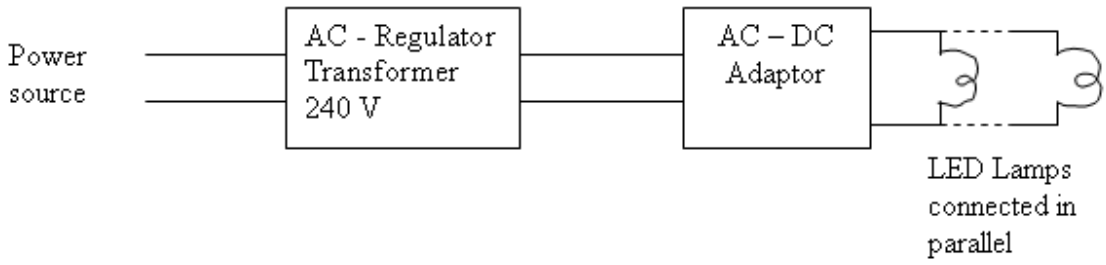

Figure 4.7: Schematic Diagram of Regulator Transformer, Adaptor and LED Lamps Circuit.

The regulator transformer was first set at 220 V and the ohms reading for all the sensors were recorded by DAU. Then the regulator was adjusted upwards at intervals of 5 V up to 250 V with sensor readings scanned at each interval. To ensure accuracy of calibration three average readings were recorded at each regulator transformer interval and the average of the three averages were used in the analysis.

In the analysis the first step was to find the average of all sensors at each particular voltage value. See table 4.1. The averages were then subtracted from each sensor

readings to get deviations. Then graphs of deviation against sensor readings were done for all the sensors. Finally, best line fit of all the graphs were plotted and their formulas were used for adjusting the experiment data. The process of adjusting experiment data for sensor 2 is demonstrated in the next section.

Table 4.1: Average of measurements of all sensors taken at different input voltages

Voltage V	Sensor1 kohm	Sensor2 kohm	Sensor3 kohm	Sensor4 kohm	Sensor5 kohm	Sensor6 kohm	Sensor7 kohm	Sensor8 kohm	Average kohm
220	126.130	317.901	341.616	164.602	110.724	383.385	134.168	130.463	210.249
225	118.389	298.391	317.005	152.744	102.747	348.727	122.039	122.456	197.812
230	112.194	282.777	298.576	143.864	96.7741	323.559	113.232	116.048	185.878
235	105.880	266.862	280.026	134.926	90.7616	298.937	104.615	109.517	173.940
240	102.254	257.725	269.544	129.875	87.3641	285.388	99.8734	105.767	167.224
245	98.416	248.05	258.412	124.512	83.7562	271.29	94.9398	101.796	160.146
250	93.951	236.798	245.653	118.364	79.6205	254.932	89.215	97.1785	151.964

4.2.2.5. Adjustment of experiment measured values

Sensor 2 has been used to demonstrate the adjustment of measured values. Initially, the average readings of all sensors at each voltage were found as explained in previous section. Then deviations from the average for the measured value at a particular voltage were found. Table 4.2 shows how this was done for sensor 2.

Table 4.2: Ohms readings for sensor 2 at different voltage settings, average readings for all sensors and deviations from the average.

Voltage	Readings	Average all sensors	Deviation
V	kohm	kohm	kohm
220	317.901	210.249	107.652
225	298.391	197.812	100.579
230	282.777	185.878	96.8992
235	266.862	173.94	92.9216
240	257.725	167.224	90.5008
245	248.05	160.146	87.9035
250	236.798	151.964	84.8336

The next step was to plot deviations against ohms readings at each voltage setting. This was done in order to find the best line of fit. Figure 4.8 shows the said graph. In this case a linear graph was found to be the best line of fit.

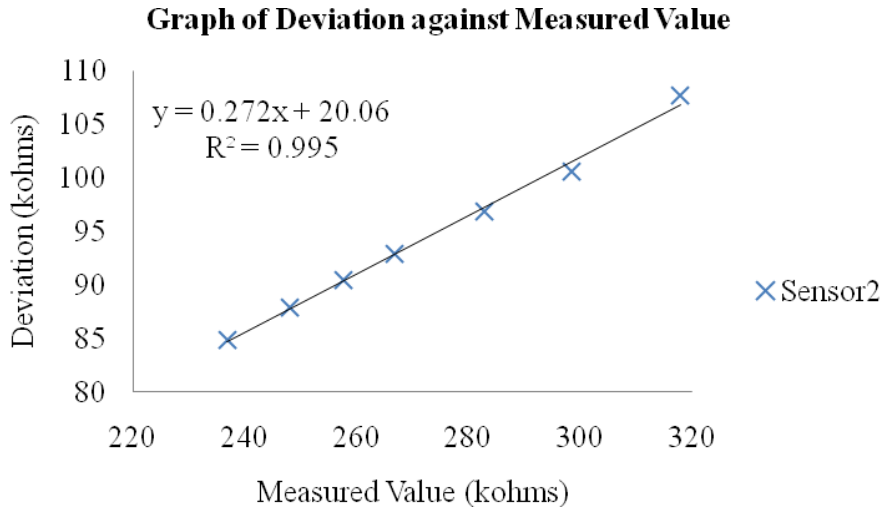

Figure 4.8: Graph of deviation from average reading against sensor readings for sensor 2 showing best line of fit, its R-squared value and equation.

The next step was now to find the value by which the measured values should be adjusted. This was achieved by substituting the measured value for x in the equation of line of fit. Finally, the adjustment value was subtracted from the measured value to get the final value. Table 4.2 shows the adjustments. The final values for the sensors were then plotted against time and this is described in experimental results section.

Table 4.3: Adjustment of measured values for sensor 2

Scan	Measured Value	Adjustment Value	Final Value
1	314.572	105.624	208.949
2	314.445	105.589	208.856
3	314.992	105.738	209.254
4	314.488	105.601	208.887
5	315.367	105.840	209.527
6	315.440	105.860	209.580
7	313.815	105.418	208.398
8	314.064	105.485	208.579
9	315.021	105.746	209.275
10	315.809	105.960	209.849
11	315.336	105.831	209.505
12	313.971	105.460	208.511
13	315.551	105.890	209.661
14	315.338	105.832	209.506
15	315.078	105.761	209.317
16	315.081	105.762	209.319
17	314.739	105.669	209.070
18	314.648	105.644	209.004
19	314.433	105.586	208.847

20	314.899	105.713	209.186
21	314.033	105.477	208.556
22	314.473	105.597	208.876
23	315.094	105.766	209.329
24	312.317	105.010	207.307
25	312.915	105.173	207.742
26	312.229	104.986	207.242
27	312.887	105.165	207.722
28	312.475	105.053	207.422
29	311.235	104.716	206.519
30	311.190	104.704	206.486
31	312.211	104.981	207.229
32	306.739	103.493	203.246
33	305.359	103.118	202.242
34	304.428	102.864	201.564
35	303.518	102.617	200.901
36	302.044	102.216	199.828
37	299.568	101.543	198.026
38	299.047	101.401	197.646
39	299.817	101.610	198.207
40	296.832	100.798	196.033
41	296.028	100.580	195.448
42	293.795	99.972	193.823
43	292.594	99.646	192.948
44	292.394	99.591	192.803
45	286.323	97.940	188.383
46	286.596	98.014	188.582
47	275.608	95.025	180.583
48	275.398	94.968	180.430
49	275.492	94.994	180.498

50	275.224	94.921	180.303
51	276.045	95.144	180.901
52	278.243	95.742	182.501
53	281.342	96.585	184.757
54	282.434	96.882	185.552
55	282.250	96.832	185.418
56	283.280	97.112	186.168
57	285.018	97.585	187.433
58	285.524	97.723	187.801
59	286.665	98.033	188.632
60	289.107	98.697	190.410
61	289.373	98.769	190.604
62	291.660	99.391	192.268
63	294.028	100.036	193.992
64	295.615	100.467	195.148
65	297.340	100.936	196.404
66	297.788	101.058	196.730
67	298.108	101.145	196.963
68	298.534	101.261	197.273
69	299.398	101.496	197.902
70	301.320	102.019	199.301
71	303.085	102.499	200.586
72	303.134	102.512	200.621
73	304.175	102.796	201.379
74	305.305	103.103	202.202
75	305.536	103.166	202.370
76	305.695	103.209	202.486
77	306.177	103.340	202.837
78	306.523	103.434	203.089
79	307.049	103.577	203.472

80	306.191	103.344	202.847
81	306.146	103.332	202.814
82	306.749	103.496	203.253
83	307.622	103.733	203.889
84	307.584	103.723	203.861
85	308.486	103.968	204.518
86	308.526	103.979	204.547
87	309.158	104.151	205.007
88	308.443	103.957	204.487
89	308.062	103.853	204.209
90	307.993	103.834	204.159

The line fit equations for measured values of all sensors are shown in table 4.4 while ohms readings, deviations from average and the best lines of fit for the other sensors are shown in Appendix F.

Table 4.4: Best line of fit equations

Sensor	Best Line Fit Formula
1	$y = 0.832x - 20.06$
2	$y = 0.272x + 20.06$
3	$y = 0.383x - 1.159$
4	$y = 0.322x – 4.496$
5	$y = 0.901x + 1.159$
6	$y = 0.539x - 35.66$
7	$y = 0.363x + 30.86$
8	$y = 0.771x – 20.05$

4.2.2.6. Experiment Procedure

The following activities had to be carried out to complete the unsteady state experiment:

- Connect phototransistor cables to DAU card. Make sure that all the necessary parameters relevant to this experiment are set. These include: activating the channels and set them to ohms in order to read resistance, auto range and resetting the time. Scanning limit was set to continuous and scan interval to 1 second.

- Place the smoke producing device inside the test section.

- Seal off both the inlet and outlet of the through-road and replace the top cover of the heading of mine model.

- Switch off laboratory lights to avoid their effect on the experiment and switch on the LED lamps.

- Press the scan button on DAU to start recording data. Scanning was left to run for about five minutes before smoke was injected into the test section. This was done to ensure an initial horizontal graph was achieved. The starting time for scanning process was recorded for crosscheck purposes.

- After approximately five minutes of scanning the smoker heater was switched on. The heater was switched off after enough smoke filled the test section. This was based on the personal judgement. It would have been better to completely saturate the test section with smoke but the smoke leakage made the environment uncomfortable so that the experiment had to be done in the shortest time possible. It was observed that when the heater was switched on, the readings for all sensors increased significantly by approximately 10 000 ohms and dropped by the same

margin when it was switched off. Switching on and off time of the heater were also recorded.

- The smoker was moved to the through-road inlet by pulling the soft wire attached to smoker tray.

- The jet fan, scrubber fan and the through-road fan were switched on. At the same time the seals on the through-road inlet and outlet were removed. The smoker was also taken out of the test section. This marked the beginning of smoke extraction process. Time at which smoke extraction began was recorded.

- Smoke extraction process was left to run until when all the smoke was removed from test section. This was determined by the readings on the DAU being consistent (not fluctuating much), then scanning was stopped.

- Data was uploaded into the computer for analysis.

4.3. RESULTS

4.3.1. Steady State Experiment Results

The information that was collected in form of video clips was converted into vector format for them to be easily analysed. Either an arrow or a circle was drawn at each point where the smoke entered the test section. An arrow indicates smoke direction and a circle indicate that no definite direction was observed. Please note that the arrows indicate direction only and not velocity magnitude.

To illustrate how the vector diagrams were constructed from video clips, points E1, E2 and E3 on MG-2 as shown in figure 4.9 and 4.10, representing side view and top view, respectively.

Figure 4.9: Top View of Points E1, E2 and E3 on MG-2

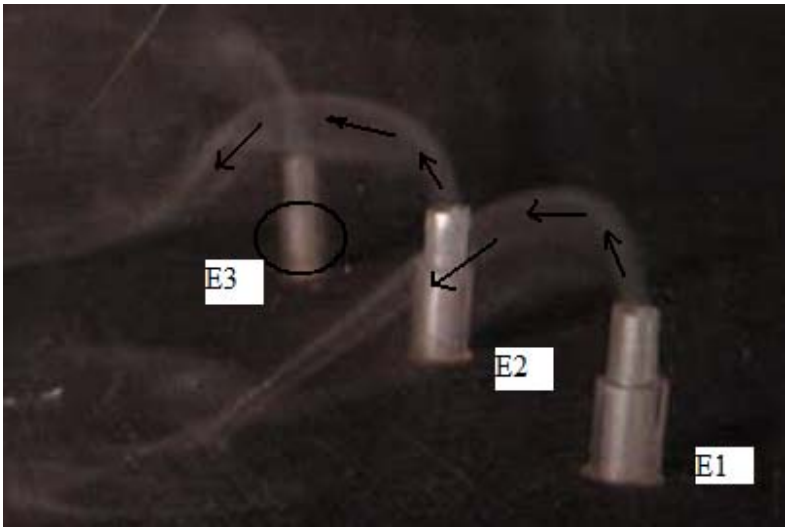

Figure 4.10: Side View of Points E1, E2 and E3 on MG-2

The air flow represented by the three white streams that are coming out from the tubes can be seen clearly on the two figures. The arrows are drawn on each stream to indicate smoke direction.

Figure 4.11 shows the complete vector diagram of MG-3 from the top at levels 1, 2 and 3 and figure 4.12 shows the same vector diagram from the side at planes 1 to 6. The dots are the positions where the smoke enters the test section from the tubes, the arrows indicate flow direction that were definite and circles around the dots indicate that the flow direction could not be determined at all and a circle and an arrow indicate that despite the smoke circulating it was flowing to a particular direction most of the time. Failure to determine flow direction at particular point was a result of continuous change of smoke direction during the whole period of observation in other words there was no dominant direction of flow. The vector diagrams for MG 1 and MG 2 are in Appendix G.

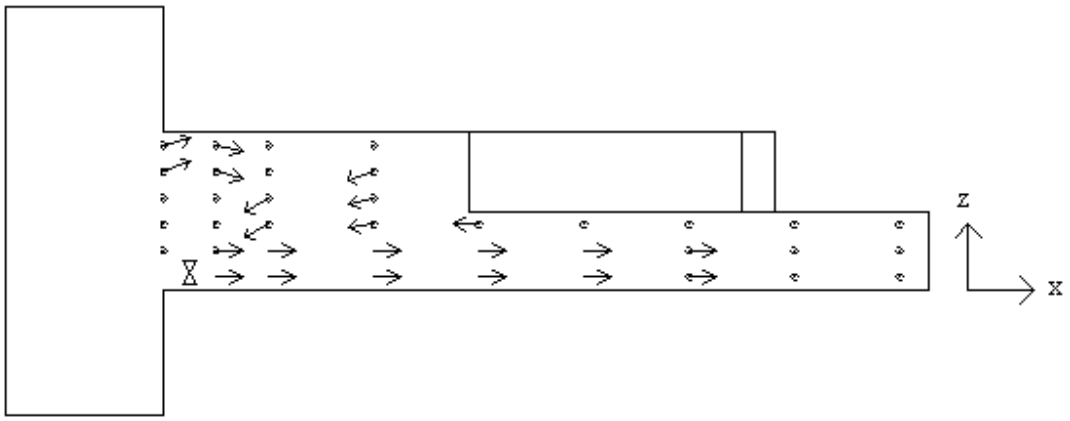

MG 3 Level 1 (At a height of 47 mm from the floor)

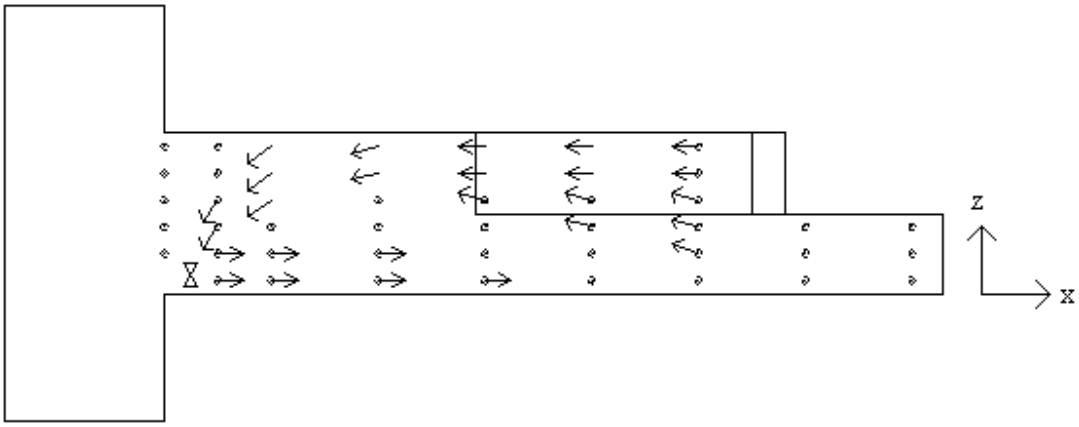

MG 3 Level 2 (At a height of 165 mm from the floor)

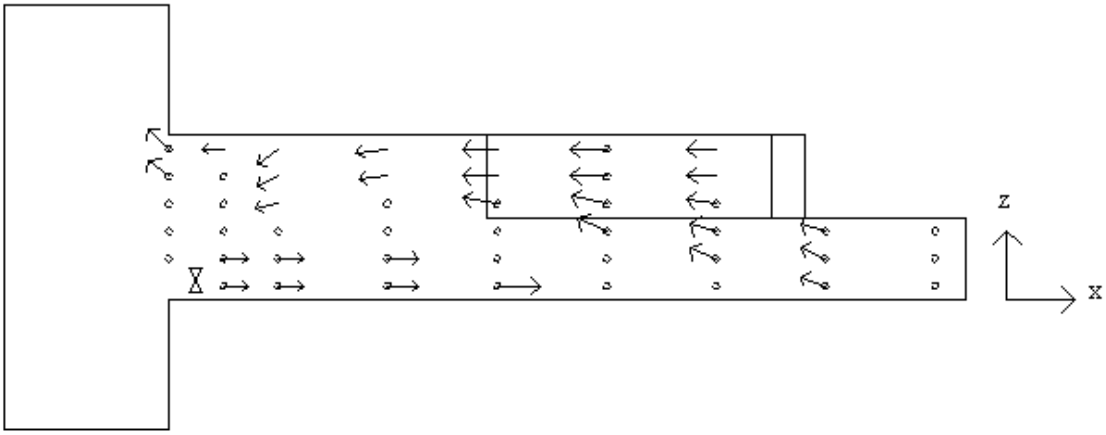

MG3 Level 3 (At a height of 250 mm from the floor)

Figure 4.11: Vector diagrams developed from video images for mine geometry, MG-3, at levels 1, 2 and 3, as seen from the top.

MG 3 Section 1

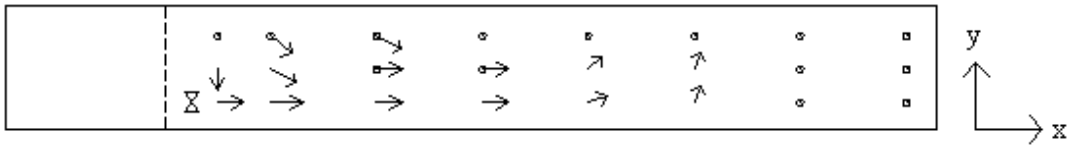

MG 3 Section 2

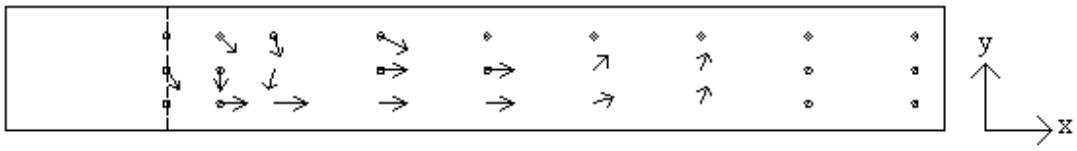

MG 3 Section 3

MG 3 Section 4

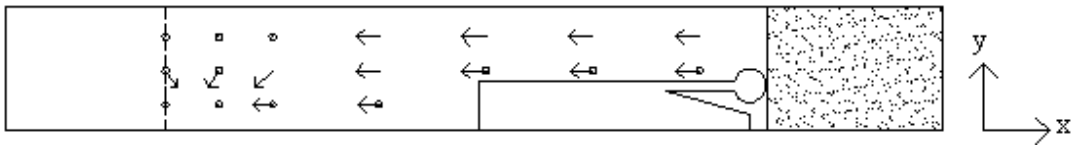

MG 3 Section 5

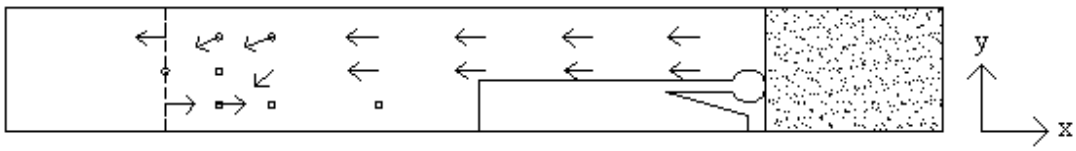

MG 3 Section 6

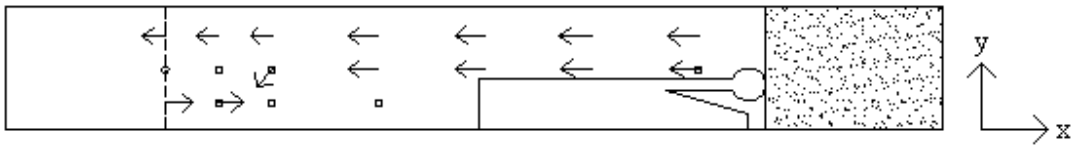

Figure 4.12: Vector diagrams developed from video images for mine geometry, MG-3, at sections 1, 2, 3, 4, 5 and 6, as seen from the side.

4.3.2. Unsteady State Experiment Results

4.3.2.1. Processing of Measured Values

The raw data whose plots are shown in Appendix H. went through the following process in order to come up with the final graph shown in figure 4.13.

- Firstly, the effects of electric current fluctuation (see appendix J) when the smoke heating element was switched on and off were removed. Then all the other suspected effects of electric current fluctuation due to switching on or off other electrical machines or devices in the laboratory were also removed.

- Secondly, the data was then adjusted by calibrating measured values, as explained in 4.2.2.4.

- Finally, Microsoft Excel was utilized to plot the results.

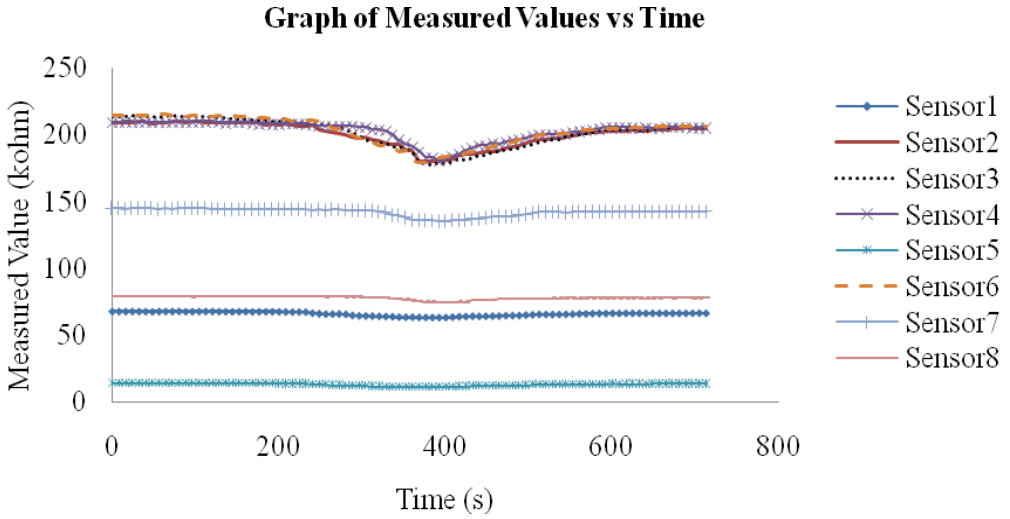

Figure 4.13: Graph showing the concentration of smoke against time around the sensors in the scaled model.

4.3.2.2. Explanation of the Results

After calibrating it was expected that the plots for all the sensors will be close together as those of sensors 2, 3, 4 and 6. The results in figure 4.14 reveals that something went wrong with sensors 1, 5, 7 and 8 during the experiment. The probable reasons for this error could be that conditions under which the calibrations were done might have changed during of the test. For example, the LED or phototransistor might have shifted. Since the anomaly was discovered too late while the author way from experiment facility, it was decided to ignore the malfunctioning sensors in this analysis. Therefore the plot for normal sensors was done as shown in figure 4.14.

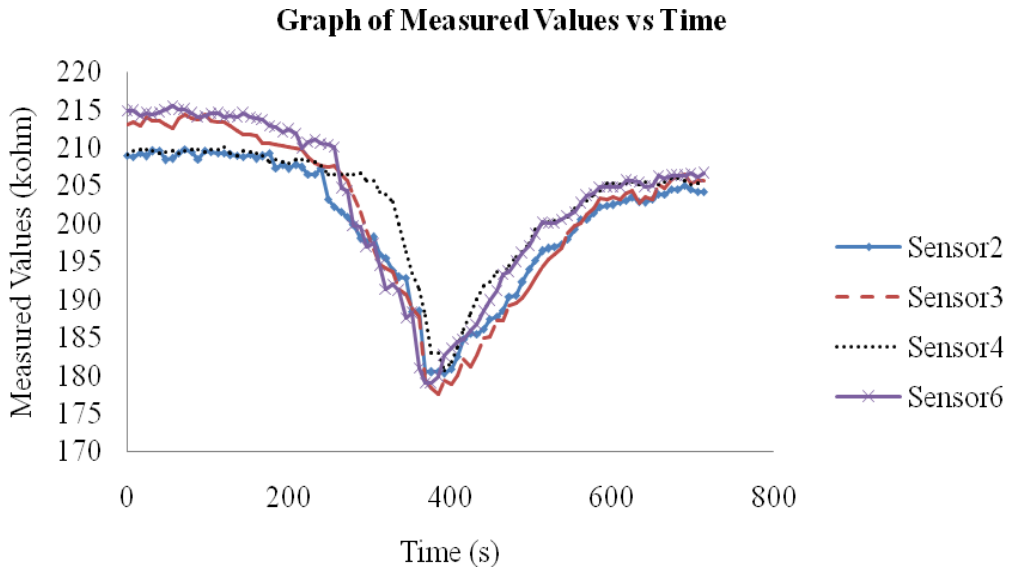

Figure 4.14: Graph showing the concentration of smoke against time around the sensors in the scaled model after removing malfunctioning sensors.

The removal of these sensors would not affect the investigation so much since validation process could be done using the remaining four sensors. And since the area of interest

was the time taken to extract initial air out of test section the measured values of the so called malfunction sensors produced sensible results. This is covered in chapter 5.

Table 4.1: Explanation of the Results in a Graph Shown in Figure 4.15

Time in Seconds	What is happening?
0 – 200	The lines of the plots for all the sensors are almost horizontal. This was the time between the scan was initiated and before the test section was filled with smoke.
200 - 400	The lines steeping downwards rapidly. This was the time when the test section was filled with smoke.
400 - 740	At approximately 400 seconds jet fan and through-road fan were switched on to start extracting the smoke out of test section. As soon as the fans are switched on the plots steeps upwards rapidly up to about 600 seconds mark where the gradient reduces significantly.
740	The plots become horizontal again. This signifies that the smoke is completely extracted.

From this analysis it can be deduced that it took approximately 360 seconds to completely remove the smoke out of the test section.

4.3.2.3. Variations and Probable Causes

In an ideal case the plots for all the sensors should return back to the starting reading when all the smoke is extracted out of the test section. This is not the situation with the experimental results. After the experiment was conducted it was observed that a brownish thin substance[45] had coated the LED lamps, phototransistors and every surface that came into contact with the smoke. The thin coating reduced the light intensity from LED lamp and that penetrating the phototransistor. This was the reason the graph could not return to the starting value.

[45] This substance is believed to be a by-product of hardboard combustion.

5. COMPARISON BETWEEN CFD AND EXPERIMENTAL RESULTS

5.1 Introduction

The main objective of this work was to demonstrate the possibility of solving coal dust and mine gas concentration problems in underground coalmine by using CFD modeling. The first step towards this goal was to model the standard[46] method of ventilation in the coalmines. The CFD model was then validated with experimental results done on scaled down coalmine model.

The validation was done by comparing the numerical and experimental solutions. Similarity between the two analysis means that the CFD results can be trusted. And further numerical analysis can be carried out with confidence.

5.2 Comparison of Results

In order to gain more confidence in numerical analysis both the steady state and unsteady state results of the two models were compared. Steady state results were done first, followed by the unsteady state.

Two unsteady solutions were done using tetrahedral and polyhedral types of volume mesh the comparison of these results against experimental results assisted in choosing the mesh to be used for the rest of numerical analysis. The polyhedral model produced results that were closer to the experiment than the tetrahedral meshed model hence the polyhedral was utilized for the rest of numerical analysis.

[46] In the standard method the jet fan is positioned 1.2 m from the entrance, 1 m from the side wall and 0.7 m high.

5.2.1. Steady State Results

Although the experimental results in chapter 4 are presented in plan and front views only, the end view is interpolated from the two so that a three dimension comparison analysis is possible. The steady state results in chapter 4 were summed up first before the comparison process could be carried out. The results for mine geometry 3 (MG 3) are presented in detail in this section while those for MG1 and MG2 are given in Appendix J.

Please take note that vectors or streamline for scrubber are not included in steady state analysis. This is because the experimental views do not include them since it was difficult to visualize them.

5.2.1.1. Summing up of Results

The first step in this analysis was to sum up the three top views and the six side views as seen in vector diagrams, figures 4.13 and 4.14 to a single top view and single side view, respectively. Then the interpolation of the second side view was done before the comparison process could be done. To achieve this it was imaged that the three levels of the top views vector diagrams were transparent and placed directly on top of each other to come up with one top view vector diagram. The same process was done with the six side sections to come up with one side view vector diagram. See figures 5.1. Only those points with a definite direction were considered in the final analysis. And for those points with more than one definite direction a resultant direction was assumed. Then a few vectors were interpolated to complete the picture.

The second step was to bring in the similar views from CFD models from chapter 3 (figures 3.10] and place them side by side with the corresponding vector diagrams in order to make the comparison process easy. The two summed up vector diagrams are shown side by side with the CFD vectors diagrams in figures 5.2 and 5.3. And the interpolated second side view vector diagram is shown in figure 5.4.

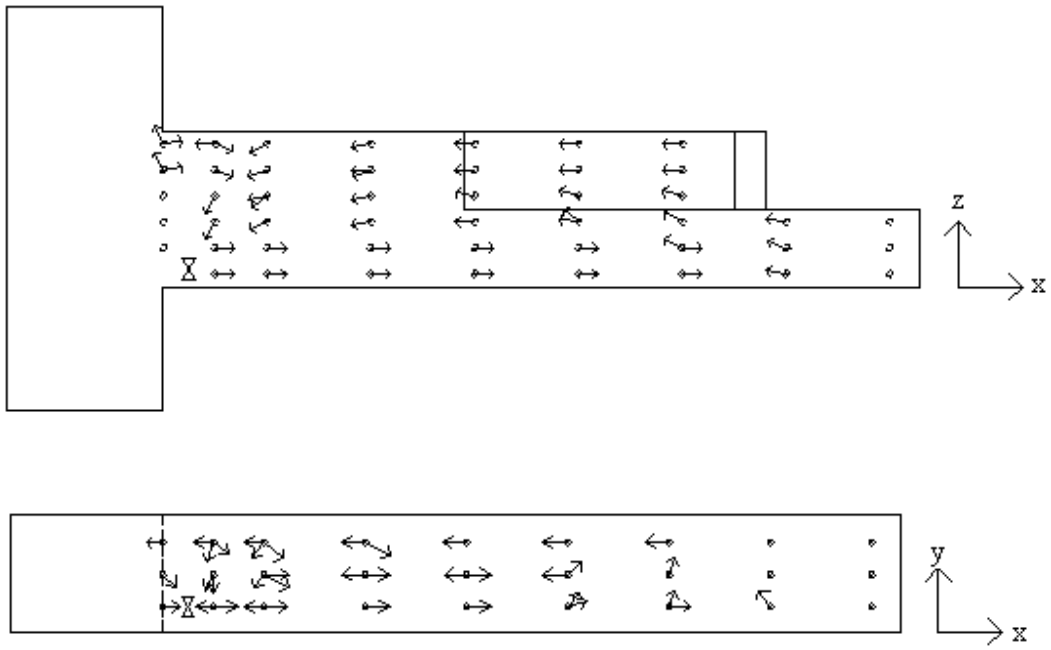

Figure 5.1: Top view and side view showing flow direction at all points before the final analysis was done.

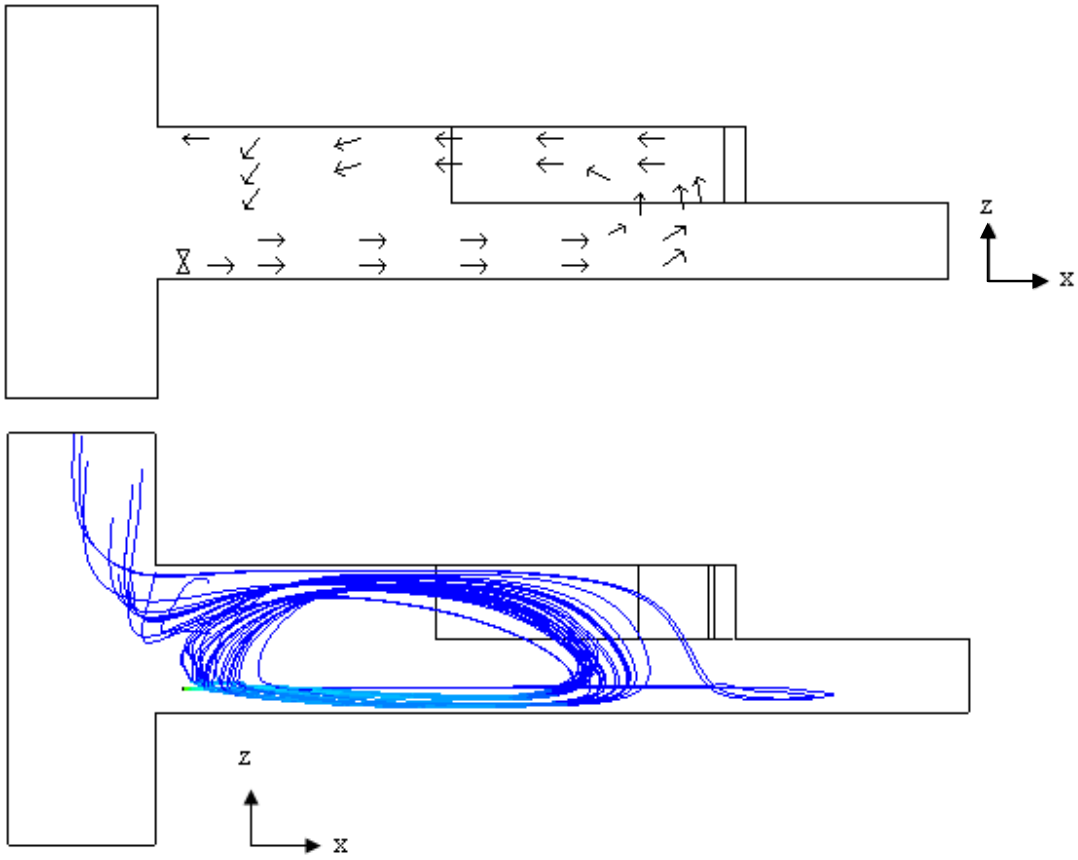

Figure 5.2: Plan view experiment and CFD results.

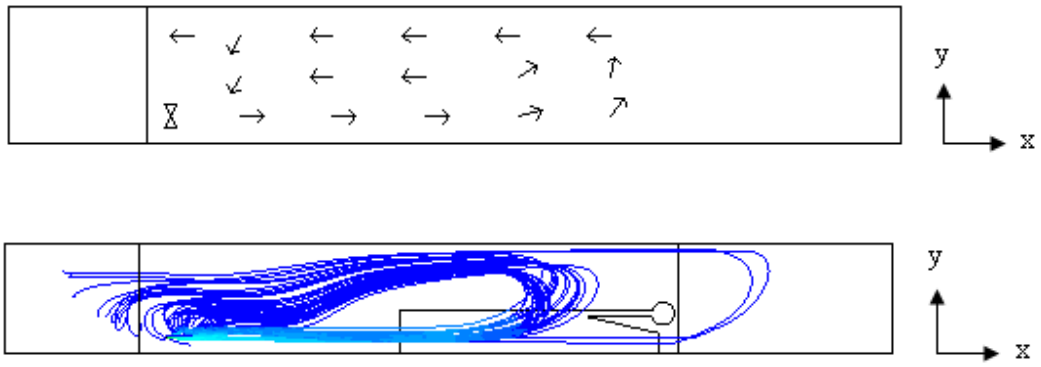

Figure 5.3: Front view experiment and CFD results.

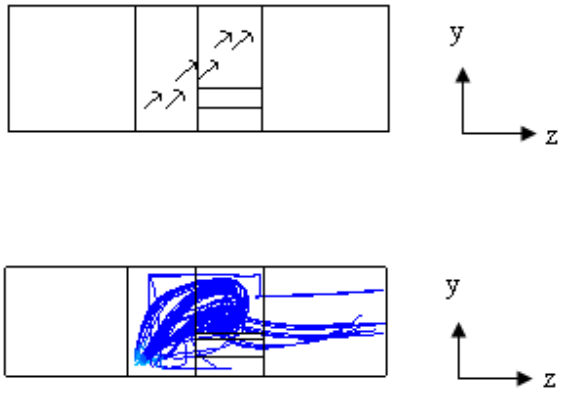

Figure 5.4: End view experiment and CFD results.

5.2.1.2. Results Analysis

The air flow pattern obtained both by experiment and CFD methods for the other two geometries i.e., MG-1 and MG-2 are shown in appendix J. The experimental and CFD air flow patterns look similar in all the three mine geometries. Therefore it can be said with certainty that CFD can be utilized to solve steady state problems of coalmine scaled-down model.

5.2.1.3. Variations and Probable Causes

Although the results by experiment and CFD methods look similar the air flow at some points is not exactly the same. This is so because in the experimental method points of entry for smoke were only at specific locations therefore could not depict air flow accurately.

5.2.2. Unsteady State Results

As it has already been explained, the objective of this analysis was to investigate the rate of extraction of initial volume of air out of the test section. Therefore the results for both

CHAPTER 5: COMPARISON: CFD AND EXPERIMENTAL RESULTS

CFD model and experiment were presented in form of time graphs in order to make comparison process easy. Due to the nature or design of the experiment the results were presented as a graph of resistance in ohms against time while the numerical results were presented as a graph of mass fraction of air against time.

To simplify the comparison, the resistance quantities on the y-axis of experimental results were first converted to mass fraction of air so that both results can be presented on a single graph. Readings for sensor 2 in table 4.3 is used here to demonstrate the conversion of experimental readings from ohms to mass fraction of air in the following steps:

i. The average sensor reading at the scan range where the graph seems to be flattening was found. This is a point when the smoke is almost completely extracted out of the test section. For sensor 2 the average reading was found to be 204.488 kohm. This was regarded as the final reading.

ii. The reading at the point when the fan was switched on to begin extraction process was regarded as the first reading. Extraction began at scan 50 and for sensor 2 the reading was 180.303 kohm.

iii. The first reading was then subtracted from the final reading. For sensor 2,

204.488 - 180.303 = 24.185 kohm

iv. Then first reading was subtracted from all the other reading from scan 50 to the final reading. For sensor 2, scan 50 gives zero and scan 90 is approximately 24.185 kohms.

v. Finally, solution of step iv was divided by solution of step iii to get experimental readings in mass fraction of air. For sensor 2, the solution for scan 50 is zero, for scan 90 it is 1 and for scans in between the solution are fractions.

5.2.2.1. Results Analysis

Each sensor position is compared and analysed separately in order to have a clear picture of what is happening at specific points. Graphs for sensors 2, 3, 4 and 6 for both CFD model and experimental model are shown in figures 5.5 to 5.8.

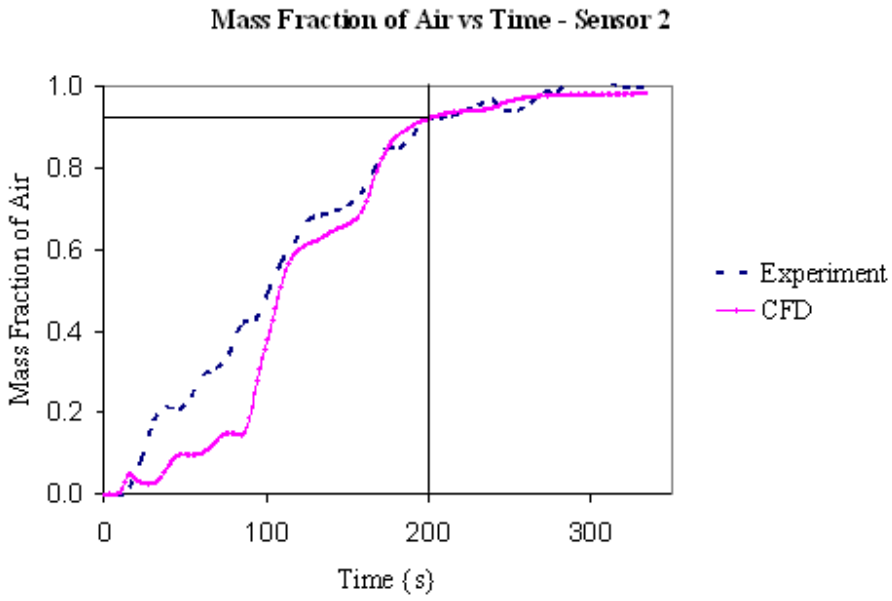

Figure 5.5: Comparison of the rate of extraction of initial volume of air by experiment and CFD methods at location sensor 2.

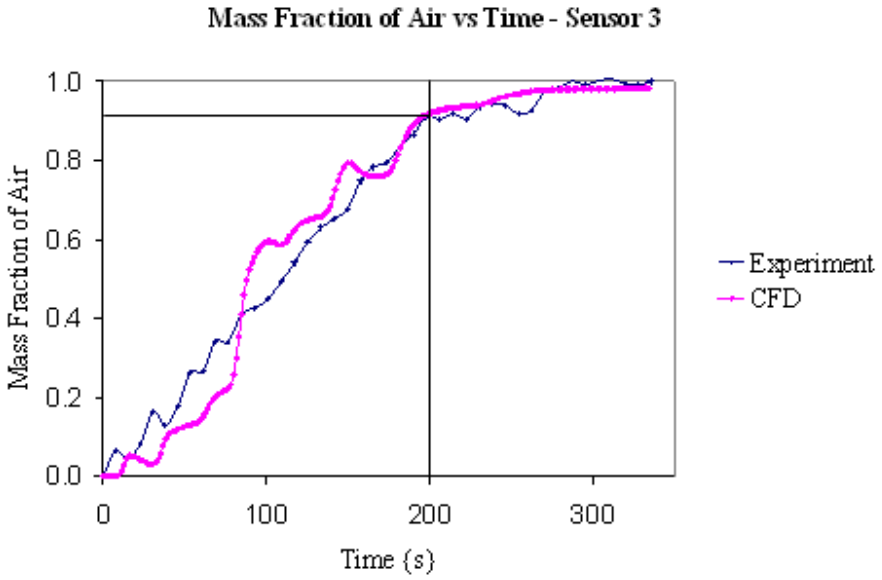

Figure 5.6: Comparison of the rate of extraction of initial volume of air by experiment and CFD methods at location sensor 3.

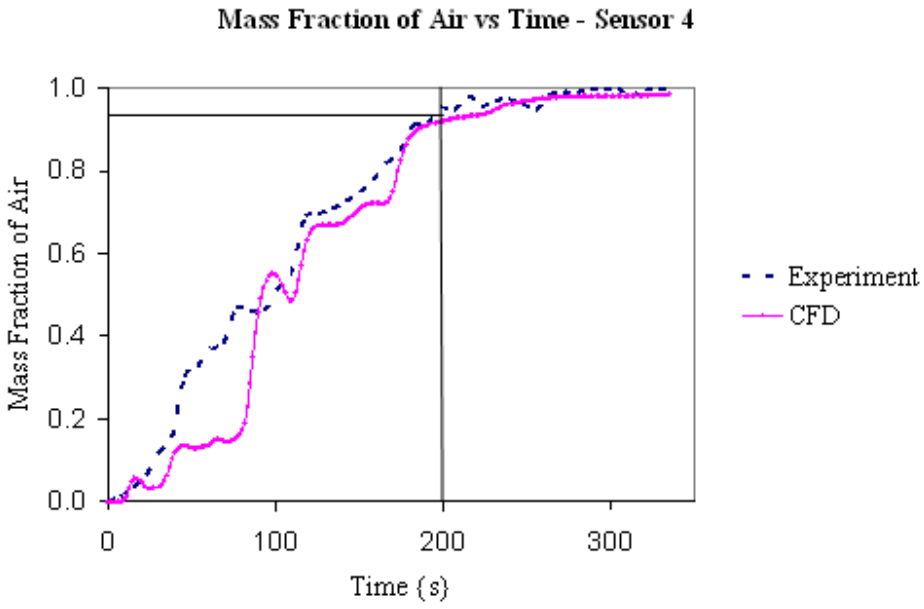

Figure 5.7: Comparison of the rate of extraction of initial volume of air by experiment and CFD methods at location sensor 4.

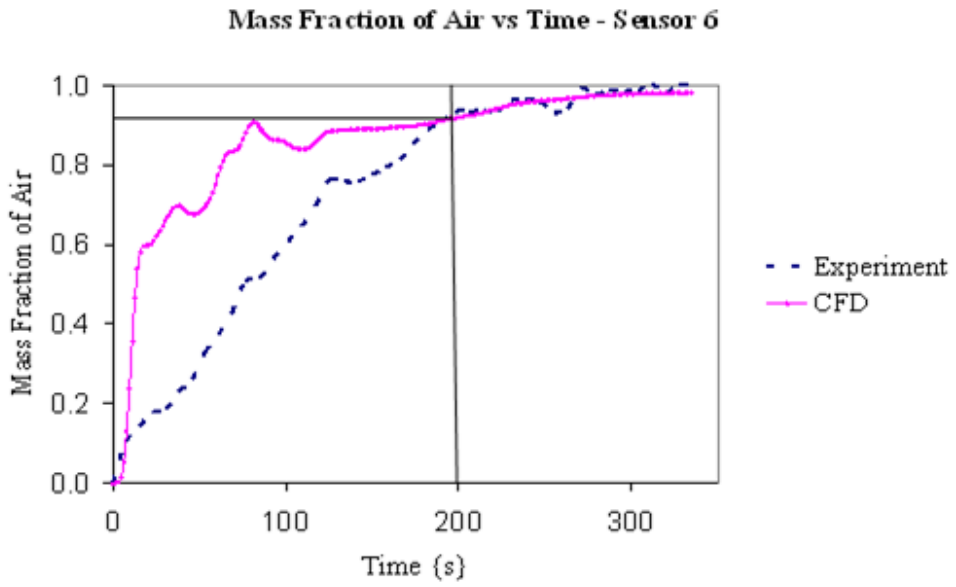

Figure 5.8: Comparison of the rate of extraction of initial volume of air by experiment and CFD methods at location sensor 6.

From the comparison graphs shown in figures 5.4 to 5.7, the rate of air extraction at heading locations sensor 2,3,4, and 6 can be said to be similar because both plots shows almost the same pattern and are close to each other. Although the plots at sensor location 6 are not as good as the rest they also look similar. Therefore it can be concluded with confidence that both CFD and experiment methods produce similar results. In other words CFD method has been verified to be true therefore further numerical analysis can be confidently pursued.

5.2.2.2. Variations and Probable Causes

As it has already been observed the plots for CFD and experiment results being compared in the graphs are not exactly the same but are similar. Some of probable causes of discrepancies between the two results are:

- Friction between air and model wall which exits in the experiment was disregarded in the CFD analysis.

- In the experiment the process of opening heading inlet and outlet and the switching-on of the fans did not happen simultaneously but a few seconds after each other while in CFD everything happens the moment the program starts running.

- The K-ϵ model was used in numerical analysis. The constants in the model relations have recommended values for boundary layer calculations. The values available are, unfortunately, not universal to all fluid problems including recirculating flows [15]. Therefore, it is possible that the constant used for modelling was not the right one.

CHAPTER 6: FAN POSITON AND OPTIMIZATION

6.0 FAN POSITION OPTIMIZATION

6.1 Introduction

After proving, in chapter 5, that CFD modelling can be utilized to solve ventilation problems in the heading of scaled down underground coalmine model the next step was to find the fan positions that result in the shortest time of air extraction for different heading lengths and widths.

This chapter explains the methodology that was used to find optimum fan positions and presents a method that can be used to determine the optimum jet fan positions for any other heading length and width within the concerned heading dimensions.

6.2 Methodology

Five different lengths at mining progression of 7 meters in the actual coalmine heading were chosen for this exercise. The lengths are 7 m, 14 m, 21 m, 28 m and 35 m and are equivalent to the following scaled down model: 467 mm, 933 mm, 1400 mm, 1867 mm and 2333 mm respectively. And two different heading width, a full and half width with scaled down dimensions 210 mm and 420 mm respectively were also chosen. There were five different mine geometries for each heading width summing up to ten geometries all together.

The geometries representing these mine progressions were prepared in CAD as before. In order to search for the optimum position of the fan for different mine progressions, several geometries were done for each progression with a jet fan at different positions. The fan position was only varied along the heading length but its position with respect to the floor and the side wall remained standard i.e. 0.7m and 1.0 m, respectively. Therefore the fan position presented in the rest of this dissertation is measured along the heading length with the entrance of the heading as a datum. See figure 6.1.

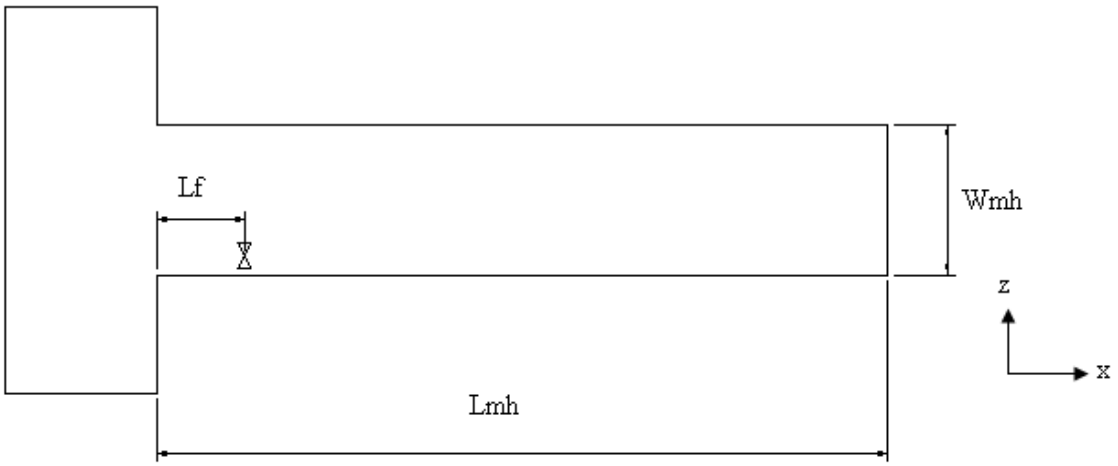

L_f = Fan position with respect to heading entrance

L_{mh} = Scaled Model Heading length

W_{mh} = Scaled Model Heading width

Figure 6.1: Plan View of the mine showing fan position

After the geometry was prepared it was then exported to Star CCM+ for meshing, modeling and iteration. To ensure correct results the parameters that were used in the numerical analysis were exactly the same as the unsteady state analysis in chapter 3. But unlike in chapter 3 where the presence of smoke was detected by sensors located at a number of different positions in the heading in this analysis the wall at the blind end of the heading was used for this purpose. This is because the blind end is the most problematic area as far as dust and mine gas extraction in the heading is concerned.

Graphs of mass fraction of air against time were plotted for each fan position of a particular geometry and the fan position that resulted into the shortest extraction time was considered optimal.

The first geometry to be done was the full heading length, i.e. 2333 mm in the scaled model, and it is explained in details here to demonstrate how the searching exercise for optimum fan positions for different heading lengths were accomplished. Initially, the extraction time for standard position, i.e. 80 mm (1.2 m equivalent in an actual mine) from heading entrance, for a full width geometry was found. Then the fan was positioned at 0 mm (right at heading entrance), 500 mm and 1000 mm to get a rough idea of a probable optimum position of the fan.

6.3 Results

The results for the four position 80 mm, 0 mm, 500 mm and 1000 mm are shown in figure 6.2 and give the following extraction times in seconds: 165 s, 285 s, 560 s and 765 s, respectively. Please note that the extraction time was read at a mass fraction of air of 0.99. This is the reading were the graph appears to touch gridline 1.0 therefore it is very easy to see with naked eyes.

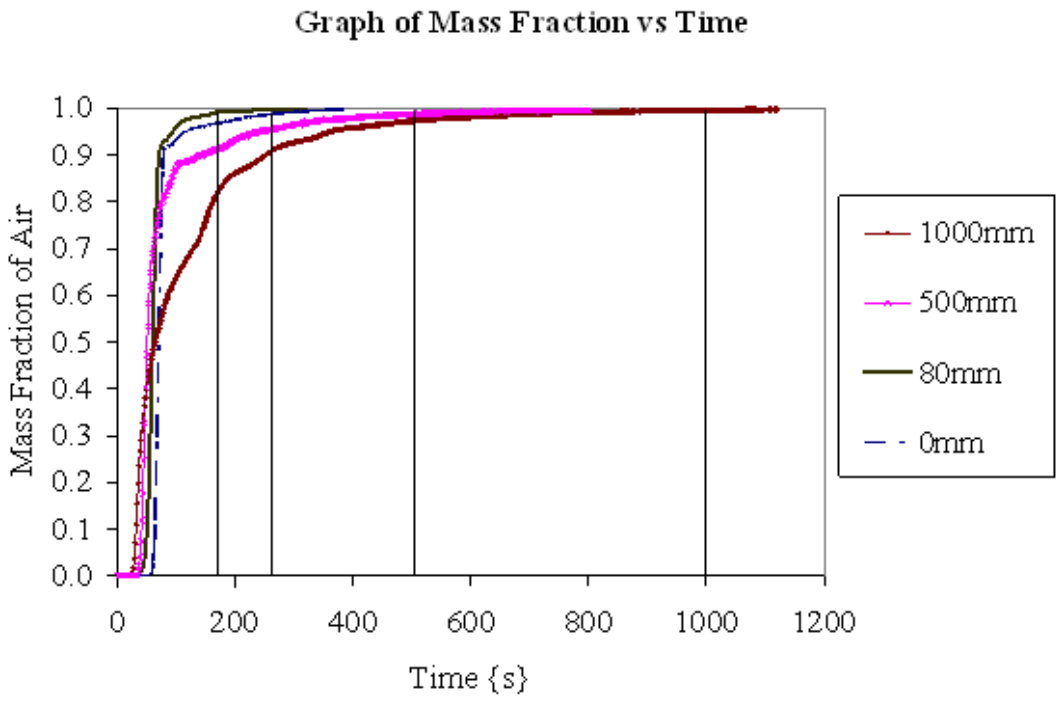

Figure 6.2: Graph of mass fraction of air against time showing the time taken to extracted pollutants at four different fan positions, i.e.; 0 mm, 80 mm, 500 mm and 1000 mm.

It can be observed from these results that optimum position should be at or near 80 mm. Then two more positions 20 mm behind and beyond 80 mm position, i.e. position 60 mm and 100 mm, were searched. These gave extraction times of 237 s and 237 s leaving position 80 mm still optimal. See figures 6.3 and 6.4.

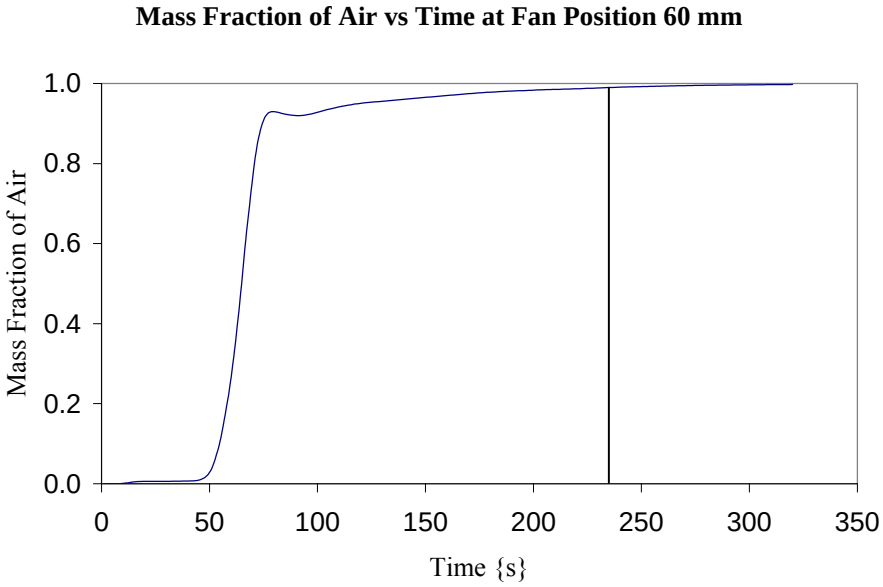

Figure 6.3: Graph of mass fraction of air against time showing that the pollutants were extracted in 237 seconds at fan position 60 mm.

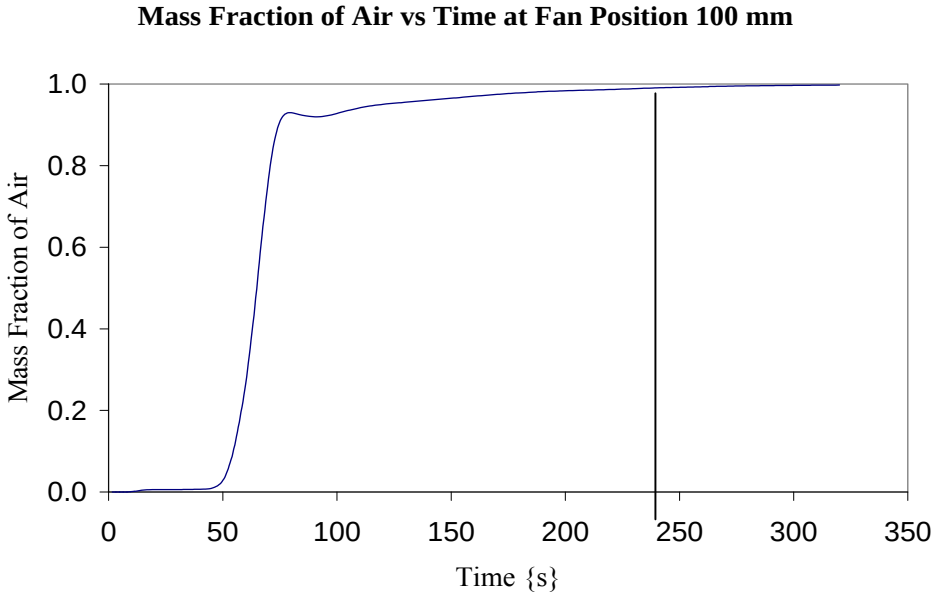

Figure 6.4: Graph of mass fraction of air against time showing that the pollutants were extracted in 237 seconds at fan position 100 mm.

Then two more positions 10 mm behind and beyond 80 mm position, i.e. position 70 mm and 90 mm, were tried. These gave extraction times of 192 s and 219 s, again leaving position 80 mm still optimal. See figures 6.5 and 6.6.

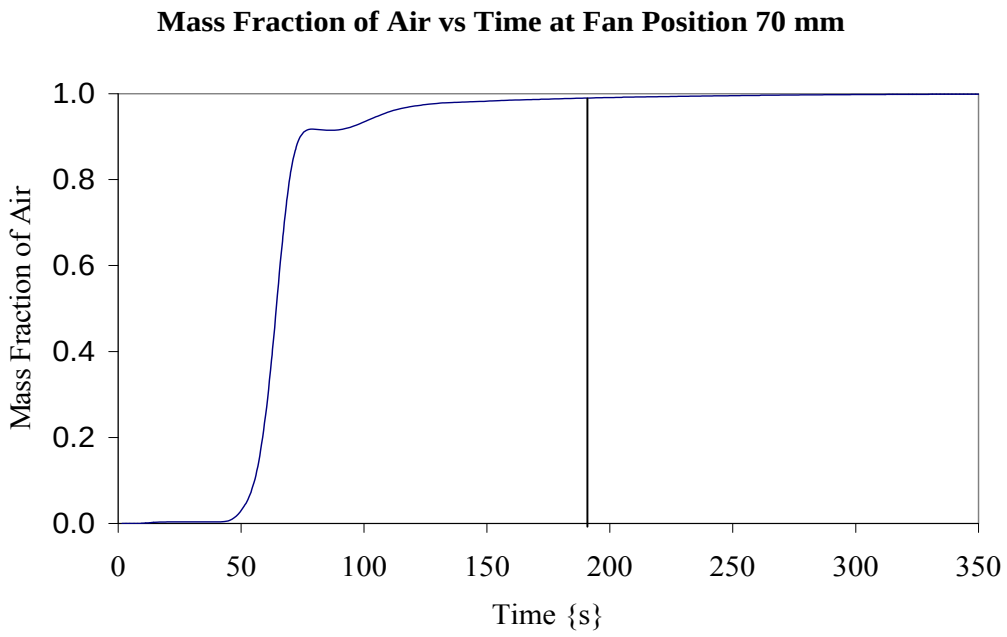

Figure 6.5: Graph of mass fraction of air against time showing that the pollutants were extracted in 192 seconds at fan position 70 mm.

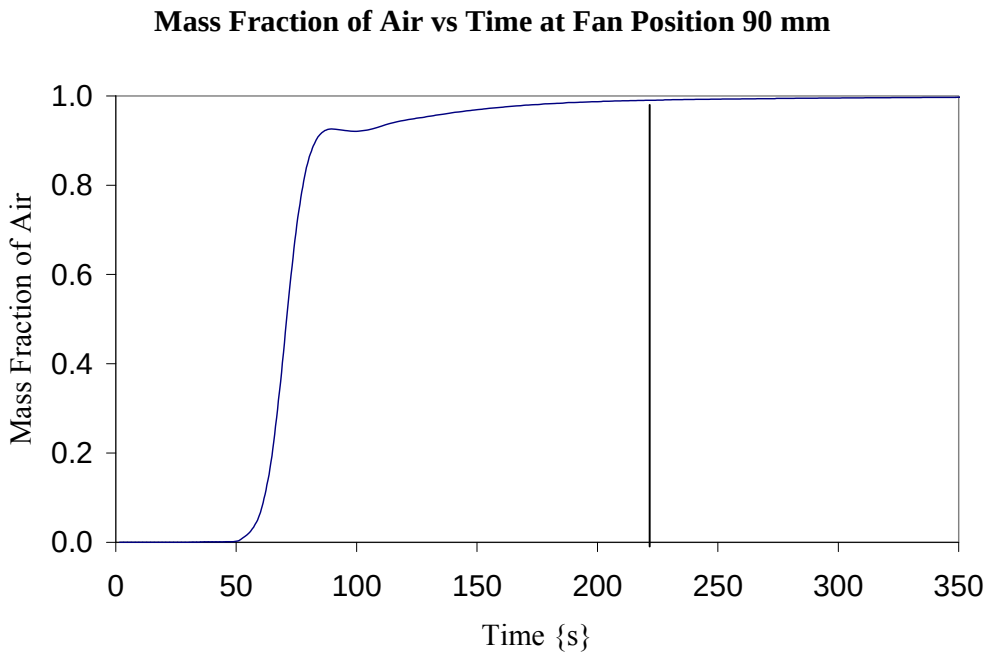

Figure 6.6: Graph of mass fraction of air against time showing that the pollutants were extracted in 219 seconds at fan position 90 mm.

Since position 70 mm have an extraction time closer to that of position 80 mm it was decided to search further between these two. Position 75 mm was tried and gave extraction time of 172 s as shown in figure 6.7.

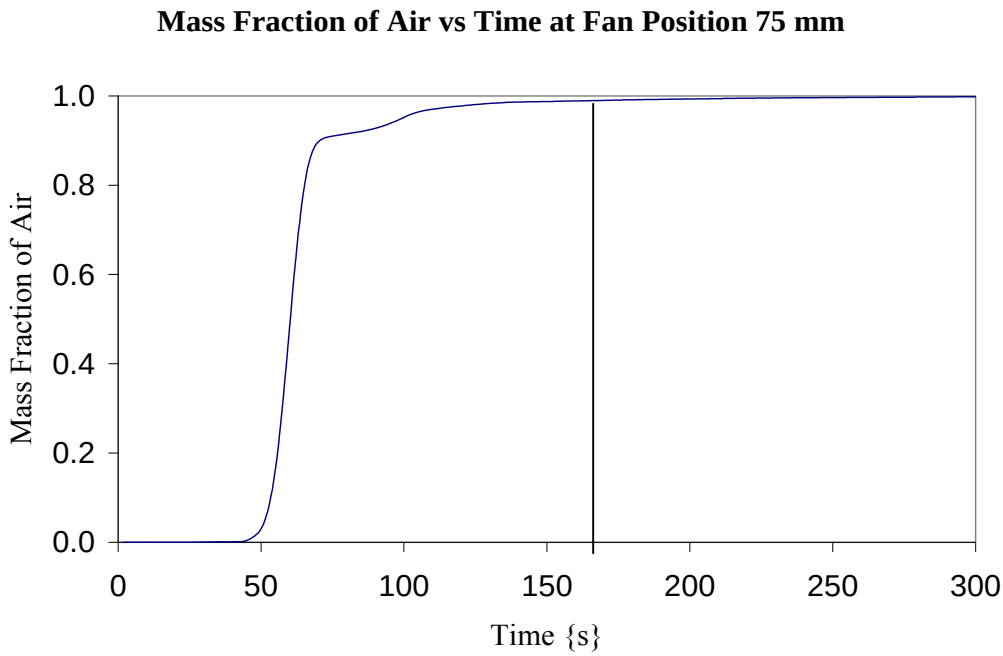

Figure 6.7: Graph of mass fraction of air against time showing that the pollutants were extracted in 172 seconds at fan position 75 mm.

Results from the searching exercise for optimum fan position in a full heading length are summarized in table 6.1 and graph of time against fan position, L_f, figure 6.8. Fan position 80 mm is an optimum position since it has the shortest extraction time than the rest.

Table 6.1: A summary of time taken to clear the heading at nine fan positions

FAN POSITION, L_f (mm)	TIME TO CLEAR THE HEADING (s)
0	224
60	237
70	192
75	170
80	165
90	219
100	237
500	547
1000	765

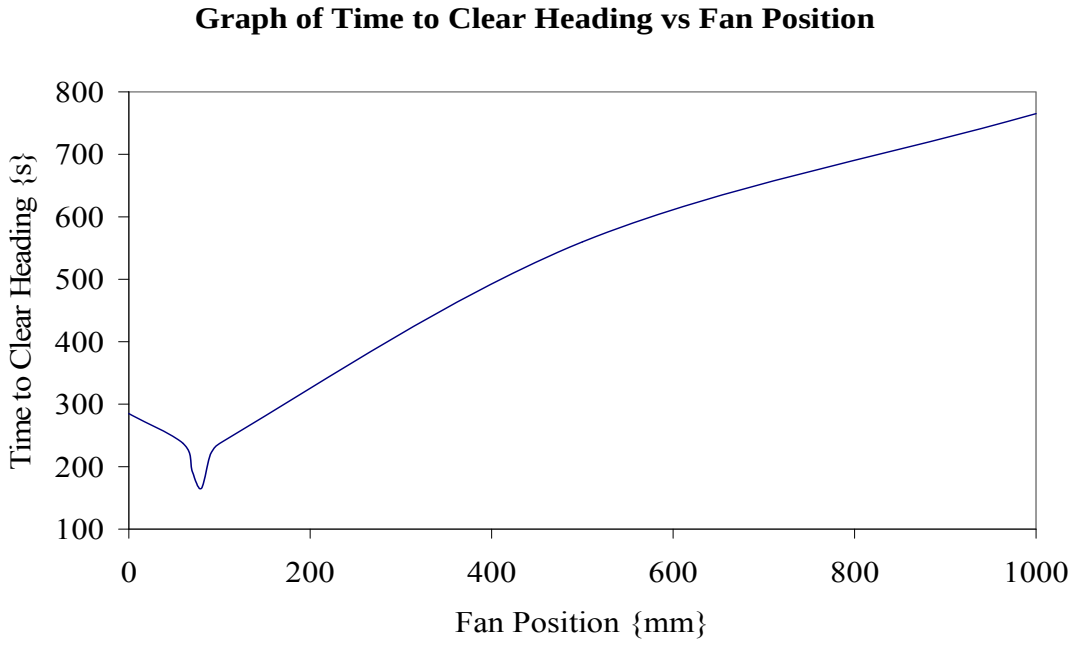

Figure 6.8: A summary of time taken to clear the heading at different fan positions along the length of the heading.

Looking at graph, figure 6.8, it is observed that when the fan is positioned right at the entrance (fan position zero) it takes a long time i.e. 285s, to clear the heading. This could be because of the through-road air flow that is passing almost directly across the fan is reducing the fan output and consequently, the penetration. See the illustration in figure 6.9a. As the fan is moved away from heading entrance into the heading the effect of this cross flow is reduced as a result the fan output and penetration increases and time taken to clear the heading is steadily reduced. This occurs up to fan position of 80mm where time to clear the heading is 165 seconds. See the illustration in figure 6.9b. From this fan position onwards time to clear the heading starts to increase. This could be because of the increased recirculation in the heading. Apart from ventilating the through-road, air flowing in the through-road also assists to draw out the pollutants out of the heading. As the fan moves deep into the heading the capacity of through-road air flow to drive the heading air away is greatly reduced. See the illustration in figure 6.9c.

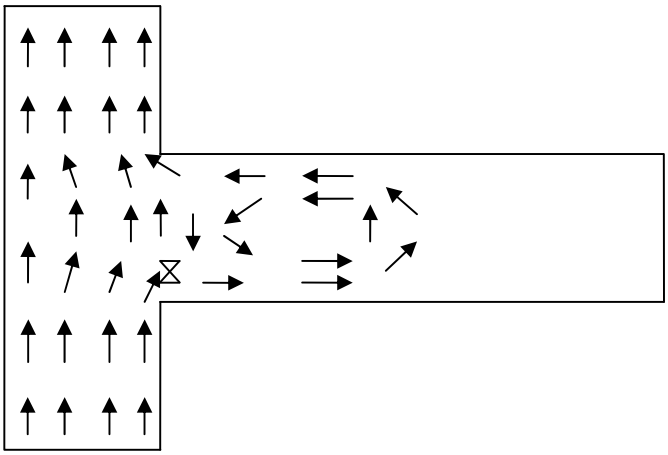

(a) Fan located at head entrance (i.e. $L_f = 0$)

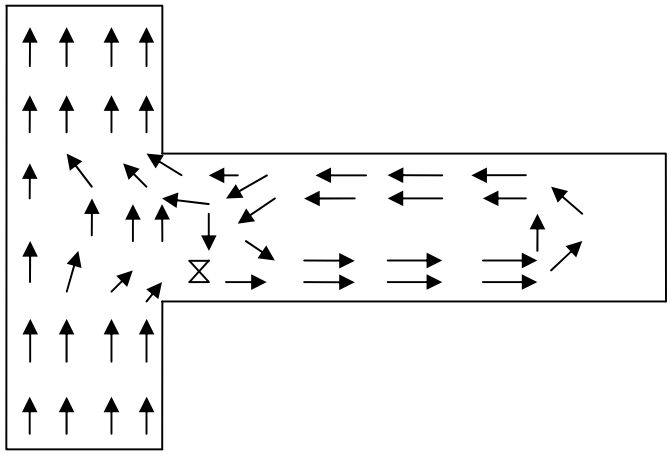

(b) Fan located at L_f = 75mm

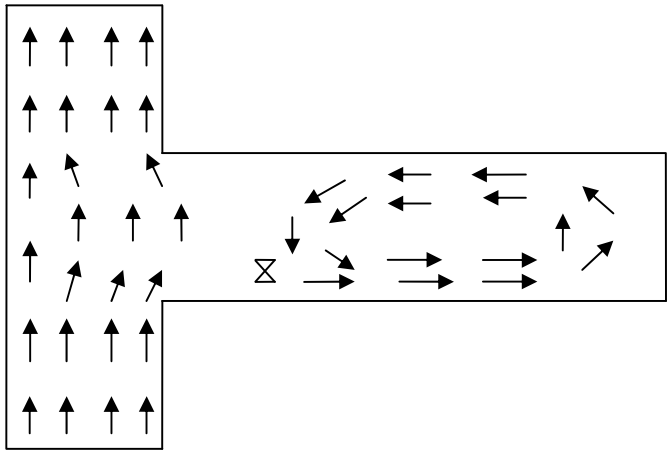

(c) Fan located at L_f = 100mm

Figure 6.9: Air patterns at three different fan position to illustrate the difference in time to completely clear out the test section.

The steps done to find the optimum position of fan in a 2333mm long heading were also followed to search for optimum position of the fan for the remaining heading lengths. Since the initial solution gave an indication of the optimum position of the fan even for the rest of mine geometries therefore the search was narrowed down in the remaining solutions. The solutions for the searching exercise for heading lengths for two different widths are given in Appendix L.

The optimum positions of the fan in the heading of scaled down model of the underground coalmine are summarized in table 6.2.

Table 6.2: Optimum fan position for five different heading lengths and two different heading widths.

Heading Length [mm]	**Fan Position in [mm] (Measured from heading entrance)**	
	Heading - 420 mm wide	**Heading – 210 mm wide**
467	15	20
933	35	50
1400	80	110
1867	70	95
2333	80	100

6.4. A Method for Determining Optimum Fan Position

Having found optimum fan position for the five heading lengths at two different widths the next step was to develop a method that can be used to determine optimum fan position for any other heading length from 467 to 2333 mm. This method is independent

from CFD. This section presents the method and describes how it was derived and finally, explains how it can be used.

6.4.1. Development of a method for determining optimum fan position

From the summarized results table a graph of optimum fan position against heading length was plotted and is shown in figure 6.10. The dimensions or quantities that are in brackets are for the real mine and are presented for relative reference purposes only.

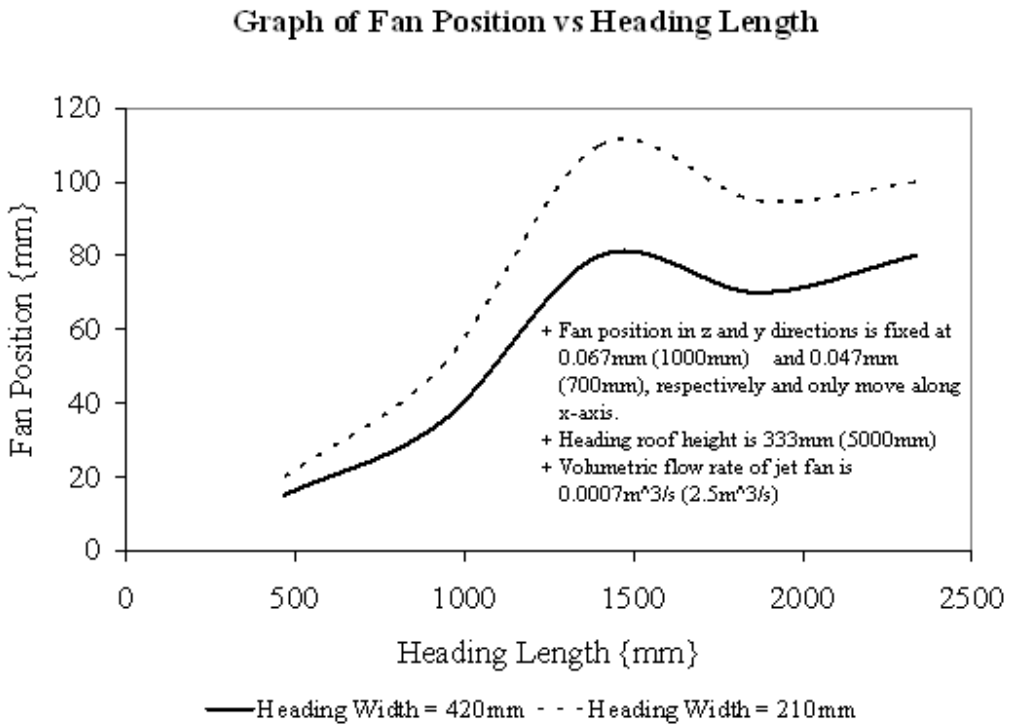

Figure 6.10: A graph for determining optimum fan position for heading lengths ranging between 467 mm to 2333 mm. The figure the brackets represent the equivalent dimensions or measurements in the actual mine.

In the graph, figure 6.10, it is observed that for a short heading length, $L_{mh,}$ the fan distance from the entrance, $L_{f,}$ is small but as L_{mh} increases L_f also increases taking a

shape similar to j-curve. This occurs between L_{mh} equal to 467mm and 1400mm. At 1400mm, L_f starts to decrease despite increasing L_{mh}. At 1867 it starts to increase again but less rapidly as it did at the beginning.

Since fan output is constant it is expected to have a constant penetration regardless of heading length. The jet fan penetration in this study is 26m which gives a scaled down equivalent of 1733 mm. Therefore one would expect a shorter heading to be cleared first and not a long heading. But it is observed in figure 6.10 that fan position for a heading length of 1400mm is greater than those of heading lengths 1867mm and 2333mm. This could be due to the effect of through-road air flow on the fan as already explained. It is also observed that the optimum fan position in half width heading shows the same trend as the full width. But the values for fan position are a bit higher. The air flowing back towards heading entrance is restricted due to narrowness of the heading, therefore increasing recirculation and time to clear the heading.

6.4.2. Determination of Optimum Position Using the Tool

Demonstration on how the tool is utilized was done using two different examples and figure 6.9 as follows:

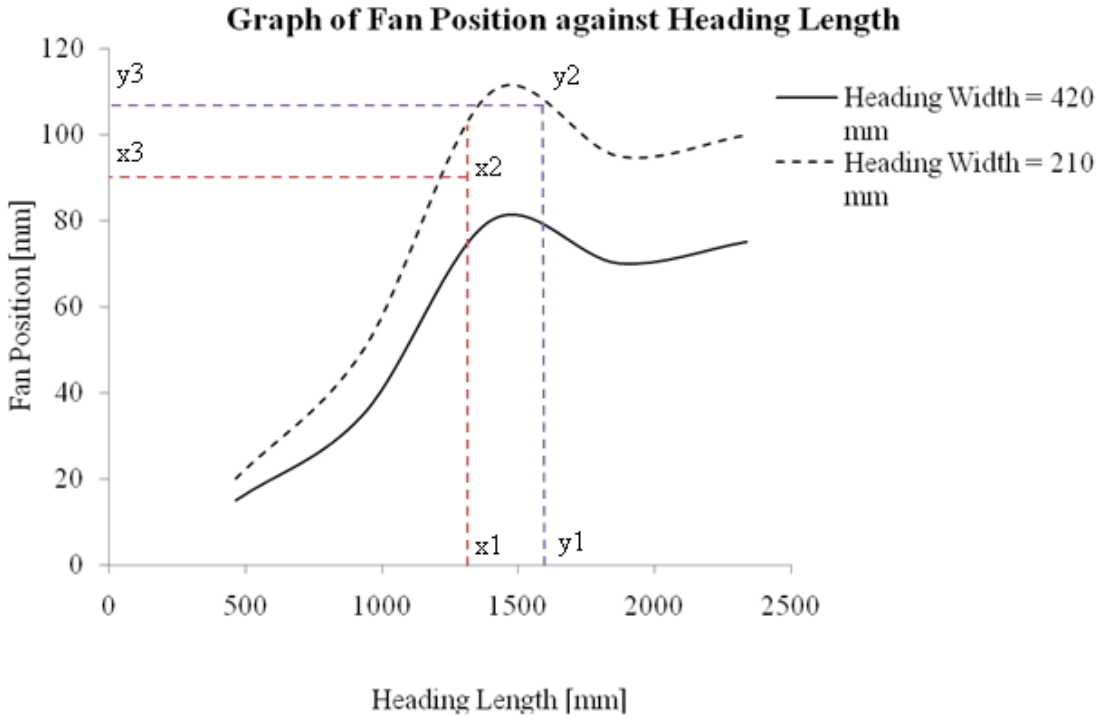

Figure 6.11: A tool for determining optimum fan position with points x and y.

Example 1

Assuming one wants to find out the optimum fan positions at heading length of y for a half width heading.

Solution for example 1

A vertical line is drawn from point y1 to intersect half width plot at y2. From y2 a horizontal line is drawn which intersects the y-axis of the graph at y3.

y3 = L_f = 90mm

But, y1 = L_{mh} = 1600mm

Therefore, the optimum fan position for heading length of 1300mm is 90mm.

Example 2

Assuming now that the heading width is 75% of full width and it is required to find the optimum fan position at heading length x1.

Solution for example 2

Like in the first example, a vertical line is drawn from point x1 to intersect half width. A midpoint between the intersections of this vertical line with full width and half width plots is a point where optimum fan position plot for a 75% full heading width is supposed to pass. This point is marked x2. A horizontal line is then drawn from x2 to intersect y-axis at x3.

x3 = L_f = 90mm

But, x1 = L_{mh} = 1300mm

And, 75% of heading width is this case is 315mm

Therefore, the optimum fan position for heading length of 1300mm and width 315mm is 90mm.

7.0 CONCLUSION AND RECOMMENDATIONS

Briefly, this investigation has highlighted that ARD and methane are main problems faced in underground coalmines. Further solutions are need and sought that can be applied to control these concentrations to the allowable levels. Ventilation techniques are popular methods currently being used for this purpose and was utilized in this study. Since it is difficult to carry out this kind of investigation in the actual mine comparatively inexpensive CFD techniques offer an alternative method. Before this technique can be used it is necessary to verify its application via experiments.

The main objective of this study was to investigate if a CFD modelling technique can reliably be used to obtain dust and mine gas concentrations in underground coalmine. Due to practical limitation, CFD modelling for a scaled down underground coalmine model was verified instead and it is believed that the same idea can be extended to the actual coalmine.

In the investigation the flow of air was first examined in a steady state condition by CFD modelling and experimentation on the scaled down mine model. The air flow patterns of results from the two models were similar. Then the unsteady state condition examination for the two models was also done to investigate the dilution of mine gas. Like in the steady state, this also produced similar results as the experimental investigation. Minor variations did exist as explained in chapter 5. The similarity in both steady and unsteady state results of the two models means that the CFD modelling technique could be relied on for further analysis.

After verification of CFD models further numerical analysis was done with an objective of finding optimum jet fan positions for different heading lengths and widths. The information found in the analysis was then used to create a graph for determining optimum fan position for different heading lengths and widths of the scaled down model. It was observed that for a short heading length, the fan distance from the entrance was

small but as heading length was increased fan distance also increased taking a shape similar to j-curve. This occurred between heading lengths 467mm and 1400mm. At 1400mm, fan distance started to decrease despite increasing heading length. At 1867 it starts to increase again but less rapidly as it did at the beginning. This could be de to the effects of through-road air flow on the jet fan and nature of air flow recirculation in the heading.

During the execution of this investigation, a number of applicable study fields related to this topic were identified. These are beyond the scope of this investigation. They are as following:

Although the results of the scaled down model appears convincing the size might compromise the results of the actual mine. Therefore is necessary to carry out a similar study on a full scale model rather than just concluding that the model analysis can work on the actual mine.

In this study the author was not able to explain why the optimum fan positions for different heading lengths changed in the manner as depicted in the graphs, figure 6.10. A study can be carried out in order to find out why the graphs behave this way.

This study has proved that CFD modelling can be used to optimize fan position in the scaled down coalmine model therefore it is possible to extend it to other mine ventilation and related studies, air conditioning for example.

REFERRENCES

[1] BELLE B K. 2002. *Dust Control for Thick-seam Wall Mines*. CSIR – Miningtek, South Africa.

[2] GODDARRD B, BOWER K and MITCHELL D. 1973. *Control of Harmful Dust in Coal Mines.* National Coal Board. London.

[3] PENG S S and CHIANG H S. 1984. *Longwall Mining*. A Wiley – Interscience Publication, Inc. IDBN 0-471-86881-7.

[4] *Increased Underground Extraction of Coal*. 1982. Publication of the South African Institute of Mining and Metallurgy monograph series No 4. Johannesburg. ISBN 0 620 06028 X.

[5] STEFANKO R. 1983. Coal Mining Technology: Theory and Practice. Society of Mining Engineers of The American Institute of Mining, Metallurgical and Petroleum Engineers. New York.

[6] CLARK J, CALDON J H, CURTH E A. 1982. Thin Seam Coal Mining Technology Noyes Data Corporation. New Jersey.

[7] Joy Mining Machinery Brochure. Bulletin No. CM33-4M-1100. A Joy Global Company. (Electronic copy).

[8] BOXHO J. 1980. *Firedamp Drainage – Handbook for the Coal Mining Industry in the European Community*. Verlag Gluckauf. GMBH. Essen. Pp. 23 -55.

REFERRENCES

[9] FLINT J D. 1990. Mine Gas and Coal Dust Explosions and Methane Outbursts – Their Causes and Prevention. Dissertation. University of Witwatersrand, Johannesburg. Pp 3 – 8.

[10] Department of Minerals and Energy, www.dme.gov.za.

[11] KISSELL F N. 2003. *Handbook for Dust Control in Mining*. U.S. Department of Health and Human Services. Pittsburgh, PA.

[12] SZLAZAK, N., SZLAZAK, J., TOR, A., OBRACAJ, D., AND BOROWSKI, M., 2003, *Ventilation Systems in Dead-end Headings with Coal Dust and Methane Hazard*. 30th International Conference of Safety in Mines Research Institutes. South African Institute of Mining and Metallurgy. Pp 673 – 688.

[13] MARX W and BELLE B K., *Simulating Airflow Conditions In a South African Coal Mine, Using The VUMA-Network Simulation Software*. (Paper). CSIR-Miningtek, Johannesburg, South Africa.

[14] DU PLESSIS J J and BELLE B K. *Kloppersbos Health and Safety Research in the South Africa Coal Industry*. CSIR Division of Mining Technology, South Africa.

[15] WHITE Frank M. 2006. *Viscous Fluid Flow*. Third Edition. Mc Graw Hill Inc., Singapore. ISBN 007-124493-X. Chapters 1,2 and 3.

[16] FLETCHER C A J. 1991. *Computational Techniques for Fluid Dynamics*. Second Edition. Springer-Verlag. Berlin Heidelberg. ISBN 3-540-53058-4 2.

REFERRENCES

[17] LOMAX Harvard, PULLIAN H. Thomas and ZINGG W. David. 1999. *Fundamentals of Computational Fluid Dynamics*. Electronic version.

[18] PATANKAR S V. 1980. *Numerical Heat Transfer and Fluid Flow*. Hemisphere Publishing Corporation. ISBN 0-89116-522-3.

[19] LEUTLOFF D, SRIVASTAVA R C et al. 1995. *Computational Fluid Dynamics,* Springer. Pp 13 – 25.

[20] Guide Notes for Star CCM+ version 3.02.006.

[21] VERSTEEG H K., MALALASEKERA W. 2007. An Introduction to Computational Fluid Dynamics-The Finite Volume Method. Second Edition. Prentice Hall.

[22] POTTER M C., WIGGERT D C. 2002. *Mechanics of Fluids.* Third Edition. Brooks/Cole product, USA. ISBN 0-534-37996-6.

[23] MUNSON B R., YOUNG D F., OKIISHI T H. 2006. *Fundamentals of Fluid Mechanics.* Fifth Edition. John Wiley and Sons, Inc. USA. ISBN 0-471-67582-2.

[24] SHAMES I H. 1992. *Mechanics of Fluids.* Third Edition. Singapore. ISBN 0-07-112815-8.

[25] DALING A A. 2007. Scale Model Investigation of Air Flow Patterns In Coalmines. Fourth Year Thesis. Mechanical Engineering Department. University of Pretoria. (Unpublished remarks and discussion)

REFERRENCES

[26] PRINSLOO T. 2008. Investigation for the Optimisation of Air Flow Patterns in Coalmines. Fourth Year Thesis. Mechanical Engineering Department. University of Pretoria. (Unpublished remarks and discussion)

[27] Every et al. RICHARD L. E, Warrington, PA United States Patent 4, 043, 395. Aug-23, 1977.

[28] BECKWITH TG., MARANGINI RD., LIENHARD JH. 1995. *Mechanical Measurements*. Fifth Edition. Addison-Wesley Publishing Company. ISNB 0-201-56947-7.

[29] www.wikipedia.org/wiki/calibration. 2009/09/08

APPENDICES

Appendix A

DUST RISK ASSESSMENT IN UNDERGROUND COALMINE

The following risk-ranking model (Australian Standards 3931: 1988) as shown in figure A1 was used for the risk assessment. Table A1 and A2 show the probability and consequence categories that were used for evaluation purposes.

CONSEQUENCE	PROBABILITY				
	A	B	C	D	E
1	1	2	4	7	11
2	3	5	8	12	15
3	6	9	13	16	18
4	10	14	17	19	20

Figure A1: Risk Ranking Model (Source: AS 3931: 1988)

For the dust explosion (acute) safety hazard, the risk equals the probability of a dust explosion multiplied by the consequence value (damage and injury costs). For the health (chronic) hazard, the risk is equal to the time-integrated exposure multiplied by the 'dose response'. Exposure equals average concentration multiplied by time exposed (for example, mg/m³ of respirable dust times years of work). Therefore, reducing the

probability or consequence value can reduce the acute dust explosion hazard risk, and reducing the concentration or time can reduce the chronic health hazard risk. With the available data and expert opinion the risk assessment for thick seam wall mining was derived and is summarized in table A3.

Table A1: Probability category for the risk ranking model

Probability category	**Definition**
A	Possibility of repeated incidents
B	Isolated incidents known to have occurred
C	Possibility of occurring some time
D	Unlikely to occur
E	Practically impossible

Table A1: Consequence category for the risk ranking model

Consequence category	Definition
1	Serious long or short-term health effects that may be fatal
2	Serious adverse health effects that would require off-site medical treatment
3	Non-life-threatening health effects that may require on site first aid and treatment
4	Little if any adverse health effects

Table A3: Assessment for thick-seam wall mining

Risk category	Risk rank	Colour
Explosion risk	2	Red
Health risk	1	Red

Appendix B

South African Coalmine Explosion Fatality Records [8]

Data presented in appendix B shows explosion fatalities in South Africa coalmines due methane and combination of methane and coal dust in 100 years (1891 – 1990). The records show the nature of explosion at a particular colliery, number of deaths involved and the year in which the accident occurred.

Date	**Colliery**	**Nature of Explosion**	**Fatalities**
Natal			
1891	Elandslaagte	Methane	1
1897	Elandslaagte	Methane	3
	Natal Navigation	Methane	0
1898	Natal Navigation	Methane	2
	Campbell	Methane	0
	St. George	Methane	0
1899	St. George	Methane	4
	South Africa	Methane	2
	South Africa	Methane	0
	Natal Navigation	Methane	0
1901	New Campbell	Methane	31
1902	Glencoe	Methane	0
	Glencoe	Methane	0
	Crown	Methane	0
1903	St. George	Methane	2

	Ramsay	Methane	0
	South Africa	Methane	2
1904	Ramsay	Methane	1
	Elandslaagte	Methane	0
1905	Crown	Methane	0
	Glencoe	Methane	1
	Glencoe	Methane	0
	Newcastle Stream	Methane	0
	Dundee Coal	Methane	1
	South Africa	Methane	0
	South Africa	Methane	1
1906	Elandslaagte	Methane	18
	Elandslaagte	Methane	1
1907	Ramsay	Methane	1
1908	Glencoe	Methane/Coal Dust	77
	Cambrian	Methane/Coal Dust	0
	Ramsay	Methane	1
1909	South Africa	Methane	1
1910	Cambrian	Methane	0
1911	Utrecht	Methane	0
1912	Natal Navigation	Methane	0
1914	South Africa	Methane	1
1915	Hlobane	Methane	1
	Hattingspruit	Methane	1
1918	Hlobane	Methane	0
	Northfield	Methane	0
1919	Durban Navigation No 2	Methane	1
	Northfield	Methane	0
1921	Northfield	Methane	1

	Hlobane	Methane	1
	Bannockburn	Methane	0
	Burnside	Methane	6
1922	Utrecht	Methane	0
	Burnside	Methane	20
	Natal Navigation	Methane	0
1923	Hlobane	Methane	12
1926	Burnside	Methane	1
	Durban Navigation No 2	Methane/Coal Dust	125
1928	New Tendege	Methane	1
	Tshoba	Methane	0
1930	Burnside	Methane	38
1937	Utrecht	Methane	0
1941	Utrecht	Methane	15
1943	Northfield	Methane/Coal Dust	78
1944	Tshoba	Methane	0
	Hlobane No 1	Methane	57
1945	Tshoba	Methane	0
1948	Cambrian	Methane	0
1949	Utrecht	Methane	0
1951	Durban Navigation No 2	Methane	9
	Northfield	Methane	3
1952	Hlobane No 2	Methane/Coal Dust	0
	Hlobane No 2	Methane/Coal Dust	1
1953	Northfield	Methane	5
1954	Newcatle-Platberg	Methane	1
1955	Carnavon Anthracite	Methane	1
1956	Cambrian	Methane	2
1960	Durban Navigation No 3	Methane	0

1961	Elandslaagte Antracite	Methane	0
	Natal Coal Exploration	Methane	0
1962	Ingagane	Methane	0
	Northfield	Methane	10
	Enyati	Methane	1
1965	Hlobane No 1	Methane/Coal Dust	0
	Indumeni	Methane	0
	Durban Navigation	Methane	0
	Kilbarchan	Methane	0
	Newcastle Platberg	Methane	0
1966	Kilbarchan	Methane	0
	Indumeni	Methane	0
	Natal Coal Exploration	Methane	0
1967	Indumeni	Methane	0
	Indumeni	Methane	0
	Kilbarchan	Methane	0
	Indumeni	Methane	3
1968	Natal Coal Exploration	Methane	0
	Kilbarchan	Methane	0
	Indumeni	Methane	0
	Durban Navigation	Methane	0
	Enyati	Methane	3
	Utrecht	Methane	0
1969	Northfield	Methane	0
1970	Durban Navigation	Methane	0
1971	H.C.J. Contractors	Methane	28
1972	Newcastle Platberg	Methane	0
1974	Durban Navigation	Methane	0
1975	Durban Navigation	Methane	0

1976	Durban Navigation	Methane	2
1977	Durban Navigation	Methane	0
	Durban Navigation	Methane	0
1978	Newcastle Platberg	Methane	0
1979	Newcastle Platberg	Methane	0
	Balgray	Methane	1
	Durban Navigation	Methane	0
1980	Durban Navigation	Methane	0
	Balgray	Methane	0
1981	Balgray	Methane	0
	Durban Navigation	Methane	0
	Newcastle Platberg	Methane	10
	Balgray	Methane	0
	Newcastle Platberg	Methane	0
	Durban Navigation	Methane	0
	Balgray	Methane	0
1982	Durban Navigation	Methane	1
1984	Durban Navigation	Methane	0
	Durban Navigation	Methane	0

Transvaal and Orange Free State

1935	Consolidated Marsfield	Methane/Coal Dust	95
1936	South Rand Exploration	Methane	0
1941	Consolidated Collieries	Methane	0
1943	Consolidated Marsfield	Methane	0
1944	Consolidated Collieries	Methane	0
1945	Landau/Navigation	Methane	10
1947	Consolidated Collieries	Methane	1

1951	Cornelia	Methane	11
1956	Schoongezicht	Methane	8
1957	Springfield	Methane	8
1960	Schoongezicht	Methane	0
1961	Coalbrook	Methane	7
1962	Springfield	Methane	1
1972	Usutu	Methane	0
1974	Albion	Methane	13
1976	Usutu	Methane	0
1977	Usutu	Methane	1
1980	Ermelo Mines	Methane	0
	Coalbrook	Methane	0
1981	Ermelo Mines	Methane	0
	Ermelo Mines	Methane	2
	Springfield	Methane	2
1982	Bosjespruit	Methane	0
	Springfield	Methane	0
	Ermelo Mines	Methane	11
1983	Springfield	Methane	0
	Springfield	Methane	0
	Ermelo Mines	Methane	1
1984	Ermelo Mines	Methane	6
1985	Middlebult	Methane/Coal Dust	30
	Springfield	Methane	2
	Springfield	Methane	0
	Springfield	Methane	0
1990	Ermelo Mines	Methane	0

Appendix C

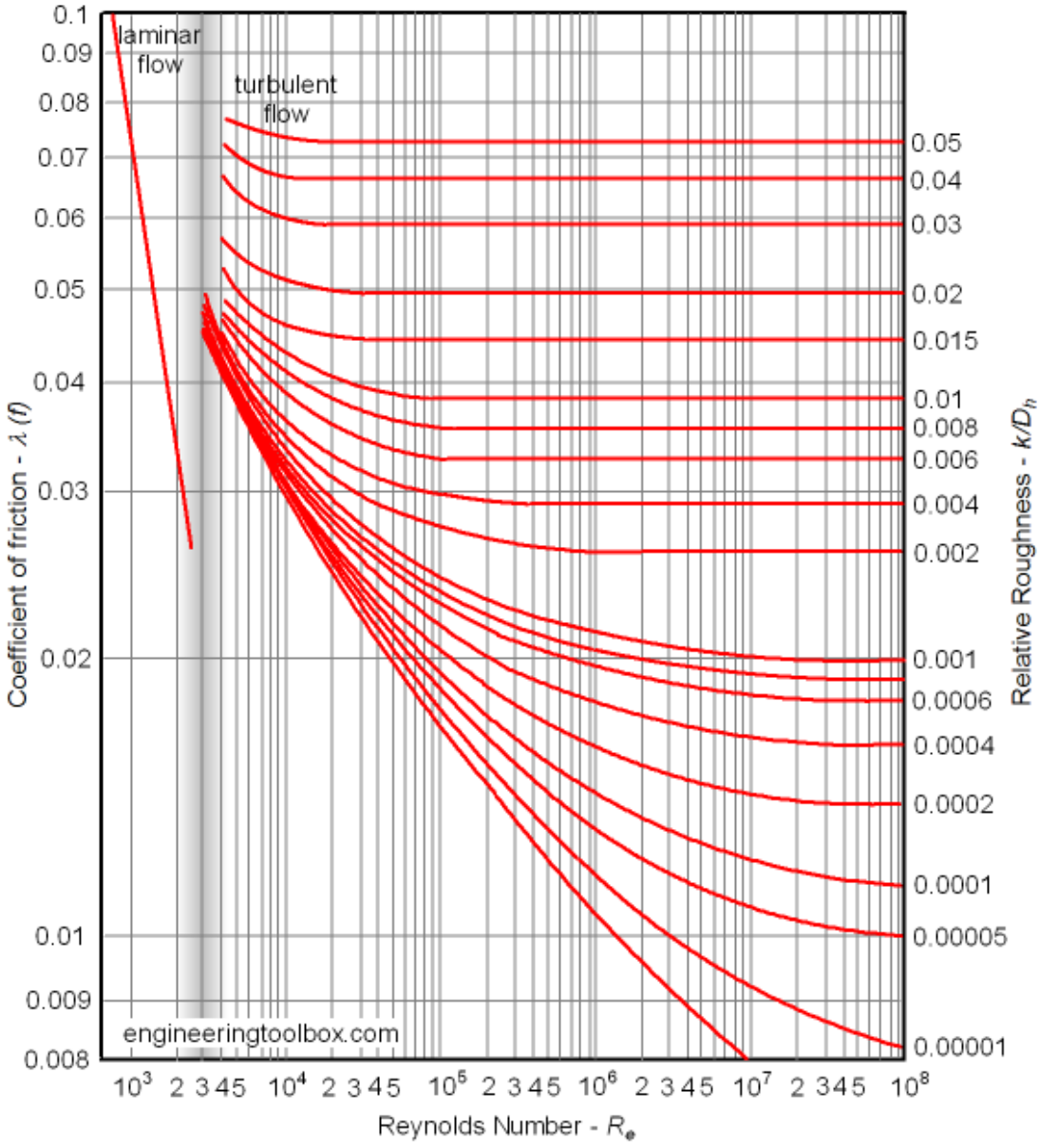
laminar flow
turbulent flow
Coefficient of friction - λ (f)
Relative Roughness - k/D_h
Reynolds Number - R_e
engineeringtoolbox.com
0.1
0.09
0.08
0.07
0.06
0.05
0.04
0.03
0.02
0.01
0.009
0.008
0.05
0.04
0.03
0.02
0.015
0.01
0.008
0.006
0.004
0.002
0.001
0.0006
0.0004
0.0002
0.0001
0.00005
0.00001
10^3 2 3 4 5 10^4 2 3 4 5 10^5 2 3 4 5 10^6 2 3 4 5 10^7 2 3 4 5 10^8

Appendix D

Properties of Water [22]

Temperature (^{0}C)	Density ρ, (kg/m^3)	Specific weight γ, (N/m^3)	Viscosity μ, (Ns/m^2) $\times 10^{-3}$	Kinematic Viscosity υ, (m^2/s) $\times 10^{-6}$
0	999.9	9809	1.792	1.792
5	1000.0	9810	1.519	1.519
10	999.7	9807	1.308	1.308
15	999.1	9801	1.140	1.141
20	998.2	9792	1.005	1.007
30	995.7	9768	0.801	0.804
40	992.2	9733	0.656	0.661
50	988.1	9693	0.549	0.556
60	983.2	9645	0.469	0.477
70	977.8	9592	0.406	0.415
80	971.8	9533	0.357	0.367
90	965.3	9470	0.317	0.328
100	958.4	9402	0.284	0.296

Properties of Air at Atmospheric Pressure [22]

Temperature (^{0}C)	Density ρ, (kg/m^3)	Viscosity μ, (Ns/m^2) $\times 10^{-5}$	Kinematic Viscosity υ, (m^2/s) $\times 10^{-5}$
-30	1.452	1.56	1.08
-20	1.394	1.61	1.16
-10	1.342	1.67	1.24
0	1.292	1.72	1.33
10	1.247	1.76	1.42
20	1.204	1.81	1.51
30	1.164	1.86	1.60
40	1.127	1.91	1.69
50	1.092	1.95	1.79
60	1.060	2.00	1.89
70	1.030	2.05	1.99
80	1.000	2.09	2.09
90	0.973	2.13	2.19
100	0.946	2.17	2.30

Appendix E

Calculations for pressure drop in a pipe with an orifice whose results are indicated in section 3.2.3.6.

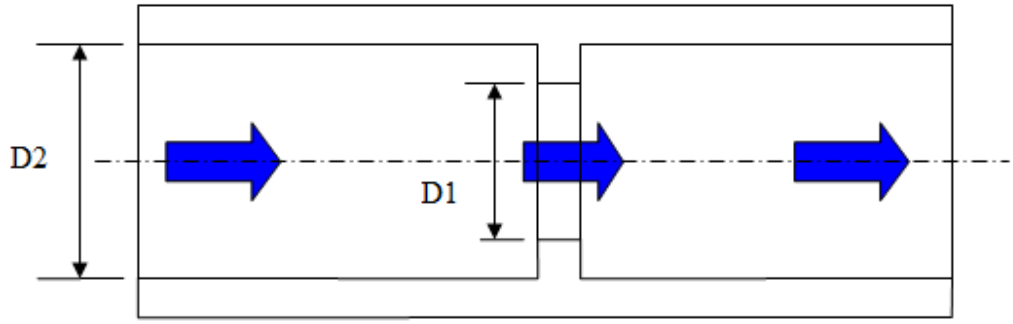

Water flows in a pipe with an orifice as shown in the figure above. From the details given below find the pressure drop between the inlet and outlet.

Internal diameter, D2	0.100 m
Orifice diameter, D1	0.071 m
Length	2.000 m
Inlet velocity	1.000 m/s
Temperature	20^0C

Material for the pipe is glass therefore the surface is smooth.

Solution

Pressure drop, ΔP = $(h_i + h_o + h_e)\ \rho g$

Where subscripts i, o and e stand for inlet, orifice and exit, respectively.

Head loss, h = $f(LV\text{^}2)/(2gD)$, equation 3.5.

To extract friction factor, f from Moody diagram (appendix D), Reynolds number and relative roughness values must be found first.

Re_i = $\frac{1 \times 0.1}{1.007E-6}$, equation 3.3.

= 1.0E5

This Re shows that the flow is turbulent.

Relative roughness, e/D is approximately zero for a smooth surface.

Therefore, the value of friction factor from Moody diagram is

f = 0.0158

Therefore, h_i = 0.00805 m

And ΔP_i = **79 Pa**

h_e = 0.00725 m (taking into consideration of developed flow)

And ΔP_e = **71 Pa**

h_o = 0.1092 m, equation 3.19.

And ΔP_o = **1 069 Pa**

Therefore, **total pressure drop = 1 219 Pa**

Appendix F

The readings for the eight sensors at different input voltage values and their best lines of fit that were used to adjust experimental measured values are as follows:

Sensor 1

Voltage (V)	Readings (kohm)	Average of all sensors (kohm)	Deviation (kohm)
220	126.130	210.249	84.119
225	118.389	197.812	79.423
230	112.194	185.878	73.684
235	105.880	173.940	68.061
240	102.254	167.224	64.969
245	98.416	160.146	61.731
250	93.951	151.964	58.013

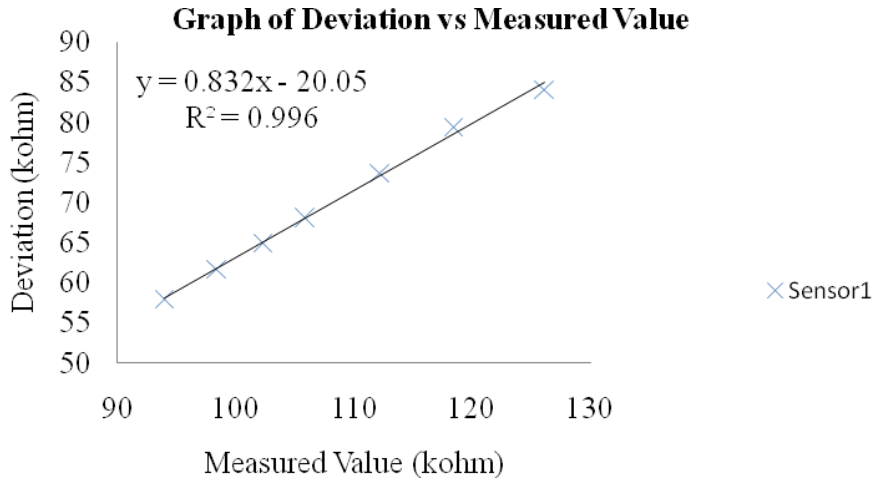

Sensor 2

Voltage (V)	Readings (kohm)	Average of all sensors (kohm)	Deviation (kohm)
220	317.901	210.249	107.652
225	298.391	197.812	100.579
230	282.777	185.878	96.8992
235	266.862	173.94	92.9216
240	257.725	167.224	90.5008
245	248.05	160.146	87.9035
250	236.798	151.964	84.8336

Graph of Deviation against Measured Value

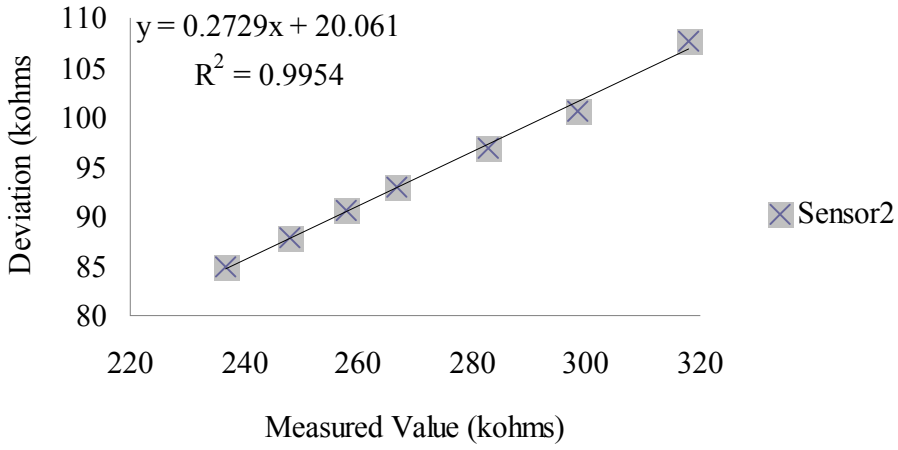

Sensor 3

Voltage (V)	Readings (kohm)	Average of all sensors (kohm)	Deviation (kohm)
220	341.616	210.249	131.367
225	317.005	197.812	119.193
230	298.576	185.878	112.698
235	280.026	173.94	106.086
240	269.544	167.224	102.32
245	258.412	160.146	98.2658
250	245.653	151.964	93.6886

Graph of Deviation against Measured Value

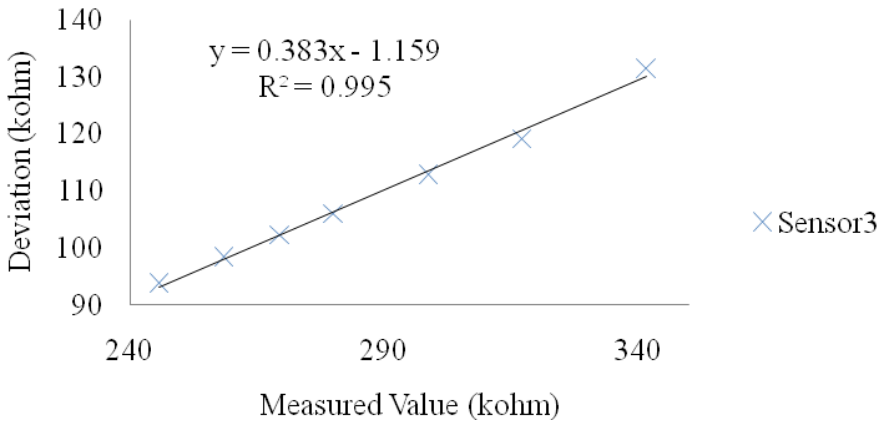

Sensor 4

Voltage (V)	Readings (kohm)	Average of all sensors (kohm)	Deviation (kohm)
220	162.604	210.249	47.645
225	152.744	197.812	45.0687
230	143.864	185.878	42.0141
235	134.926	173.94	39.0146
240	129.875	167.224	37.3486
245	124.512	160.146	35.6349
250	118.364	151.964	33.6004

Graph of Deviation against Measured Value

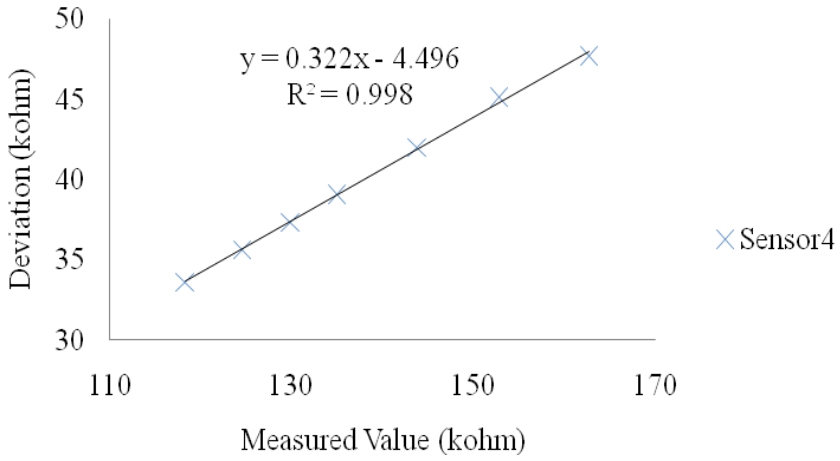

Sensor 5

Voltage (V)	Readings (kohm)	Average of all sensors (kohm)	Deviation (kohm)
220	110.724	210.249	99.525
225	102.747	197.812	95.0651
230	96.7741	185.878	89.104
235	90.7616	173.94	83.1788
240	87.3641	167.224	79.8596
245	83.7562	160.146	76.3903
250	79.6205	151.964	72.3434

Graph of Deviation against Measured Value

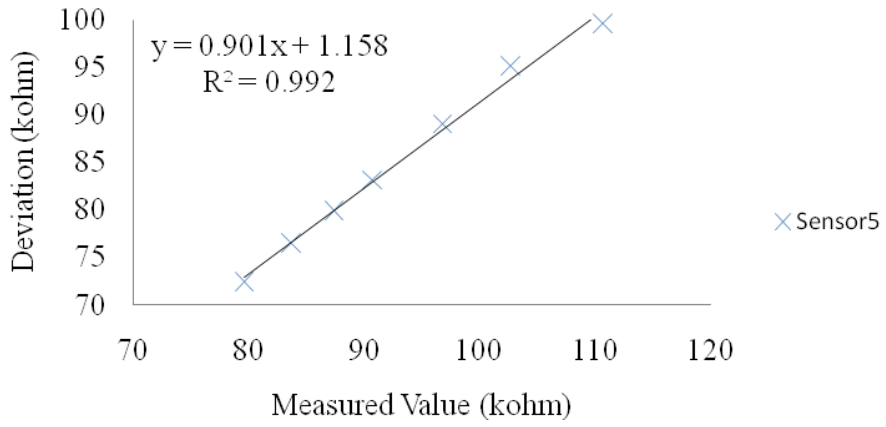

Sensor 6

Voltage (V)	Readings (kohm)	Average of all sensors (kohm)	Deviation (kohm)
220	383.385	210.249	173.136
225	348.727	197.812	150.915
230	323.559	185.878	137.681
235	298.937	173.94	124.996
240	285.388	167.224	118.164
245	271.29	160.146	111.144
250	254.932	151.964	102.968

Graph of Deviation against Measured Value

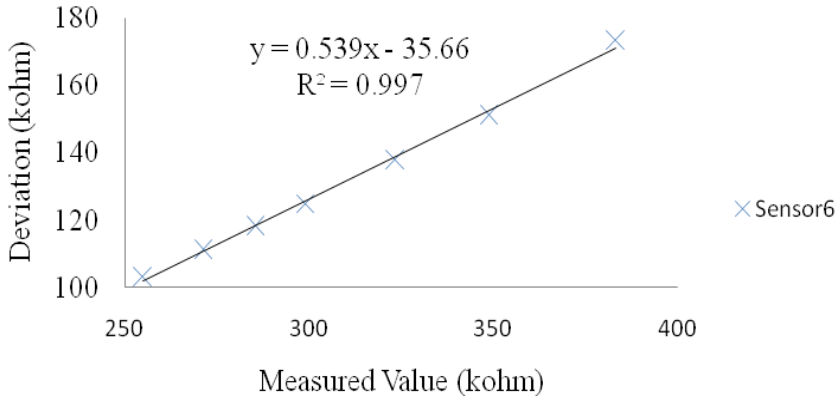

Sensor 7

Voltage (V)	Readings (kohm)	Average of all sensors (kohm)	Deviation (kohm)
220	132.168	210.249	78.081
225	122.039	197.812	75.7729
230	113.232	185.878	72.6463
235	104.615	173.94	69.3255
240	99.8734	167.224	67.3503
245	94.9398	160.146	65.2067
250	89.215	151.964	62.7489

Graph of Deviation against Measured Value

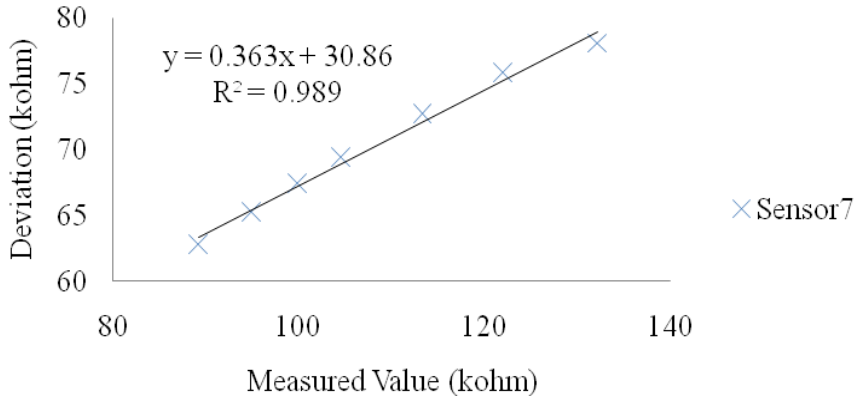

Sensor 8

Voltage (V)	Readings (kohm)	Average of all sensors (kohm)	Deviation (kohm)
220	130.463	210.249	79.786
225	122.456	197.812	75.3566
230	116.048	185.878	69.8301
235	109.517	173.94	64.4238
240	105.767	167.224	61.457
245	101.796	160.146	58.3501
250	97.1785	151.964	54.7854

Graph of Deviation against Measured Value

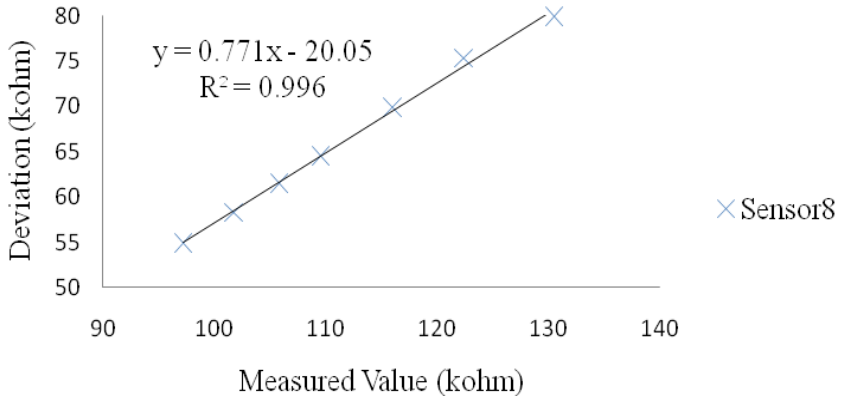

Appendix G

This appendix shows vector diagram developed from video images of MG-1 and MG-2 as seen from the top at levels 1, 2 and 3 and as seen from the side at planes 1 to 6. The dots are the positions where the smoke enters the test section from the tubes, the arrows indicate flow direction that were definite and circles around the dots indicate that the flow direction could not be determined at all and a circle and an arrow indicate that despite the smoke circulating it was flowing to a particular direction most of the time. Failure to determine flow direction at particular point was a result of continuous change of smoke direction during the whole period of observation in other words there was no dominant direction of flow.

MG-1 AS SEEN FROM THE TOP

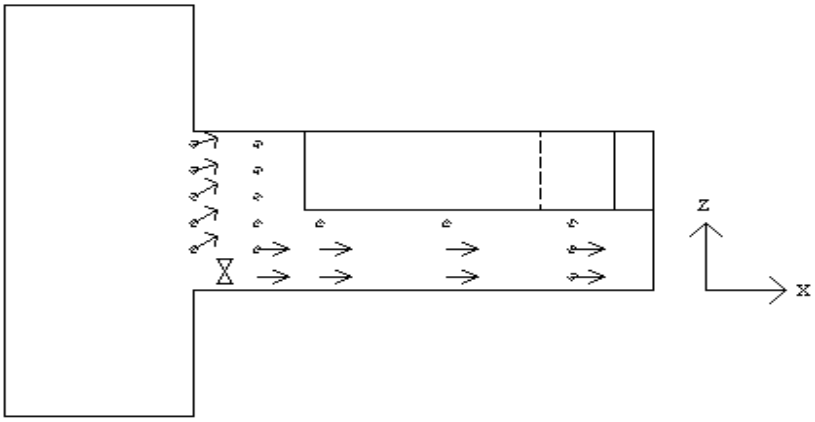

Level 1

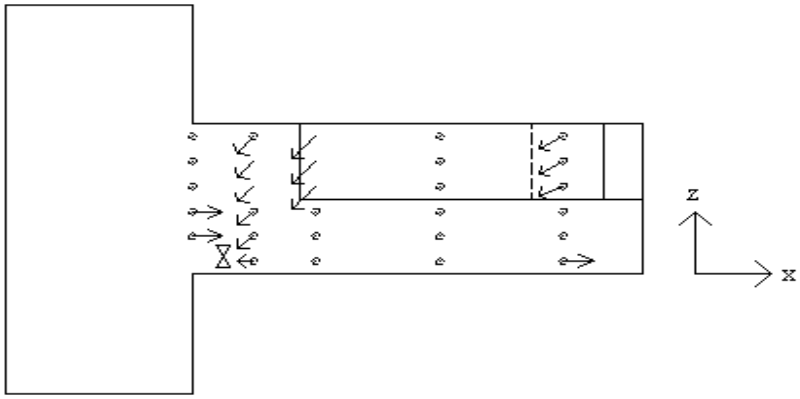

Level 2

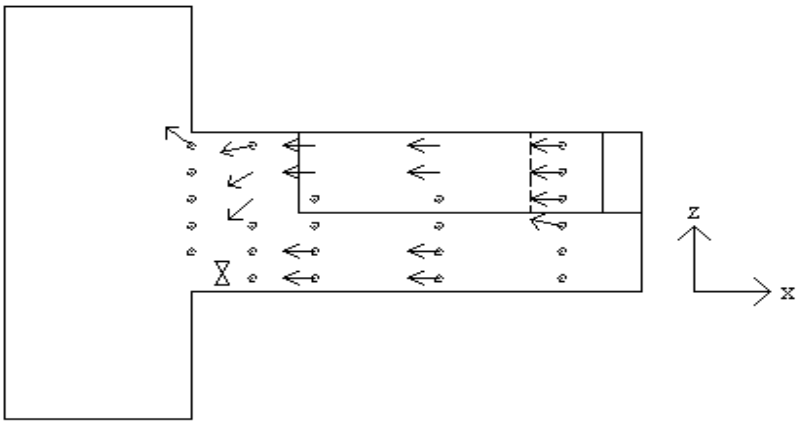

Level 3

MG-1 AS SEEN FROM THE SIDE

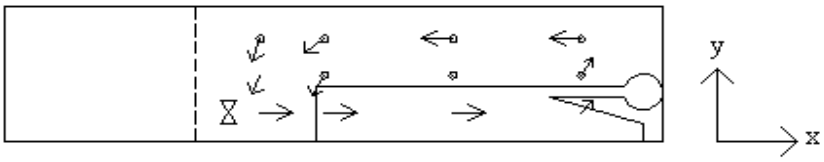

Section 1

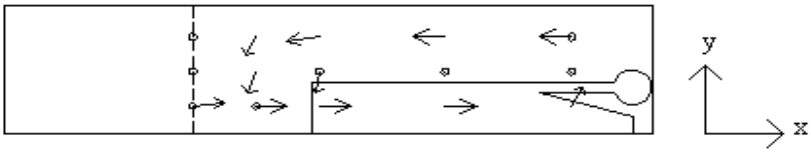

Section 2

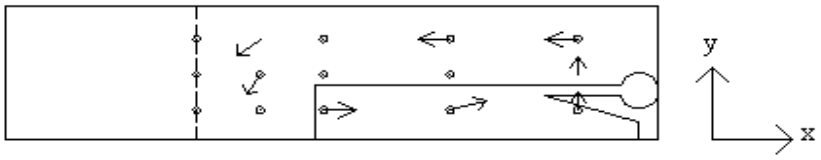

Section 3

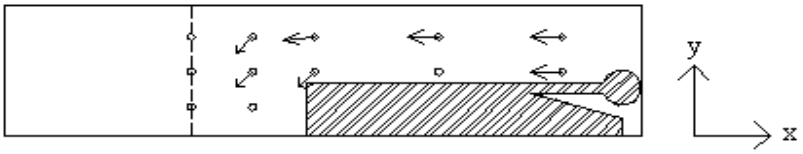

Section 4

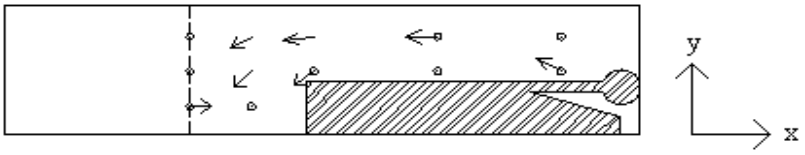

Section 5

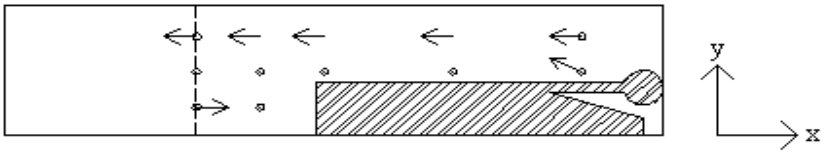

Section 6

MG-2 AS SEEN FROM THE TOP

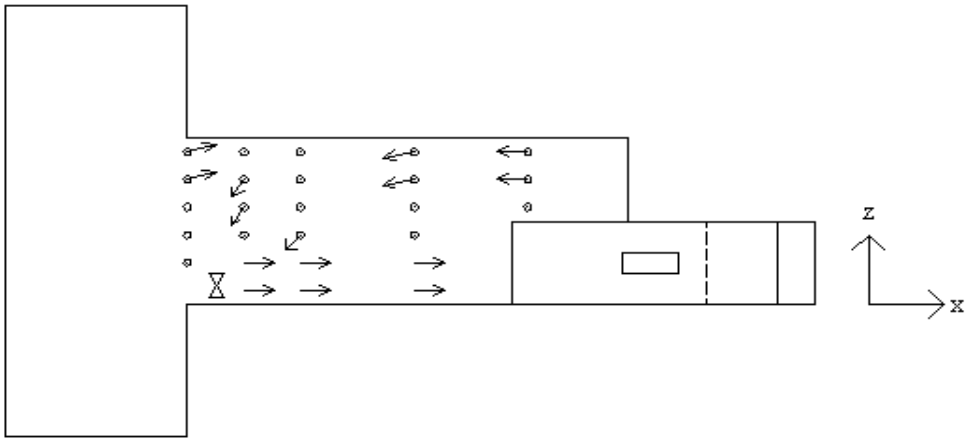

MG2 Level 1

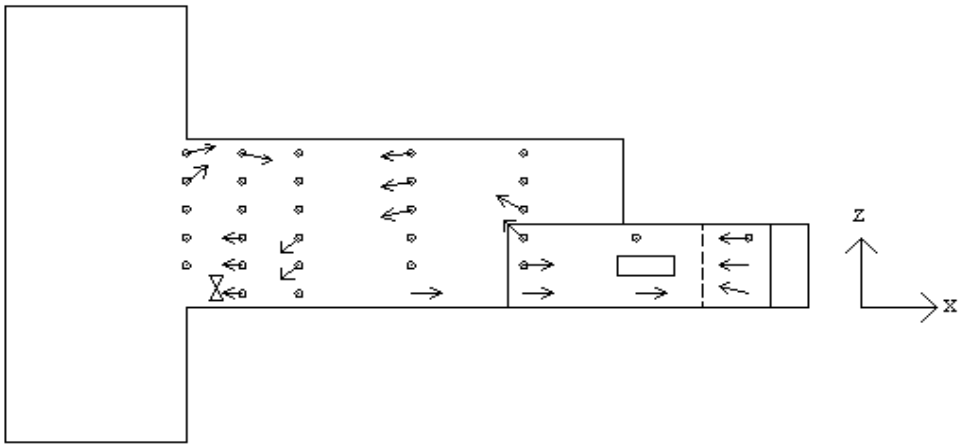

MG2 Level 2

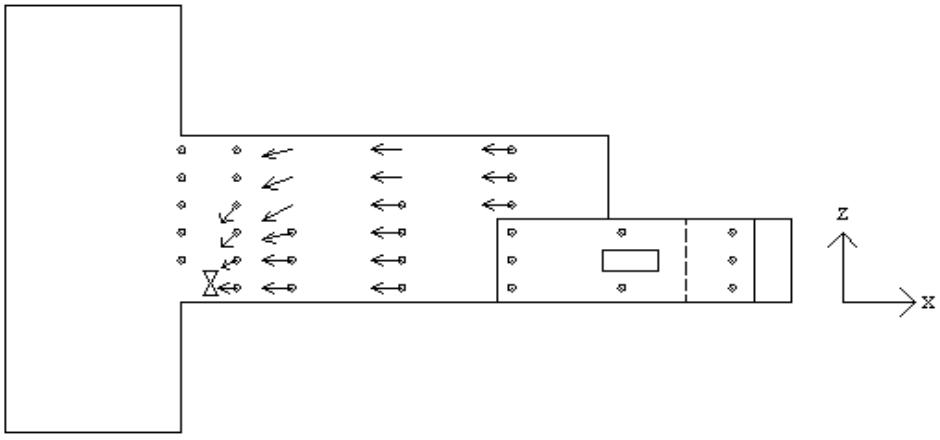

MG2 Level 3

MG-2 AS SEEN FROM THE SIDE

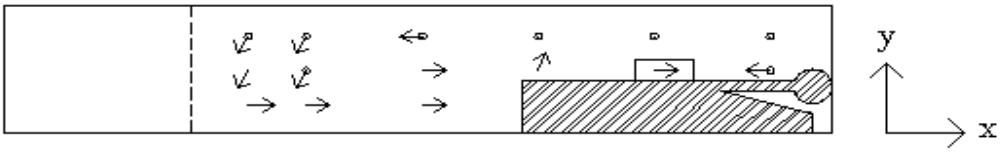

Section 1

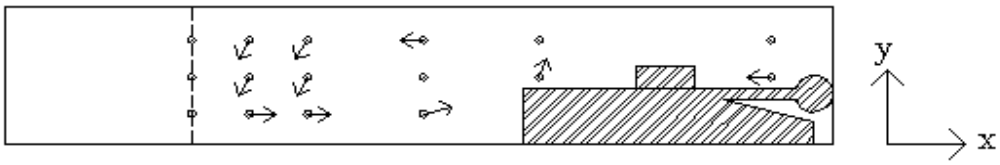

Section 2

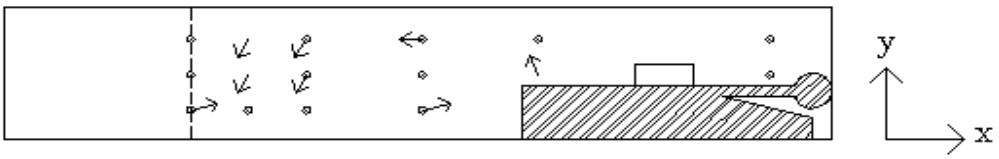

Section 3

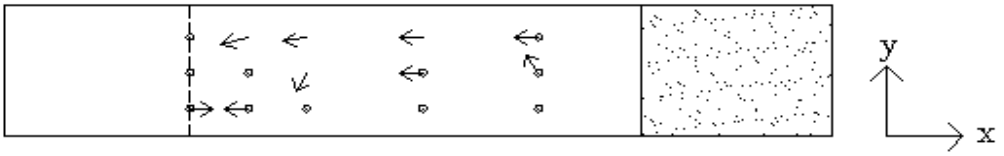

Section 4

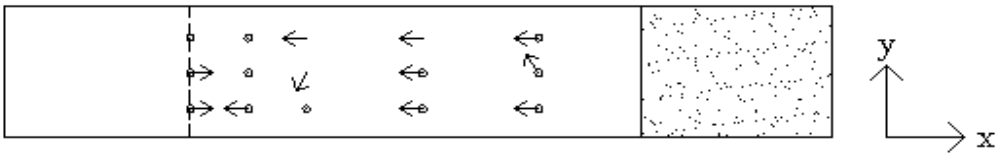

Section 5

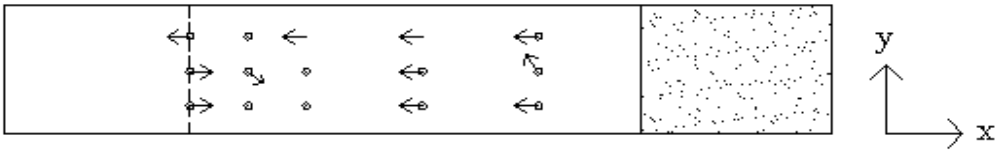

Section 6

Appendix H

The resistance values measured in unsteady state experiment done on a scaled down model of the underground coalmine. Channels 101 to 108 represent sensors 1 to 8.

		101	102	103	104	105	106	107	108
	Channel	Channel	Channel	Channel	Channel	Channel	Channel	Channel	Channel
Scan Number	Unit	OHM	OHM	OHM	OHM	OHM	OHM	OHM	OHM
1	09/03/2009 14:59:48:079	284116.9	314572.3	343321.8	314900.7	258364.7	388782.1	263507.9	255558.1
2	09/03/2009 14:59:56:169	284186.5	314444.7	343964.5	315429.8	257985.1	388677.8	263792	255645.8
3	09/03/2009 15:00:04:259	284025.6	314991.8	343305.2	315657.7	258067.3	387210.6	263052.1	255585.8
4	09/03/2009 15:00:12:349	284365.9	314487.9	345149.9	315613.3	257924.1	387933	263200.1	255419.4
5	09/03/2009 15:00:20:439	284194.2	315366.9	344329.6	315456.8	257897.4	387582.3	263353.6	255205.2
6	09/03/2009 15:00:28:530	283967.9	315440.2	344187.6	315057.3	258343.6	388358.1	263523.1	255227.6
7	09/03/2009 15:00:36:620	282875.7	313815.3	343328.5	315158.2	258440.1	389178.3	263381.9	255550.4
8	09/03/2009 15:00:44:710	284225.3	314063.9	342589.3	315444.4	257970.7	390156.4	262998.4	255494.9
9	09/03/2009 15:00:52:800	284280.8	315020.7	344800.2	315043.9	258297	389224.4	263337.6	255458.3
10	09/03/2009 15:01:00:890	284276.4	315808.7	345459.5	315471.3	258491.2	388920.8	263122.7	255216.3
11	09/03/2009 15:01:08:980	280380.7	315338.1	337114.3	313631.1	255319.2	377030.7	256164.9	253858.6
12	09/03/2009 15:01:17:071	280473.9	315078.4	337103.2	328590.3	265437	389831.8	267150.7	253796.4
13	09/03/2009 15:01:25:161	291712.8	326366	371228.2	329136.4	266666.8	437801.1	266742.3	253403.5
14	09/03/2009 15:01:33:251	291115.6	326024.2	367192.6	327895.5	264864.3	422246	266111.8	253323.6
15	09/03/2009 15:01:41:341	290591.8	325933.2	371361.4	327498.1	264717.8	438104.2	265883.2	252824.2

16	09/03/2009 15:01:49:431	290389.8	325717.9	361512.1	328326.1	263306	406855.9	264256.1	264844.4
17	09/03/2009 15:01:57:522	290924.7	326184	371425.7	327185.1	264655.7	429065.2	265485.9	265323.9
18	09/03/2009 15:02:05:612	290960.3	325318.3	365472.2	327933.2	265474.8	436719.1	266009.7	265505.9
19	09/03/2009 15:02:13:702	289956.9	325757.8	361538.7	326612.4	264593.5	428272.7	264633.5	265878.8
20	09/03/2009 15:02:21:792	290556.3	326379.4	372236	326319.4	263974.2	432525.9	265874.3	265126.3
21	09/03/2009 15:02:29:882	287666.1	323602.4	350186.7	323948.7	261912	396278.6	263505.8	267086.4
22	09/03/2009 15:02:37:972	288525.1	324199.5	351929.2	324326	262193.9	393665.9	263223.9	261445.9
23	09/03/2009 15:02:46:062	287885.8	323513.6	348839.3	324758.9	261969.7	404327.6	264977.5	260336
24	09/03/2009 15:02:54:153	291743.8	324872.1	361494.4	327107.5	262902	412434.3	265197.3	261714.5
25	09/03/2009 15:03:02:243	288740.5	323760	357212.4	326814.4	261752.2	430199.5	266038.6	261492.5
26	09/03/2009 15:03:10:333	290116.7	325520.3	363587.6	327644.6	256189.3	381909.8	265632.4	261794.4
27	09/03/2009 15:03:18:423	289837	326175.1	347172.2	324938.7	255132.7	372537.8	264928.7	262433.7
28	09/03/2009 15:03:26:513	282001.6	312475	338087.4	313860.4	255534.2	378199.5	262053.6	255442.5
29	09/03/2009 15:03:34:603	281877.8	311235.3	336462.6	313690.6	255689.3	379909.8	262647.4	255744.4
30	09/03/2009 15:03:42:693	281598.1	311190.1	335047.2	313384.7	255132.7	380537.8	261943.7	255383.7
31	09/03/2009 15:03:50:783	276762.4	312210.8	334600.2	312748.4	252622.1	379458.2	261743.9	255286
32	09/03/2009 15:03:58:873	274018.7	306739	334342.4	311116.8	251272.5	379237	262275.6	255664.5
33	09/03/2009 15:04:06:962	272320.6	305359.4	334701.8	311150	249790.7	378376.7	261736.1	254850.1
34	09/03/2009 15:04:15:072	272049.7	304428.2	332914.5	311089.8	244909.5	366457.8	261945.9	255522.4
35	09/03/2009 15:04:23:163	272911	303517.5	331503.3	311121.2	245782.9	365958.4	261889.6	255372.5
36	09/03/2009 15:04:31:254	271201.8	302044.1	328268.4	311112.2	244599.8	356053.6	261820.7	255141.7
37	09/03/2009 15:04:39:365	265929.8	299568.4	324829.9	311451.7	242590.9	355545.3	261461.3	255069.1
38	09/03/2009 15:04:47:475	264258.2	299047	320848.6	310071.5	239787.3	349784.9	261301.8	254787.6
39	09/03/2009 15:04:55:606	263663.4	299817.3	316916.4	309987.3	238832.7	351025.8	261236.6	253957.5
40	09/03/2009 15:05:03:736	263124	296831.6	313564.5	308805.2	236689.5	344366.4	260813.8	253193.8

41	09/03/2009 15:05:11:602	262039.9	296028.1	312669.9	307928.4	235774.9	337691.5	260359.8	253466.9
42	09/03/2009 15:05:19:526	261293.7	293794.9	311886.3	306192.5	235461.8	339238.7	259210.5	252900.8
43	09/03/2009 15:05:27:392	260167.7	292594	308305.8	305062.6	234332.2	337283	256151.7	249899.6
44	09/03/2009 15:05:35:023	258468.2	292394.3	307266.9	305320.1	234290.4	329664.7	255897.6	249564.5
45	09/03/2009 15:05:42:655	258021.1	286323.1	304163.6	303315.7	234169.7	330812.3	253783.3	246452.3
46	09/03/2009 15:05:50:288	257862.8	286596.1	302358.9	303504.3	233079.6	315386.9	251436.8	243297
47	09/03/2009 15:05:57:921	257110	275608.1	288696.1	286762.6	233058.3	310949.5	251152.6	241964.9
48	09/03/2009 15:06:05:554	256755.4	275398.3	287326.5	284600.5	233030.8	311002	251150.4	238952.6
49	09/03/2009 15:06:13:186	256483.3	275492.1	285899.1	284838.1	233673.1	312660.1	250399	239118
50	09/03/2009 15:06:20:818	256347.5	275224.1	288924.7	285654.9	233923.9	318690.1	249987.2	238000.4
51	09/03/2009 15:06:28:450	256461.4	276045.4	287923.6	287224.3	234411.6	320956.5	249754.1	238358.9
52	09/03/2009 15:06:36:082	258289.3	278243	289779.3	287055.6	235009.4	322943.2	250631.8	237514.2
53	09/03/2009 15:06:43:715	260754.4	281341.9	293344.3	288223.2	236132.6	323431.5	250845.7	238655.2
54	09/03/2009 15:06:51:367	260886.4	282434	291874.8	289193.3	236936.2	325997.6	251425.4	238977.1
55	09/03/2009 15:06:58:999	262535.7	282249.8	294072.4	290660.6	240043.9	327857.7	252488.9	243445.5
56	09/03/2009 15:07:06:631	262038.5	283279.8	297994.8	291195.6	240562.6	331751.3	252785.3	244573.2
57	09/03/2009 15:07:14:263	262419.2	285017.9	298070.3	291663.9	241445.3	334399.5	253754.2	246018.3
58	09/03/2009 15:07:21:896	263250.5	285524	301546.5	293588.5	241736.1	337567.1	254375.8	245847.3
59	09/03/2009 15:07:29:840	263499.1	286665	301513.2	292958.1	243498.6	342133.3	255368	247958.4
60	09/03/2009 15:07:37:990	264995.3	289106.7	304731.9	294736.1	242124.7	342637.2	255112.7	247478.9
61	09/03/2009 15:07:46:121	265226.1	289373.1	305448.9	296205.6	243354.5	345482.9	255272.6	248110.5
62	09/03/2009 15:07:54:251	265881	291659.5	306461.1	297162.4	244498.8	347929.2	256533.4	249254.7
63	09/03/2009 15:08:02:382	267849.9	294028	308567.7	298805	245199.1	350195.6	256897.5	249431.9
64	09/03/2009 15:08:10:492	269017.6	295615.2	310716.5	301229	248111.5	353283.3	258489.1	249546.1
65	09/03/2009 15:08:18:603	270686.8	297340	313131.6	302382.3	248325.7	357008.1	259543.5	249365.4

66	09/03/2009 15:08:26:693	270626.9	297788.4	314774.3	302656.4	248567.4	356792.8	259395.8	249833.5
67	09/03/2009 15:08:34:783	270451.5	298108	315833.1	302830.6	248948.6	356767.1	259361.5	250342.4
68	09/03/2009 15:08:42:873	270567.6	298534.2	316943	303072	249414.5	357725.1	259571.2	250470.6
69	09/03/2009 15:08:50:963	271004.5	299397.7	320203.9	303504.3	250038.3	358808.4	259232.7	250801.9
70	09/03/2009 15:08:59:053	271767.9	301320.1	321815.5	305049.3	250888.5	359973.8	259402.5	250656.1
71	09/03/2009 15:09:07:143	273266.2	303084.8	322288.3	305739.7	251518.9	362206.9	259479.4	250278.1
72	09/03/2009 15:09:15:233	273843.4	303133.6	324195.1	306450	252833	364320.2	260187.2	250758.5
73	09/03/2009 15:09:23:323	274651.4	304174.7	325618	307648.7	252915.1	365379	260217.9	250859.3
74	09/03/2009 15:09:31:413	275348.4	305304.6	327642.4	308270.2	253738.7	366961.7	259885.3	250798.6
75	09/03/2009 15:09:39:503	274911.1	305535.5	327333.9	309688.7	253571.1	367012.8	260091.7	250657.6
76	09/03/2009 15:09:47:593	275834.6	305695.3	327928.8	309502.2	254324.7	367119.3	259752.1	250810.2
77	09/03/2009 15:09:55:683	275359.5	306177	327416	309436.7	253809.7	367101.6	260191.2	250910.7
78	09/03/2009 15:10:03:773	275916.7	306523.3	328692.4	309680.9	254088.4	368639.9	260162.8	251146.7
79	09/03/2009 15:10:11:863	275807.9	307049.4	329227.4	309764.9	254150.8	368821.9	260183.2	250959.8
80	09/03/2009 15:10:19:953	275813.4	306191.4	326590.2	309313.5	253962.9	368440.1	260158.7	251078.3
81	09/03/2009 15:10:28:043	275637	306145.9	327926.6	309815.2	253591.1	366875.1	260189.1	250504.5
82	09/03/2009 15:10:36:133	275751.3	306748.6	327438.2	309262.5	254339.1	367445.6	260173.2	250836.1
83	09/03/2009 15:10:44:224	275788.5	307622.1	330761.2	309316.9	254520.1	370258.1	259890.9	251202.3
84	09/03/2009 15:10:52:314	275830.8	307584.3	329953.2	309799.7	254510.7	369563.3	260138.4	251371.3
85	09/03/2009 15:11:00:405	275574.9	308485.6	331769	310495.6	254651.1	370020.7	260221	250799.7
86	09/03/2009 15:11:08:495	275637.1	308525.5	332408.3	310568.9	254671.3	370108.3	260280.9	251274.7
87	09/03/2009 15:11:16:585	275900.4	309158.2	332805.7	310133.8	254703	370060.6	260310.9	251424.5
88	09/03/2009 15:11:24:674	276210.8	308443.4	330983.2	309420.1	254348	370992.9	260405.6	251026.4
89	09/03/2009 15:11:32:764	276829.7	308061.6	331498.2	309555.9	254638.6	369878.5	260481.3	250713.1
90	09/03/2009 15:11:40:855	276294.1	307992.8	331342.8	309356.9	254679.2	370779.8	260436.6	251284.5

Appendix J

A graph of resistance against time plotted from the raw data. In this graph the effects of switching on and off of heating element can clearly be seen in all the plots. The effect on plot for sensor 6 has been illustrated; point A being switch on and B switch off.

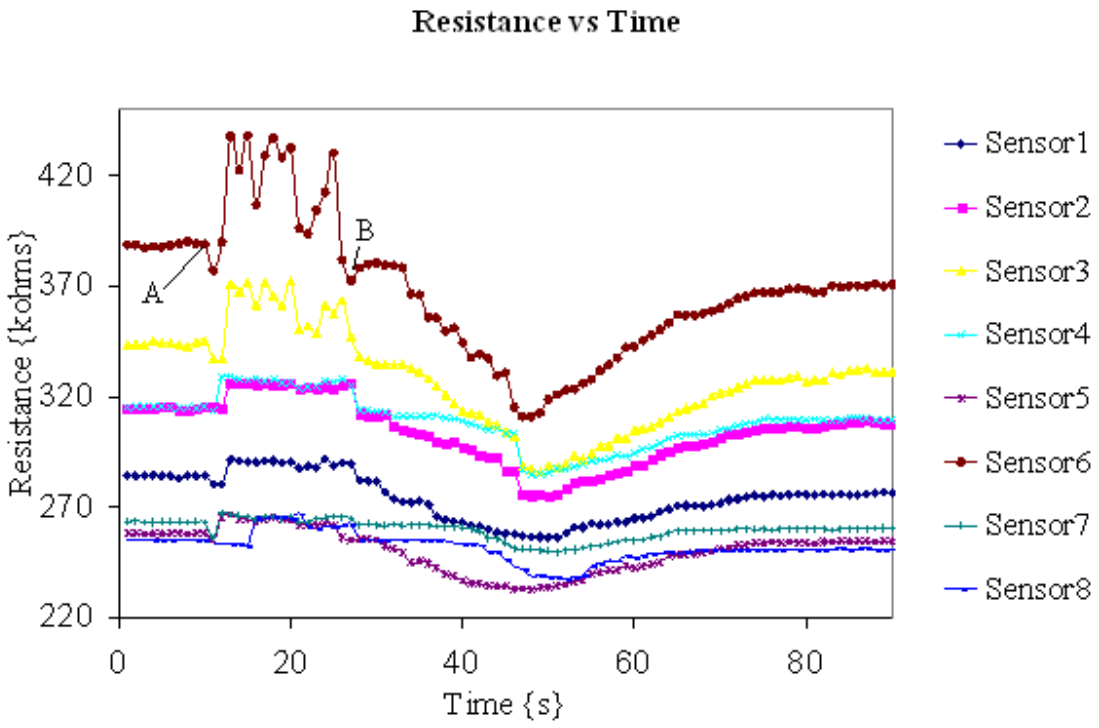

Appendix K

Steady state experiment and CFD results for mine geometries 1 and 2 are compared in this appendix as follows:

Mine Geometry One (MG-1)

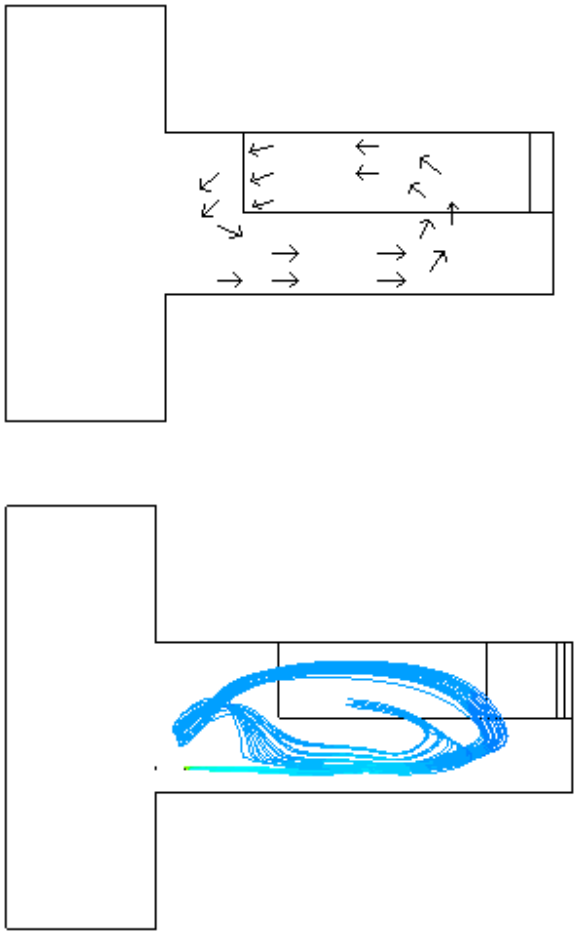

Plan view experiment and CFD results.

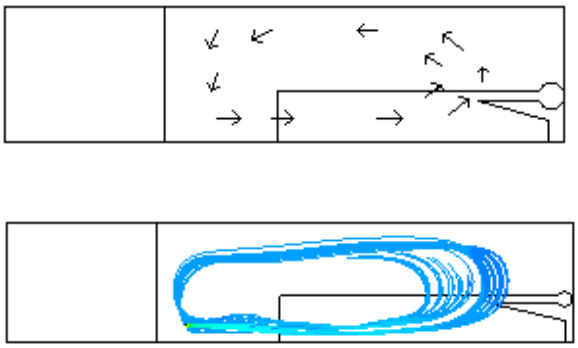

Front view experiment and CFD results.

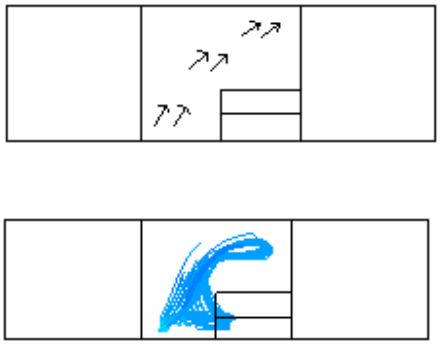

End view experiment and CFD results.

Air flow pattern appears to be similar in all the three views of MG-1.

Mine Geometry Two (MG-2)

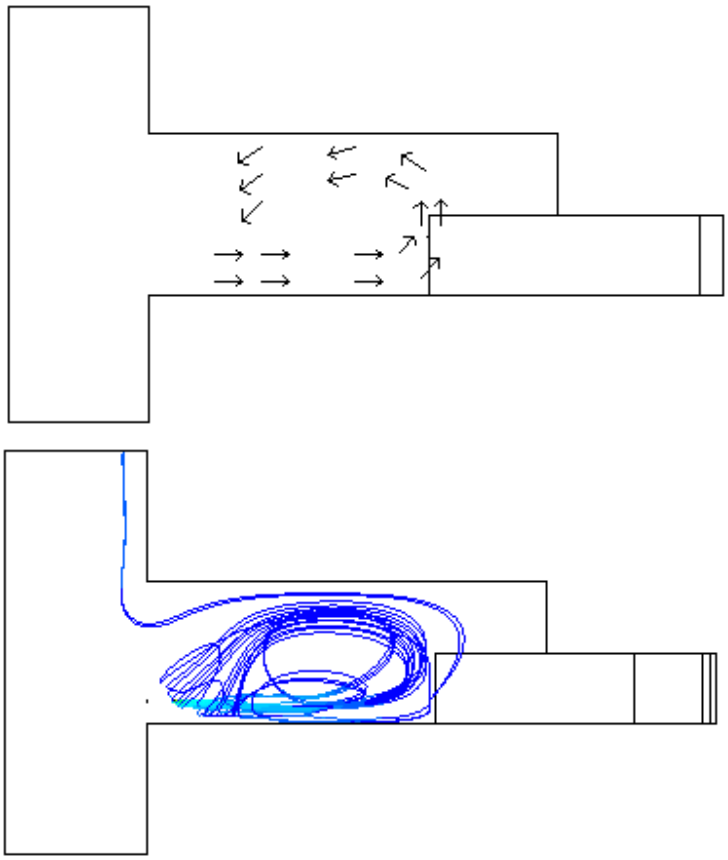

Plan view experiment and CFD results.

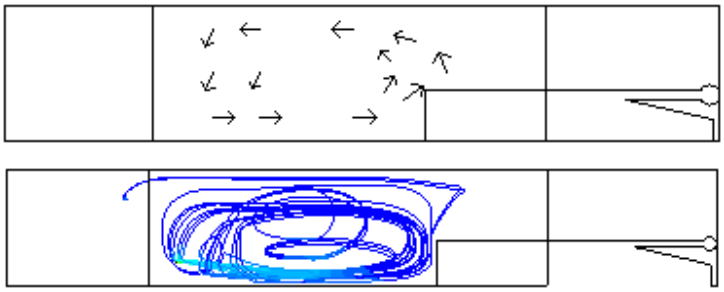

Front view experiment and CFD results.

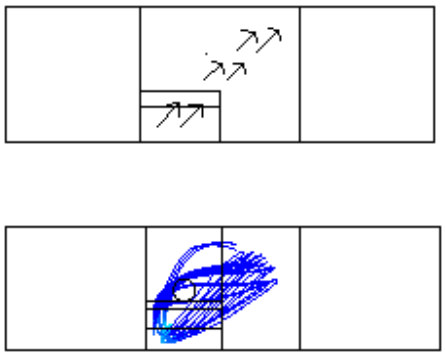

End view experiment and CFD results.

Air flow pattern appears to be similar in all the three views of MG-2.

Appendix L

The solutions for the searching exercise for optimum position of jet fan in heading lengths 467, 933, 1400 and 1867 mm with full heading width are presented in section L.1 of this appendix. And the solutions all the five heading lengths with half heading width are presented in section L.2. The searching exercise for 2333 mm long heading with full heading width has already been presented in details in chapter 6. Although more than three positions were done for each of heading length only the optimum and the nearest positions behind and beyond the optimum are shown.

L.1 Search Results for Full Width Headings

L.1.1 Heading Length – 467 mm

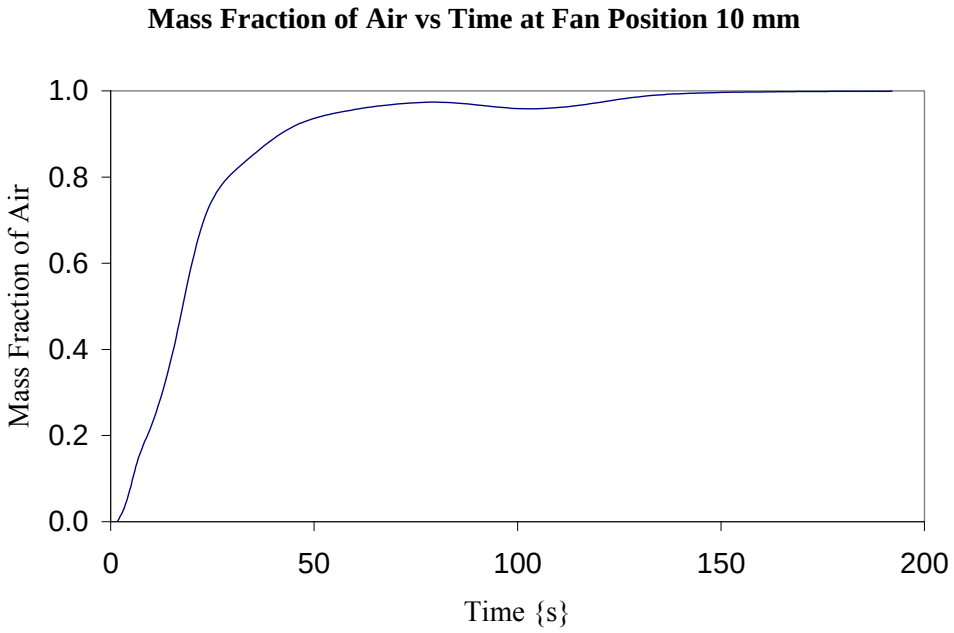

Figure L.1.1: Graph of mass fraction of air against time showing that the pollutants were extracted in 145 seconds at fan position 10 mm.

Mass Fraction of Air vs Time at Fan Position 15 mm

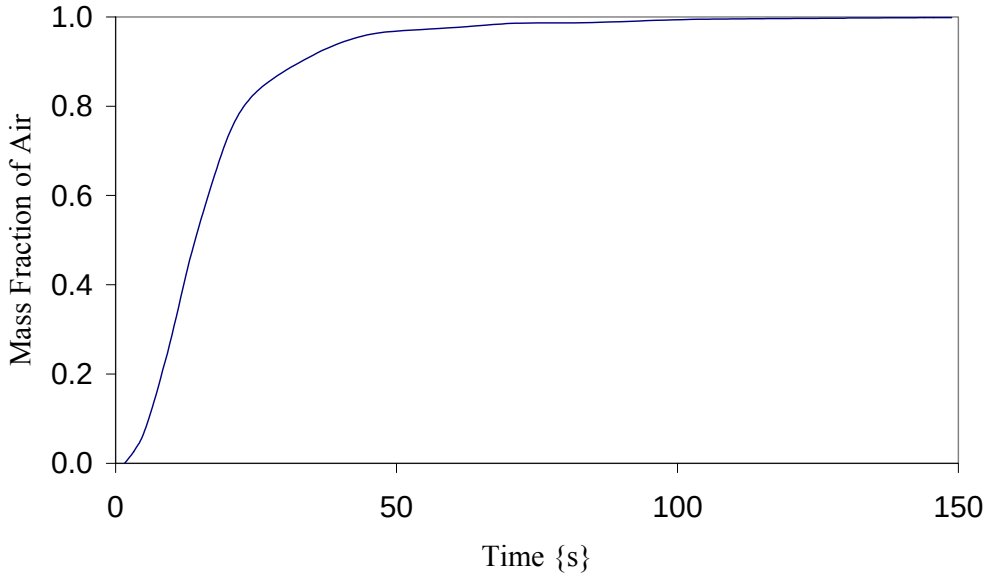

Figure L.1.2: Graph of mass fraction of air against time showing that the pollutants were extracted in 108 seconds at fan position 15 mm.

Mass Fraction of Air vs Time at Fan Position 20 mm

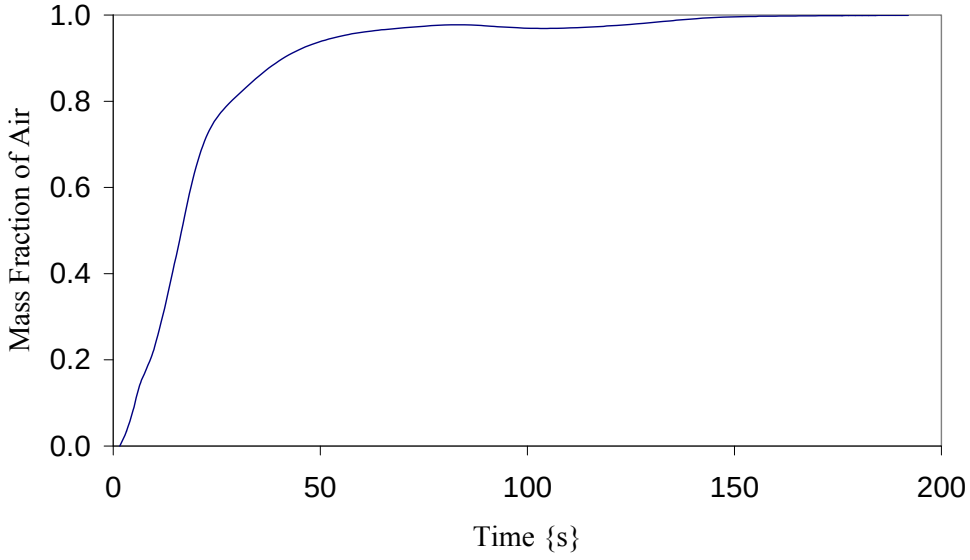

Figure L.1.3: Graph of mass fraction of air against time showing that the pollutants were extracted in 148 seconds at fan position 20 mm.

Looking at the results for a 467 mm long heading shown in figures L.1.1 to L.1.3, fan position 15 mm has the shortest extraction time of 108 seconds as compared to 145 and 148 seconds for fan positions 10 and 20 meters respectively. Therefore fan position 15 mm is optimum for this particular length of heading.

L.1.2 Heading Length – 933 mm

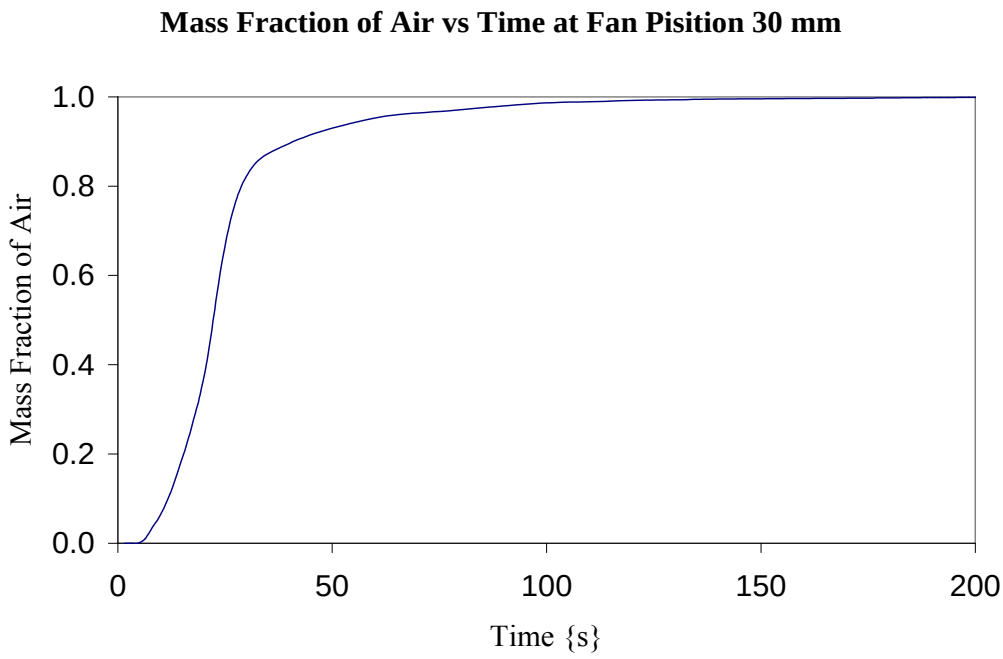

Figure L.1.4: Graph of mass fraction of air against time showing that the pollutants were extracted in 141 seconds at fan position 30 mm.

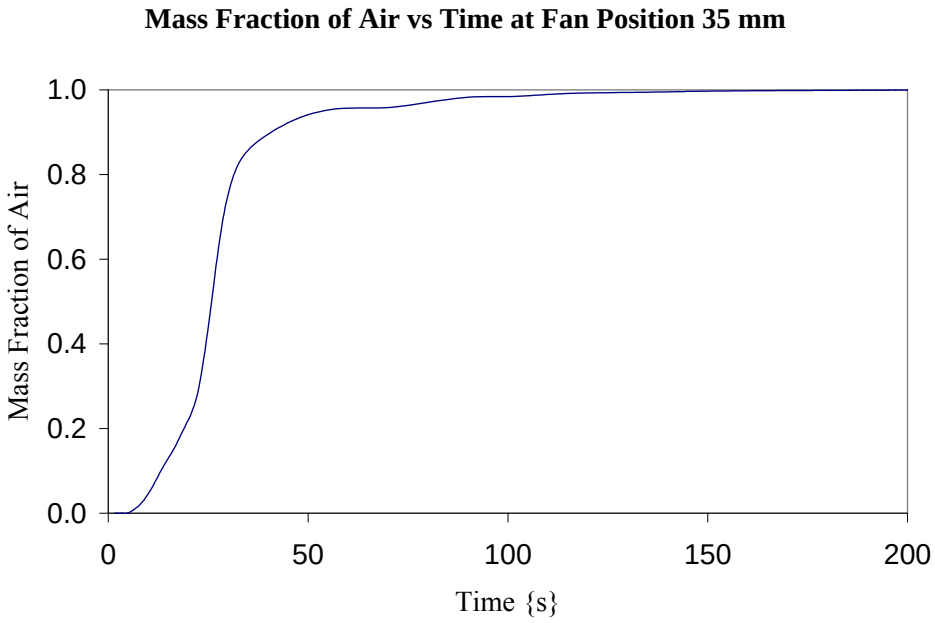

Figure L.1. 5: Graph of mass fraction of air against time showing that the pollutants were extracted in 137 seconds at fan position 35 mm.

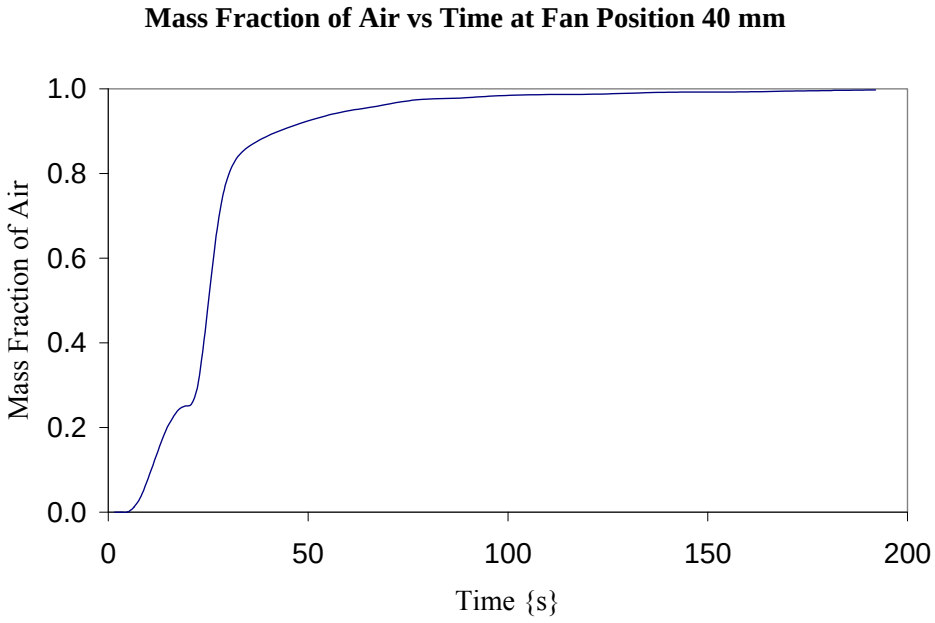

Figure L.1.6: Graph of mass fraction of air against time showing that the pollutants were extracted in 171 seconds at fan position 40 mm.

For the heading length of 933 mm fan position 35 mm with extraction time of 137 seconds is optimum as compared to positions 30 and 40 mm with extraction time of 141 and 171 seconds respectively.

L.1.3 Heading Length – 1400 mm

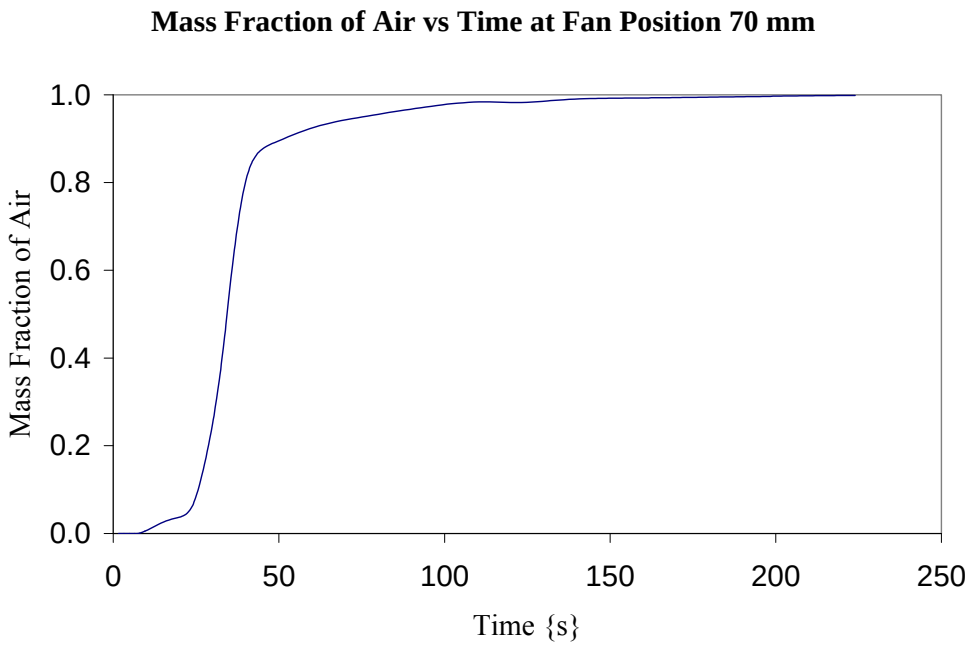

Figure L.1.7: Graph of mass fraction of air against time showing that the pollutants were extracted in 137 seconds at fan position 35 mm.

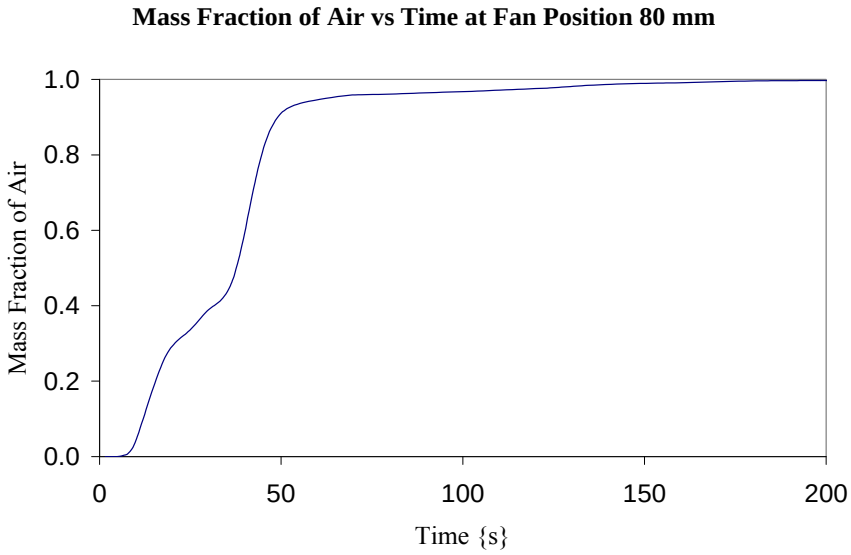

Figure L.1.8: Graph of mass fraction of air against time showing that the pollutants were extracted in 137 seconds at fan position 80 mm.

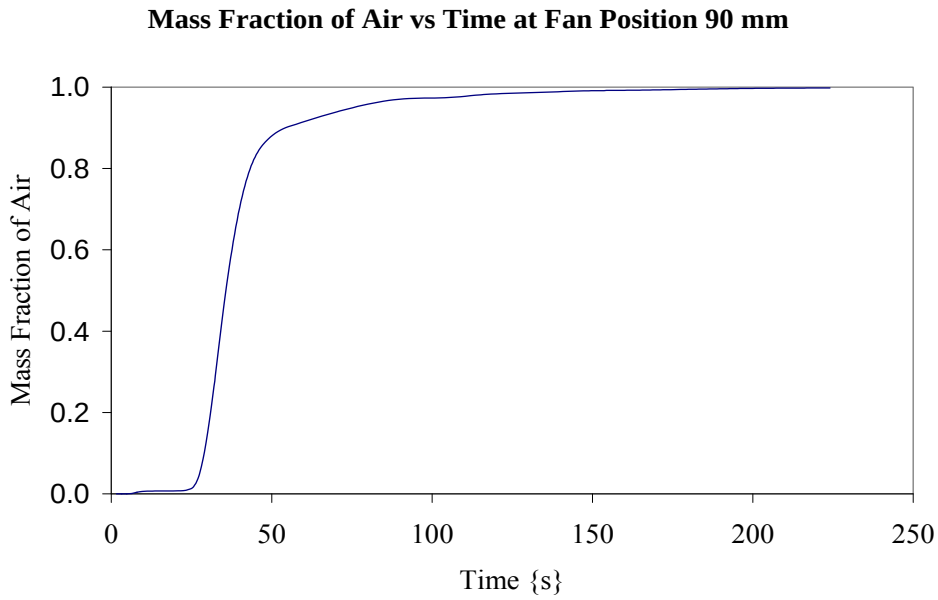

Figure L.1.9: Graph of mass fraction of air against time showing that the pollutants were extracted in 137 seconds at fan position 35 mm.

For the heading length of 1400 mm fan position 80 mm with extraction time of 174 seconds is optimum as compared to positions 70 and 90 mm with the same extraction time of 184 seconds.

L.1.5 Heading Length – 1867 mm

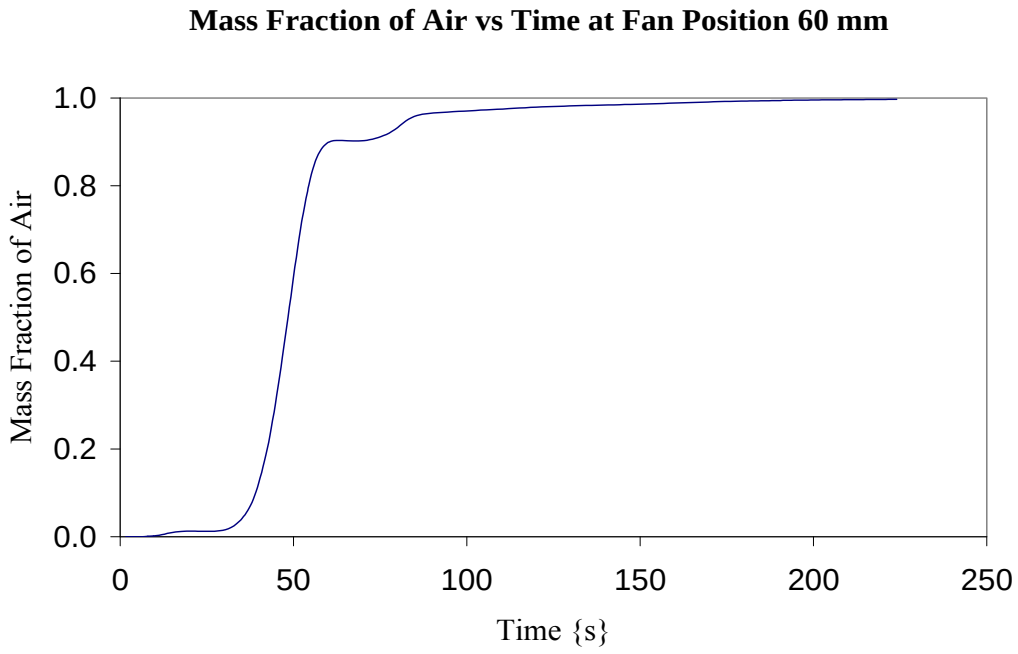

Figure L.1.10: Graph of mass fraction of air against time showing that the pollutants were extracted in 197 seconds at fan position 60 mm.

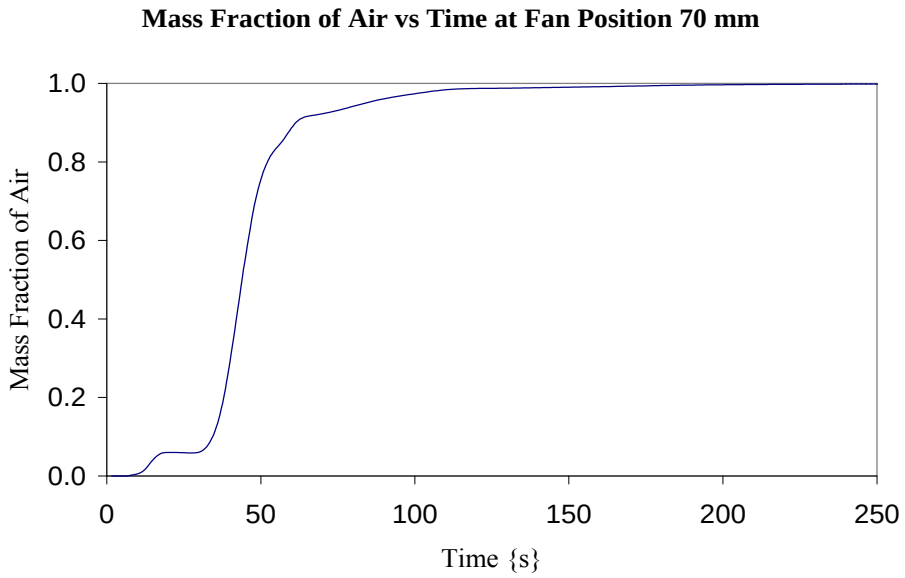

Figure L.1.11: Graph of mass fraction of air against time showing that the pollutants were extracted in 184 seconds at fan position 70 mm.

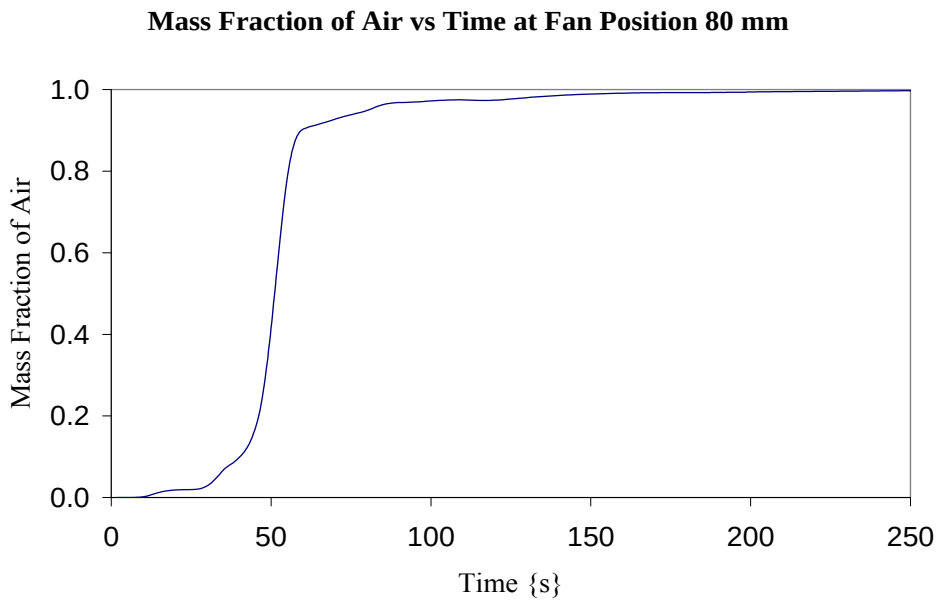

Figure L.1.12: Graph of mass fraction of air against time showing that the pollutants were extracted in 214 seconds at fan position 80 mm.

For the heading length of 1867 mm fan position 70 mm with extraction time of 184 seconds is optimum as compared to positions 60 and 80 mm with extraction time of 197 and 214 seconds respectively.

L.2 Search Results for Half Width Headings

L.2.1 Heading Length – 467 mm

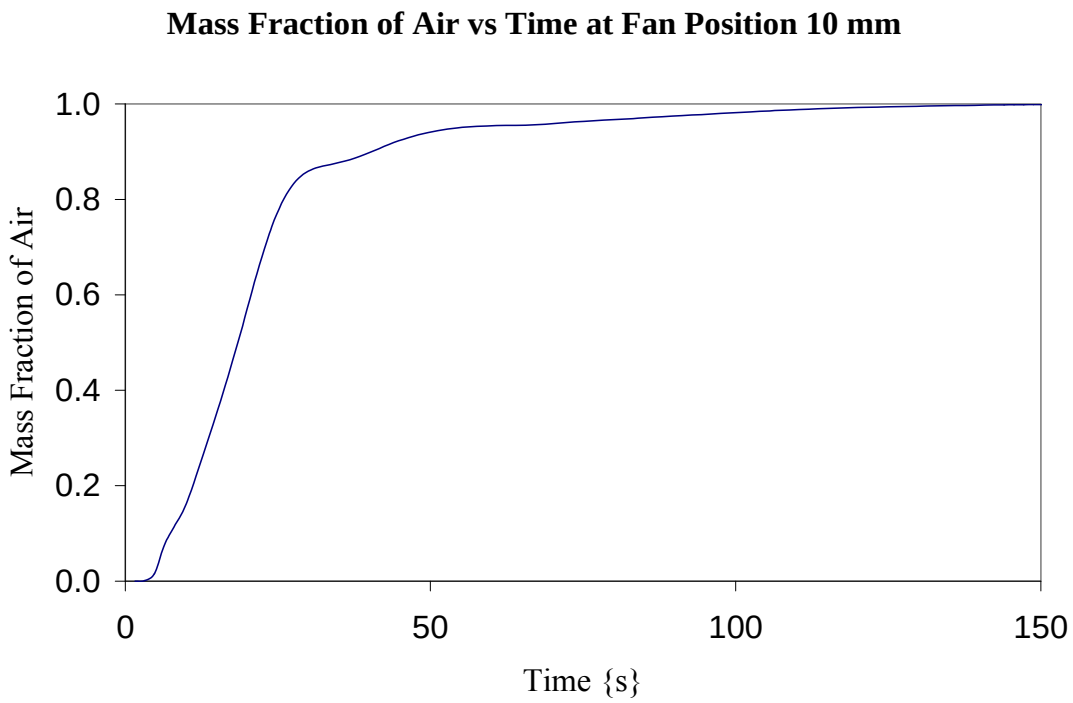

Figure L.2.1: Graph of mass fraction of air against time showing that the pollutants were extracted in 113 seconds at fan position 10 mm.

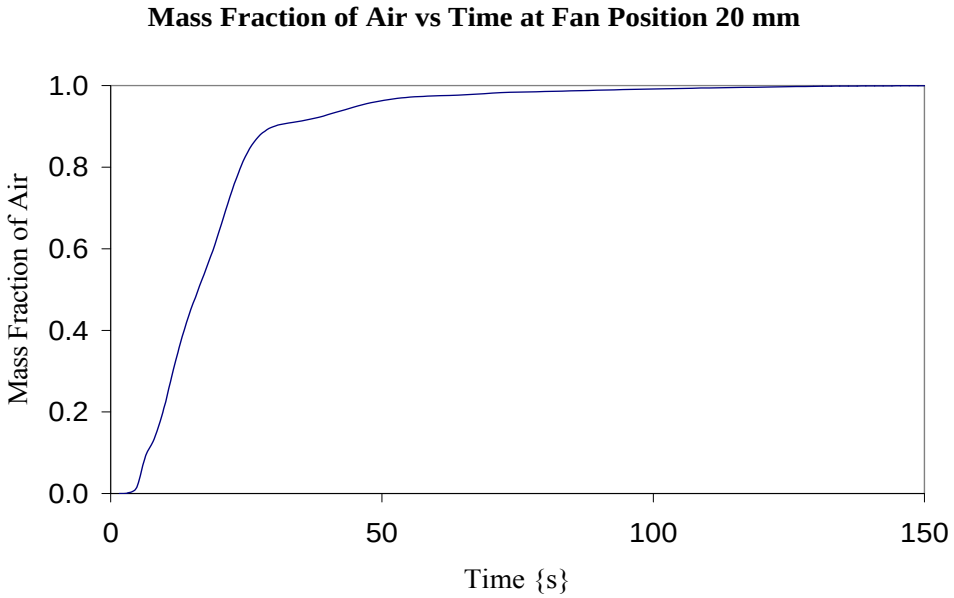

Figure L.2.2: Graph of mass fraction of air against time showing that the pollutants were extracted in 94 seconds at fan position 20 mm.

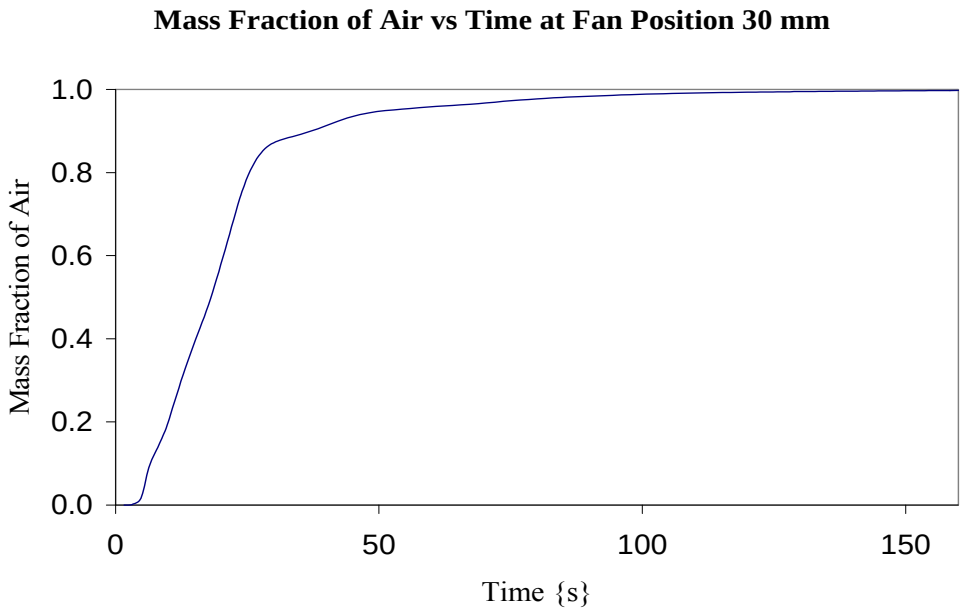

Figure J.1.3: Graph of mass fraction of air against time showing that the pollutants were extracted in 105 seconds at fan position 30 mm.

For the heading length of 467 mm fan position 20 mm with extraction time of 94 seconds is optimum as compared to positions 10 and 30 mm with extraction time of 113 and 105 seconds respectively.

L.2.2 Heading Length – 933 mm

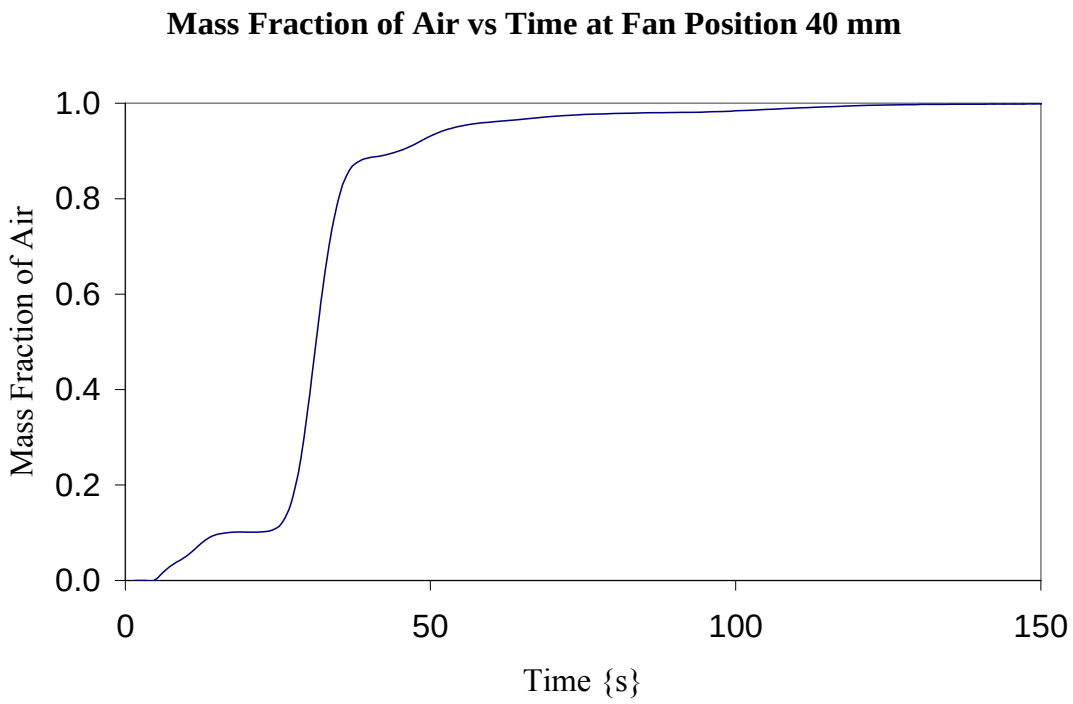

Figure L.2.4: Graph of mass fraction of air against time showing that the pollutants were extracted in 110 seconds at fan position 40 mm.

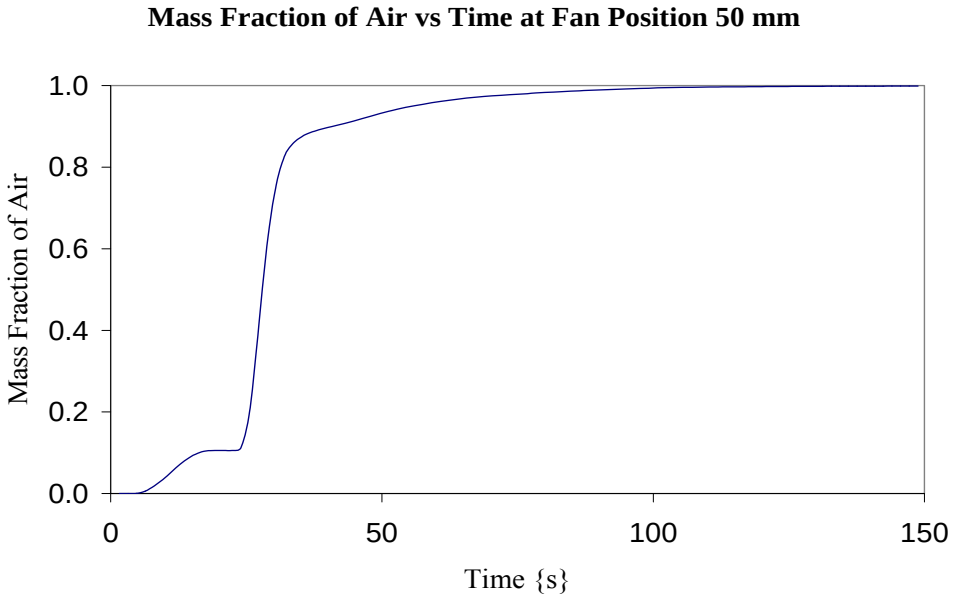

Figure L.2.5: Graph of mass fraction of air against time showing that the pollutants were extracted in 91 seconds at fan position 50 mm.

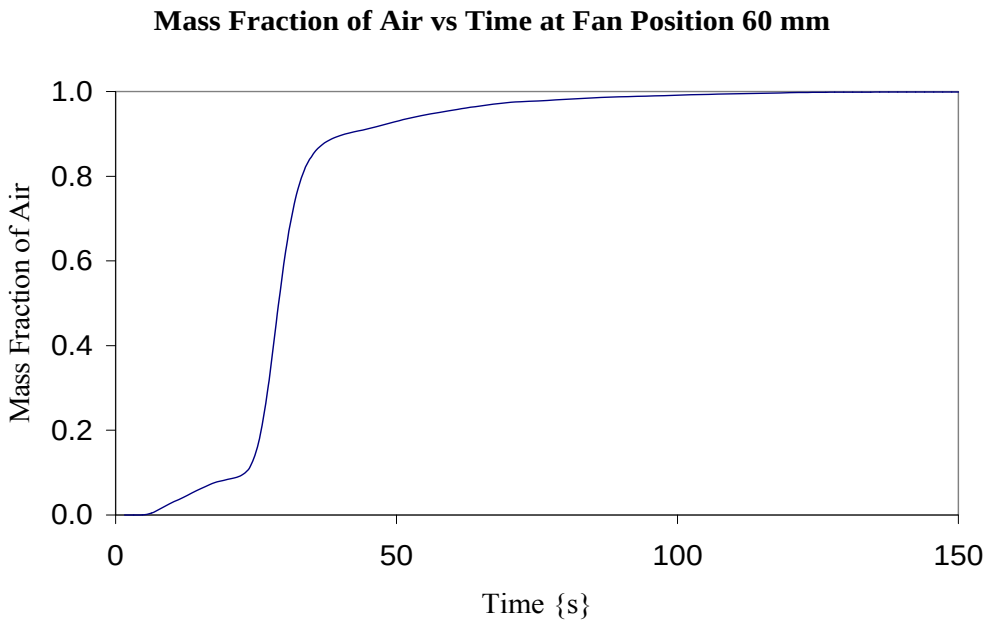

Figure L.2.6: Graph of mass fraction of air against time showing that the pollutants were extracted in 96 seconds at fan position 60 mm.

For the heading length of 933 mm fan position 50 mm with extraction time of 91 seconds is optimum as compared to positions 40 and 60 mm with extraction time of 110 and 96 seconds respectively.

L.2.3 Heading Length – 1400 mm

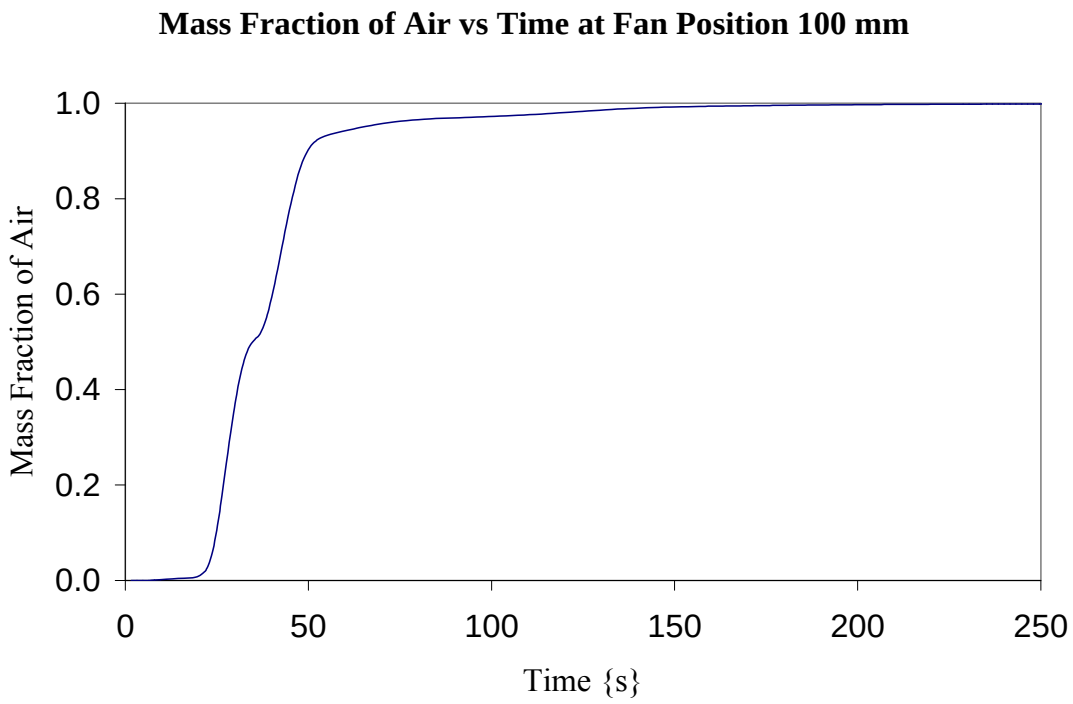

Figure L.2.7: Graph of mass fraction of air against time showing that the pollutants were extracted in 141 seconds at fan position 100 mm.

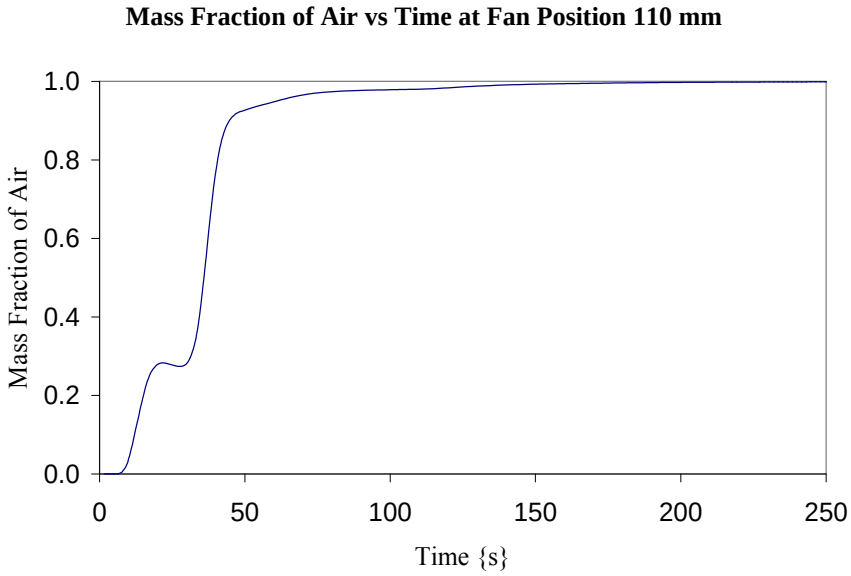

Figure L.2.8: Graph of mass fraction of air against time showing that the pollutants were extracted in 136 seconds at fan position 110 mm.

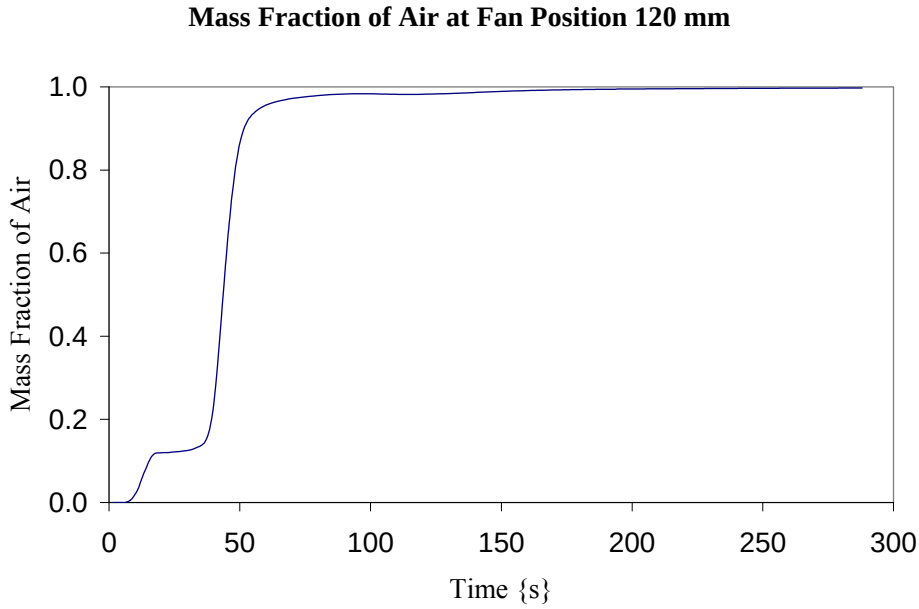

Figure L.2.9: Graph of mass fraction of air against time showing that the pollutants were extracted in 154 seconds at fan position 120 mm.

For the heading length of 1400 mm fan position 110 mm with extraction time of 136 seconds is optimum as compared to positions 100 and 120 mm with extraction time of 141 and 154 seconds respectively.

L.2.4 Heading Length – 1867 mm

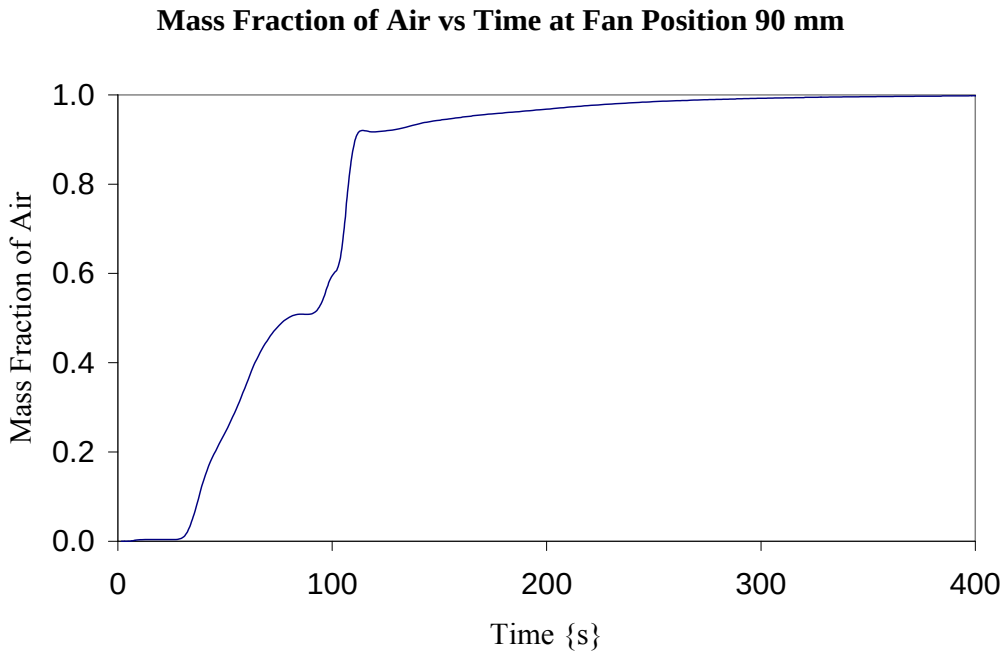

Figure L.2.10: Graph of mass fraction of air against time showing that the pollutants were extracted in 282 seconds at fan position 90 mm.

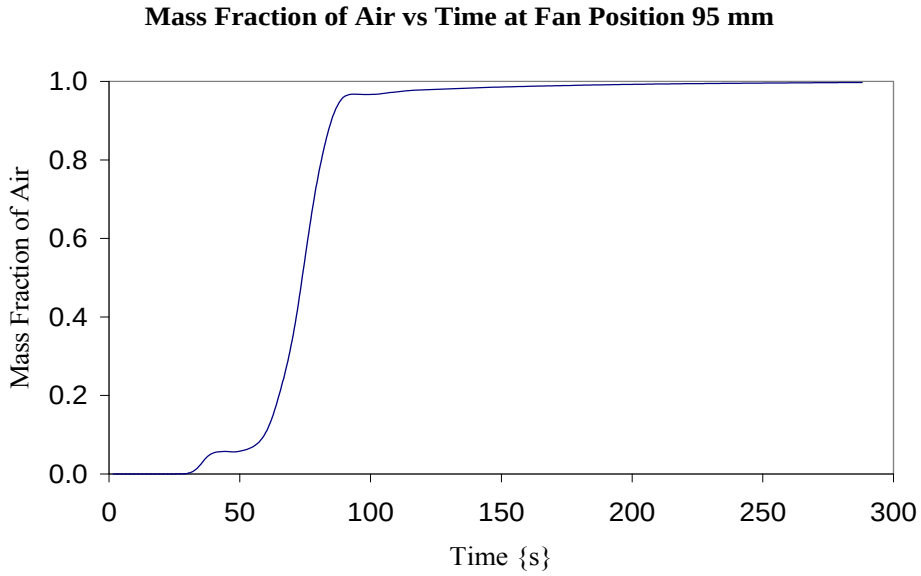

Figure L.2.11: Graph of mass fraction of air against time showing that the pollutants were extracted in 178 seconds at fan position 95 mm.

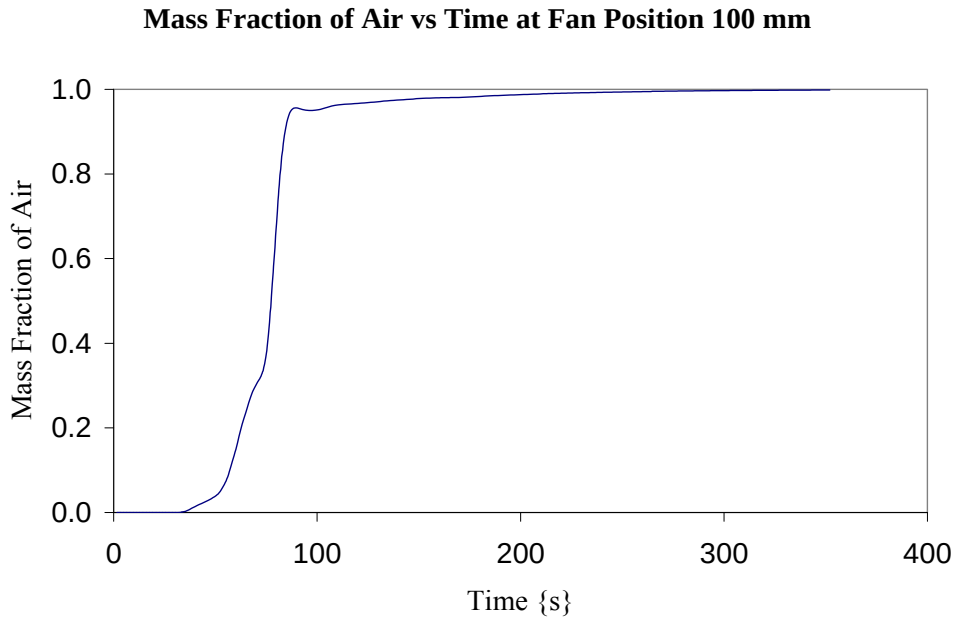

Figure L.2.12: Graph of mass fraction of air against time showing that the pollutants were extracted in 216 seconds at fan position 100 mm.

For the heading length of 1867 mm fan position 95 mm with extraction time of 178 seconds is optimum as compared to positions 90 and 100 mm with extraction time of 282 and 216 seconds respectively.

L.2.5 Heading Length – 2333 mm

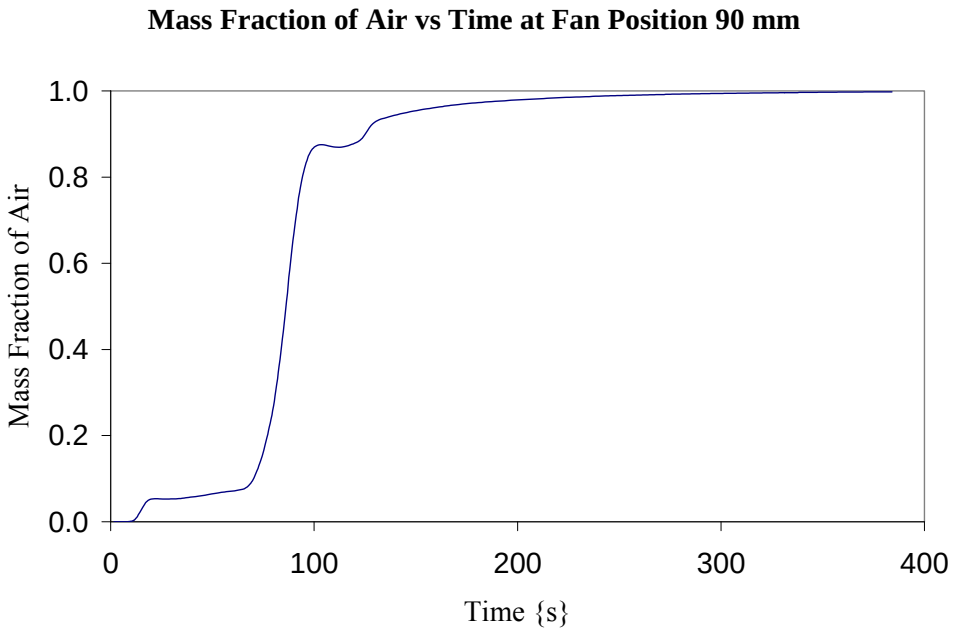

Figure L.2.13: Graph of mass fraction of air against time showing that the pollutants were extracted in 256 seconds at fan position 90 mm.

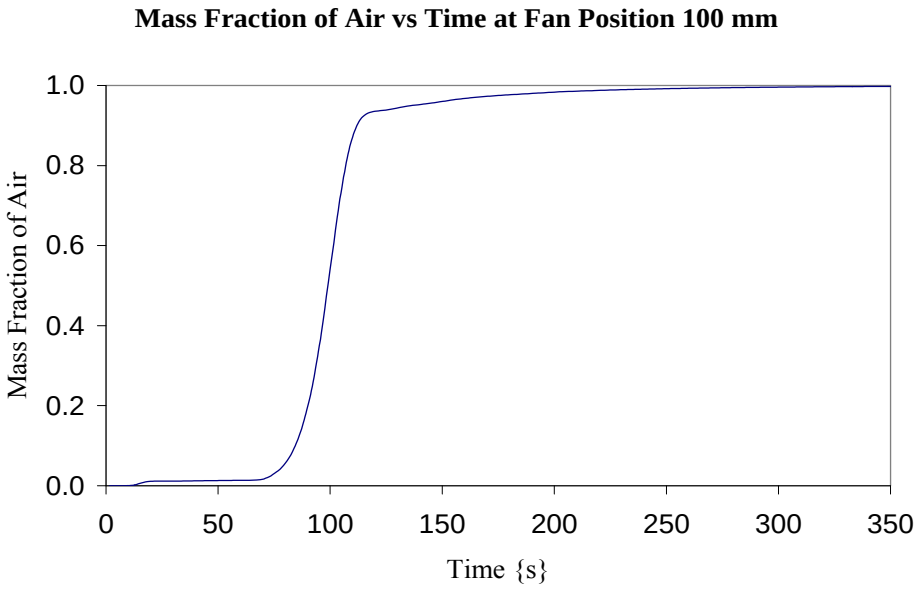

Figure L.2.14: Graph of mass fraction of air against time showing that the pollutants were extracted in 235 seconds at fan position 100 mm.

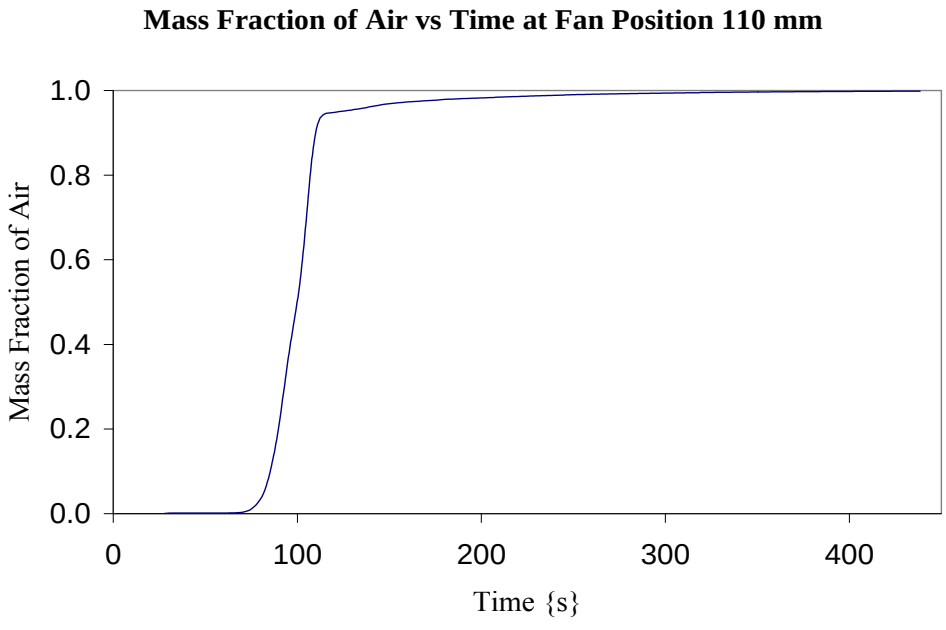

Figure L.2.15: Graph of mass fraction of air against time showing that the pollutants were extracted in 251 seconds at fan position 110 mm.

For the heading length of 2333 mm fan position 100 mm with extraction time of 235 seconds is optimum as compared to positions 90 and 110 mm with extraction time of 256 and 251 seconds respectively.